Dissertation

Determination of occupational exposure to the eye lens in the Cath lab during pelvic endovascular interventions

submitted by

Alexander Rene Gangl, MSc.

for the Academic Degree of

Doctor of Medical Science

(Dr. scient. med.)

at the

Medical University of Graz

Department of Neuroradiology, vascular and interventional Radiology

under Supervision of

Univ. Prof. Dr. Hannes Deutschmann

2021

"Declaration

I hereby declare that this thesis is my own original work and that I have fully acknowledged by name all of those individuals and organizations that have contributed to the research for this thesis. Due acknowledgement has been made in the text to all other material used. Throughout this thesis and in all related publications I followed the "Standards of Good Scientific Practice and Ombuds Committee at the Medical University of Graz ".

Graz, 16.08.2021

Disclosures

Following co-authors also were acting as supervisors of this thesis.

- Univ. Prof. Dr. Hannes Deutschmann[1]
- Univ.Prof. Dr. Rupert H. Portugaller[1]
- Univ. Doz. Mag. Dr. Georg Stücklschweiger[2]

It has to be confirmed that (a) all co-authors have agreed to the inclusion of their published data in the dissertation and that (b) permission to reproduce illustrations and figures (Figure 6) from own and third-party publications (Scannavino, F. A. and Cruvinel, P. E. (2012) 'A graphical tool for an analytical approach of scattering photons by the Compton effect', *Nuclear Instruments and Methods in Physics Research, Section A: Accelerators, Spectrometers, Detectors and Associated Equipment*. Elsevier, 674, pp. 28–38. doi: 10.1016/j.nima.2011.12.120) has been granted.

[1]*Department of Radiology, Division of Neuroradiology, Vascular and Interventional Radiology, University Hospital Graz, AT*

[2]*Department of Medical Physics and Radiation Protection, University Hospital Graz, AT*

Acknowledgements

In the last five years, I have received lots of encouragement, support and patience from my private and professional surroundings. Especially, would like to express my personal thanks to Univ. Prof. Dr. Rupert Portugaller and Univ. Doz. Mag. Dr. Georg Stücklschweiger acting as co-supervisors. Their valuable technical support was instrumental in the creation of this dissertation.

I would like to thank the entire team of the "Competence Centre of Physical Medicine and Radiation Protection" for their prompt respond to my special requests and their professional support.

To all my colleagues of the "Clinical Department of Neuroradiology, Vascular and Interventional Radiology", I just want to say, that I'm so grateful being part of this amazing team.

I would also like to thank the Doctoral School for Sustainable Health Research under the direction of Prof. Andrea Berghold.

Finally, I want to say thank you to my family and all my friends giving me strength and support throughout this challenging period. Thanks for forbearing with me in serval difficult emotional moments.

In the end, I would like to express my regrets regarding the unexpected death of Univ. Prof. Dipl. Ing. Dr. Peter Kindl. He was my external supervisor and a longtime friend of my family. On this way, I would like to express my most sincere condolences to his widow.

Table of Contents

Abstract

Sehr früh nach Entdeckung der Röntgenstrahlung wurde die negative Wirkung von ionisierender Strahlung auf menschliches Gewebe nachgewiesen. Um adäquaten Schutz beim Umgang mit Röntgenstrahlung gewährleisten zu können, sind eine exakte Strahlendosimetrie, sowie auch eine effiziente Abschirmung notwendig. Diese wissenschaftliche Arbeit beschäftigt sich mit dem Vergleich eines neuen kompakten Echtzeitdosimetriesystems (RaySafe i3) mit etablierten Messgeräten, sowie seine Möglichkeiten zur Bestimmung der Strahlenbelastung der Augenlinse während vaskulärer Interventionen der Beckenarterien. Des Weiteren wird der Wirkungsgrad von Strahlenschutzbrillen unter verschiedenen Aspekten (Brillendesign, Augenhöhe, Blickrichtung und Art des Streukörpers) beleuchtet und mit bestehender Literatur verglichen. Diese Arbeit bestätigt die Zuverlässigkeit von RaySafe i3 im Zuge von durchleuchtungsgezielten Interventionen. Unter Einschränkungen ist eine Einschätzung der Augenlinsenbelastung durch auftretende Streustrahlung mittels erstellter Umrechnungsfaktoren möglich. Bezüglich der Performanz von Strahlenschutzbrillen werden große Unsicherheiten durch unterschiedliche Parameter (Körpergröße, Blickrichtung) hervorgerufen. Die Bandbreite von Dosisreduktionsfaktoren lag zwischen 1.1 und 7.9.

Abstract

Since the discovery of X-rays, it did not take long time to recognize the adverse effects of ionizing radiation on human tissue. have been recognized. To guarantee adequate radiation protection during fluoroscopic guided interventions, sufficient protection devices and also reliable monitoring applications are mandatory. The main purpose of this thesis is to evaluate the use of the latest real-time personnel dosimetry device (RaySafe i3) forestimation of the eye lens dose of medical staff working in the Cath lab.

Furthermore, we sought to evaluate the efficacy of radiation protection glasses with regard to several parameters (design of protection glasses, eye level, viewing direction and the type of scattering bodies) and to compare the results with current scientific evidence. The results of this work confirm the reliability of the RaySafe i3-system for monitoring radiation areas. Concerning the estimation of radiation exposure to the lens of eye, the usage of conversion factors is limited. The protective ability of radiation protection glasses in varying experimental setups and different types of glasses is heterogeneous. A wide range of dose reduction factors from 1.1 to 7.9 was determined.

1 Introduction

Interventional radiology (IR) is representing the combination of high-end fluoroscopic imaging devices allowing visualisation of smallest vessels and a huge spectrum of catheters and wires enabling the interventionist to navigate to also distally located lesions in a minimally invasive way. In the last two decades, in the field IR, the number and also the types of interventions have shifted from mainly diagnostic to therapeutic procedures. This development is based on the rapid technical progress of modern angiography units. Another important aspect regarding the growth of the spectrum of interventions in IR is a massive increase in the range of new catheters, wires and other medical devices (stents, balloons, embolic agents). All these developments allow more therapeutic options, especially regarding patients in a critical conditions, because of the lower invasiveness of intervention with a shorter time of recovery, less morbidity and also lower mortality (Bahruddin *et al.*, 2016)(Stecker *et al.*, 2009). Simultaneously non-invasive imaging techniques like computer tomography (CT), magnetic resonance imaging (MRI) and ultrasound (US) have undergone a big step forward, especially in the field of vascular imaging. The considerable achievements are reduced scanning time, the higher spatial resolution as well as the new post processing techniques (Kishore and Gupta, 2013). This progress inevitably results in a decreased demand of primary diagnostic catheter angiographies(Hart *et al.*, 2010).

An increase of more time consuming therapeutic interventions in the Cath-lab ends in a higher radiation exposure for the medical staff and the treated patients (Stecker *et al.*, 2009). Especially in the situation of pelvic vascular interventions two adverse situations regarding radiation protection arise: One the one hand, pelvic vascular interventions always go hand in hand with an increased irradiated volume in comparison to peripheral vascular interventions. This causes a higher radiation exposure to the staff because of a higher dose of scattered radiation (W.J. Meredith, 1968).On the other hand, due to the femoral puncture, the distance from the centre of the imaged region (pelvic region) and the medical staff is because is shorter compared to interventions in other regions (e.g. head, feet). This setup ends in high scatter radiation dose levels at typical positions for interventionists, assisting staff and also for the anaesthesiologic team.

Additionally, studies have demonstrated that the dose distribution along the angiographic table does not always stick to the inverse square law. Perpendicular to lateral edges higher dose values have been detected compared to dose distribution along the head-foot axis.

The incremental complexity of pelvic vascular interventions also has a negative effect on the radiation time. Consequently, the rapid progress of minimal invasive therapeutic treatments ends up to an increasing radiation exposure risk medical staff (Haqqani *et al.*, 2013). Referring to patients, the risk of radiation damages is low compared to the benefit endovascular interventions imply (Stecker *et al.*, 2009).

Interventional radiological procedures are representing only a small part (2 percent) of the total amount performed examinations at radiological clinics. Nevertheless this small part of overall frequency stands for about 20 percent of collective effective dose (Reaktorsicherheit, 2014).

New insights regarding tissue weighting factors (Brenner, 2011), caused a reduction of the dose limit for occupational exposure in planned exposure situations for the lens of eye from 150 mSv to 20 mSv a year. The uncertainty concerning the scientific evidence of threshold doses (Chodick *et al.*, 2008a) seem to raise more questions regarding radiation protection than they answer. Worldwide efforts of international organisations for enhancement of radiological protection (ALARA ("as low as reasonably achievable") principles, "Bonn call for Action"…) but also a growing number of discussions on relevant congresses and conferences (e.g. "radiation protection pavilion") raise interest of medical staff working in the angiography suite in the issue of radiation protection.

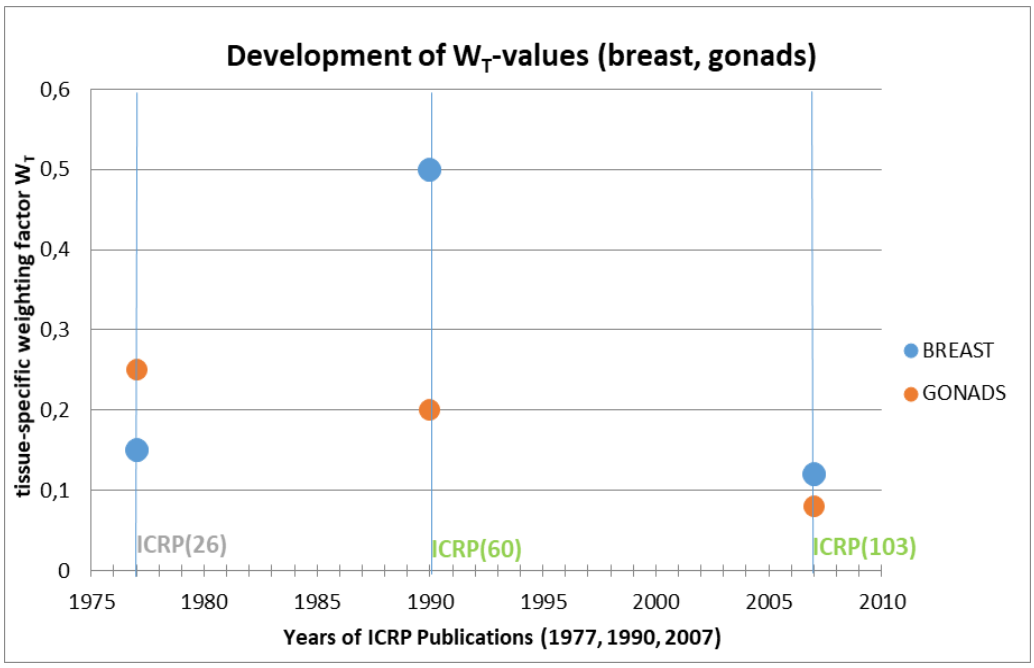

Figure 1: Change of tissue-specific factors WT (ICRP 26, ICRP 60 and ICRP 103) (European Commission, 2014)

As a consequence, vendors have developed new strategies in reducing the dose exposure to the treated patients but also to the involved medical staff. A great number of radiation protection devices (lead aprons, radiation safety glasses and headwear) are available on the market. Manufacturers of angiography systems are developing hardware and software tools to achieve lower radiation exposures for patients and medical staff in the course of X-ray guided interventions combined with respectable image quality. For educational purposes in dealing with X-rays, easily applicable real-time radiation dose monitoring systems have been developed resulting in a proven benefit (Sandblom *et al.*, 2013). These personal dosimeters (PDM) are intended to be worn as an above-apron dosimeter to measure and display the accumulated dose and the current dose rate of the personnel.

Dosimeters worn under the lead apron may result in dose data, underestimating the dose exposure to the medical personnel in daily clinical practice (Seals *et al.*, 2016). Consequently, all organisations dealing with radiation protection in medicine, recommend wearing at least two dosimeters, one above the apron and another one below the apron to achieve a realistic estimation of effective dose in the angiography suite (Icrp, 2012).

2 Aims and Objectives

2.1 Aims

We identified three relevant scientific questions:

- Is the real-time dosimetry system RaySafe i3 a useful tool for estimation of eye lens dose?
- Does this system provide reliable dose data that can be used for further quantification of the dose exposure of the lens of eye during interventional procedures?
- Are lead glasses effective protection devices and is the degree of safety varying with the change of the orientation of the interventionist's head?

2.2 Objectives

- To quantify dose values by using RaySafe i3 and compare it to other established dosimetry systems?
- To assess the measurement accuracy considering the angular dependence of RaySafe i3.
- To determine the dose exposure to the lens of eye and to other points of measurement for receiving correction factors obtained from different measurement techniques (RaySafe i3, TLD, dose area product).
- To quantify dose exposure to the lens of eye depending on different types of lead glasses and altering alignment of the interventionist's head.
- To determine the impact of magnification level on the radiation exposure of the lens of eye.

To carry out dosimetry of the lens of eye, thermoluminescent dosimeters (TLD) have to be calibrated to several experimental setups.

3 Radiobiological effects regarding the human eye lens

For better understanding of the processes affecting the radiation cataract some basic terms dealing with this topic are to be explained as follows:

3.1 Tissue radiation effects

Radiation exposure interacting with human tissue does have a health effect that "varies greatly in the shape of dose-response curve, latency, persistency, recurrence, curability, fatality and impact on quality of life (QOL)"(Hamada and Fujimichi, 2014). The International Commission on Radiological Protection (ICRP) grouped all these effects in tissue reactions that are coupled with a preceding threshold dose and stochastic effects whose probability of occurrence raises with the increase of dose without any threshold.

3.1.1 Tissue reactions

Tissue reactions, formerly known as non-stochastic effects (ICRP Publication 26) or deterministic effects (ICRP Publication 60) are defined by the characteristic of incidence and by the severity of the extent of damage. Tissue reactions are called early or acute effects. The extent of severity is varying with the amount of dose exposure and the probability occurrence is always associated with a defined threshold dose. These deterministic effects are resulting from damaged cellular tissue ending up with failures of its biological functions. To avoid tissue reactions, equivalent dose limits are established (Hamada and Fujimichi, 2014). Since human tissue varies in its radio-sensitivity, individual threshold doses are known (Protection, 1987). Tissues showing early indications of damage are generally those with a high proliferative behaviour (e.g. bone marrow). Tissue reactions, such as cataracts, non-malignant skin damage or impaired fertility are individual predictable since the thresholds are well defined and exactly applicable.

Regarding low-dose radiation and its effect on cancer risk for occupational exposured workers, several studies are representing opposing views. On the one hand the radiation hormesis concept considers that doses below 100 mSv of ionizing radiation may be harmless

or even beneficial (Doss, 2013). On the other hand, the linear no-threshold (LNT) dose-respond model refers to non-harmless dose of radiation without any lower limit.

3.1.2 Stochastic effect

Stochastic effects are primarily dealing with cancer or hereditary effects. The tendency of appearance is a function of dose. Since the stochastic effects are occurring by chance, an individual prediction is not feasible. Therefore, the calculation of stochastic effects is always targeted on a larger sample size. To reduce the risks of stochastic effects, effective dose limits are defined (Hamada and Fujimichi, 2014). In contrast to tissue reactions, the occurrence of stochastic effects is independent on any thresholds. That is why stochastic effects are closely linked to the Linear No-Threshold (LNT) hypothesis.

3.2 Linear No-Threshold Dose-Respond Model

The substantial key massage of LNT model is that there is no "safe" dose of radiation. The weak point of the LNT hypothesis is that the dose response data for high dose radiation, such as atomic bomb survivors has linearly been extrapolated down to the spectrum of low radiation doses. Although a number of reports and studies are not in consent with the LNT model, authoritative scientific institutions like the National Council on Radiation Protection and Measurements (NCRP) or the International Commission on Radiological Protection (ICRP) have implemented the LNT model (Alderson *et al.*, 2015).

Regarding radiation-induced cataractogenesis latest scientific evidence tends to classify this radiation damage stochastic rather than deterministic (Chodick *et al.*, 2008a). As a result, ICRP revised their guidelines by decreasing the threshold dose for symptomatic cataract to 0.5 Sievert (Sv). Since present dose data may underestimate the occupational dose exposure in clinical reality (Seals *et al.*, 2016), ICRP further reduced the occupational dose limit for lens equivalent dose to 20 mSv/year averaged over defined

5-years period with no single year exceeding 50 mSv (Seals *et al.*, 2016). The former annual dose was limited to 150 mSv. Also, the IAEA has implemented these new limits in the IAEA Basic Safety standards. Current discussions are expressing doubts regarding the existence of

a threshold concerning radiation-induced cataract(IAEA (International Atomic Energy Agency), 2013).

Studies have shown that there is a real risk of exceeding the annual eye lens dose for staff working in the angiography suite (Omar *et al.*, 2017). Also the International Radiation Protection Association (IRPA) highlighted: "Workers exposed to highly non-uniform radiation fields in which the eyes may be especially exposed, such as interventional radiologists and cardiologists or other staff members who work close to the radiation source but with a part of their body protected with a lead apron or other shielding systems."(Baxter *et al.*, 2008) For getting a good estimation of effective dose and of the dose to the eye lens ICRP recommends to perform double dosimetry: A combination of two dosimeters, one worn beneath the lead apron the second one unshielded above the apron (Icrp, 2012).

For receiving a real-time response regarding the current dose exposure, the application of a PDM placed above the apron is advised. Furthermore the use of PDMs can realize an increasing awareness concerning radiation protection (Omar *et al.*, 2017) but also may provide dose data to achieve a proper estimation of the dose to the lens of eye. Since medical staff is working in inhomogeneous radiation fields, which demands double dosimetry (IAEA (International Atomic Energy Agency), 2013) the range of PDM's application could be expanded.

3.2.1 Cataract

The lens is an ellipsoid biconvex structure placed in the frontal part of the human eye. Apart from the cornea, the lens is the second functional unit of the eye, focusing incoming light. The lens is characterized by its elastic and flexible attributes. By changing its curved shape (accommodation), crossing rays of light are converged on the light sensitive retina and results in a smooth and sharp vision of objects at near and far (Figure 2).

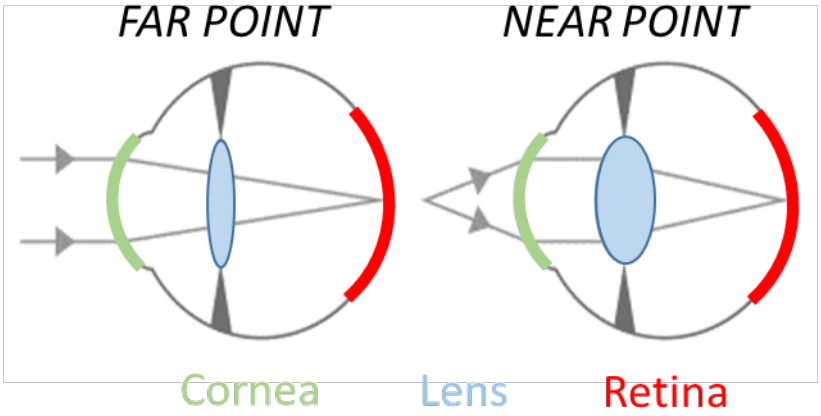

Figure 2: Adjustment of the lens to keep an object in focus on the retina (Accommodation)

3.2.2 *Functional mechanism of cataract*:

Generally, cataracts describes any loss of physiological transparency concerning any location in the lens of eye (cortical, nuclear and posterior sub-capsular).Radiation-associated lens opacities causes blurry vision, sensitivity to light, double vision or colour perception. In most cases cataract is related to ageing(Commission, Protection and Reasoning, 2009) and occur in about 50 % of the population between 65 to 75 year old with clinical manifestation and mainly occur in the anterior part of the lens. Apart from this, cataract is mostly considered to be a multifactorial disease based on congenital and developmental, traumatic, metabolic, toxic or radiation induced reasons (Gupta, Rajagopala and Ravishankar, 2014). Therefore, lifestyle habits like smoking or alcohol abuse are of same importance as gender, genetic factors ethnic predispositions or the use of corticosteroids.

In terms of ionizing radiation primary, a primary opacification of the sub-capsular region (back of the lens, inside the membranous capsule) is described. The radiation-catarctogenesis begins at the anterior surface of the lens. Highly proliferating dividing cells form a transparent protein fibre that migrates from the front to the posterior area from the lens. Under exposure of ionising radiation, the crystalline structure of these fibres become

abnormal and result in non-translucent spots in the posterior pole of the lens. At a progressed stage, these spots enlarge to opaque of several millimetres. In comparison, age-related cataract are generally caused by gradual hardening and yellowing of the central zone of the lens.

3.2.3 Risk associated with occupational exposure

Beside airline pilots or astronauts, professional groups working in the surroundings of fluoroscopic guided interventions are potentially at risk receiving high occupational eye lens doses (Omar *et al.*, 2015). A 20 years prospective cohort study implementing 35 700 radiologic technologists focused on risk of cataract caused by low dose exposure of ionizing radiation. This publication found a significant correlation between low-dose radiation exposure and an increased risk for a sub-capsular cataract formation(Chodick *et al.*, 2008b). A potential exceed of the lifetime threshold for occupational exposed staff (Jacob *et al.*, 2013), paired with scientific uncertainty regarding the existence of any threshold dose for cataract induction (Vanhavere *et al.*, 2011a), should be of sufficient concern to increase efforts regarding accurate and suitable eye dosimetry as well as also user-friendly and reliable radiation protection devices.

3.2.4 Historical review

On Friday, November 8. 1895, when Wilhelm Conrad Röntgen (1845-1923) made his most important discovery, the foundation stone was laid for a new medical specialisation: Radiology.

Within a year after finding X-rays, the first radiology department in Glasgow hospital opened.

On December 28, 1895 W.C. Röntgen presented the manuscript "On a New Kind of Rays, a Preliminary Communication". In this paper he described the penetration of the so-called X-rays through matter. Furthermore, he described that "the transparency of various substances assumed to be of equal thickness depends primarily upon their density".

Consequently Roentgen found that X-rays penetrates human tissue in another extent than bones or metals. This characteristic of X-rays he proved by creating a film of his wife's hand wearing a ring on her finger being published with the first public announcement of this historical discovery on 5. January 1896.

Regarding the development of IR, following milestones have to be mentioned:

8. November 1895: Wilhelm Conrad Röntgen discovers X-rays.

17. January 1896: Edward Haschek and O.T. Lindenthal perform the first "angiography" by injecting a mixture of petroleum and mercuric sulphide (called Teichmann's solution) in arteries of an amputated hand.

28. December 1896: The first implementation of X-rays regarding diagnostic application by Gustav Kaiser.

1901: L.E. Schmidt and D. Kolischer perform a retrograde imaging of the urinary tract

1916: C.V.S Patterson develops intensifying screen.

1923: E.A. Graham and W. Cole create the first angiography of the arteria brachialis.

1927: E. Monis performed the first cerebral angiography on a living human.

1929: The first aortography, realized by direct puncture is made by R. Dos Santos.

1929: W. Forssmann carries out a cardiac catheter examination in self-experiments.

1938: J.V. Coltmann introduces the image intensifier.

1952: A.Voorhees placed the first synthetic endoprothesis (Viynon N) into a ruptured abdominal aortic aneurysma.

1953: S.I. Seldinger implements the transfemoral arterial access bearing his name.

1964: C. Dotter is the first using a guide wire and a co-axial catheter to dilate a leg artery.

1965: Transcatheter arterial embolization opens a new perspective for IR
1976: P.H. Heintzen and his team is pioneering regarding digital subtraction angiography.
(Hefner, 1995)(Consultants, 1989)(Brant-Zawadzki *et al.*, 1983)(Hassan, 2018)

In 1896, the year after the discovery of X-rays scientists all over the world were looking for possible applications in medical sciences and other various purposes. Consequently, in the 1896 even more than 1000 papers dealing with scientific use of X-rays were published.

Since this new kind of "light" wasn't able to be seen, tasted, felt, heard or detected the general opinion was X-rays were without any adverse effects. Nevertheless an increasing number of radiation damages like erythema, dermatitis and skin ulceration were reported by Drury (1896) and Leppin (1896)(Clarke and Valentin, 2009).
Already in December 1896 Wolfram Fuchs published the first recommendations regarding radiation protection: "Make exposure as short as possible. Do not place the X-ray tube closer to the body than 12 inches. Rub the skin carefully with Vaseline and leave a layer on the part that shall be exposed."(Busch, 2013). These conclusions are the base for current recommendations regarding applied radiation protection representing major three corner stones: time, distance and shielding.
In the year 1896, Thomas Edison suffered from sore eyes after experimenting with X-rays. Worldwide in the two following years after discovery of X-rays about 100 cases of X-ray injury had been published (Strzelczyk, 1998). Resulting in all these published adverse effects the Roentgen Society established a Committee on X-ray injuries in 1896. Since there was a lack of dosimetry devices reliable qualitative recommendations regarding radiation protection were not available.
Because of increasing concerns regarding safety issues, in the year 1925 the first International Congress of Radiology aimed to establish an international committee on radiation protection. In the following year the International Commission on Radiological Protection (ICRP) was founded.
Since biological effects of X-rays were observed within months after Röntgen's discovery, first attempts concerning therapeutical application of X-rays were performed. On January 12, 1896 Emil Grubbe began treating Rose Lee suffering from a relapsed breast cancer(Vujošević and Bokorov, 2010).

4 Dosimetry

4.1 Interaction of X-rays with matter

An important issue regarding occupationally radiation protection within fluoroscopy-guided interventions is the determination of radiation quantities and also the shielding against scattering radiation. These scattered photons are resulted from interaction of X-rays with matter.

X-rays are high energetic photons generated as a result from a bombardment of accelerated electrons towards a metallic anode. These X-ray photons, with an energetic range from about 60 to 150 keV are used to generate images that are based on distributed differences in density of the irradiated volume. This obtained relief of X-ray energies is the origin of fluoroscopic imaging.

X-ray photons are imparting their energy to the surrounding either by absorption or by scattering. Depending on the irradiated cross section and occurring photon energies different mechanism of energy loss may occur.

Photons are generally considered to be massless. They are supposed to propagate in the form of electromagnetic waves.

Its energy is described by the Planck-Einstein relation:

$$E_{photon} = \frac{h.c}{\lambda} = h.\upsilon \qquad (1)$$

where h is the Planck constant (6.626 x 10^{-34} J.s), c is the speed of light, λ is the wavelength of the photon and the frequency $\upsilon = \frac{c}{\lambda}$.

However, photons that are interacting with matter behave like particles with a defined rest mass. These particle characteristics emerge in case of interactions between photons and matter. These interactions result in a momentum transfer from the photon to the target matter. That is way a photon can also be described by its mass. By equalizing equation (1) with the mass-energy equivalence the mass of a single photon can be calculated:

$$m_{photon}.c^2 = \frac{h.c}{\lambda} = h.\upsilon \qquad (2)$$

$$m_{photon} = \frac{h}{\lambda}.c$$

This definition of m_{photon} enables the determination of the momentum P of a photon with the wavelength λ:

$$|P|_{photon} = m_{photon}.c = \frac{h}{\lambda.c}.c = \frac{h}{\lambda} \qquad (3)$$

Depending on their energy, photons are interacting with electrons of different energy levels ending up in excitation or ionisation of the bombarded atom.
With respect to photon energies coming across in the course of fluoroscopic guide interventions, two main mechanisms of photons in matter are to be discussed:

- Photoelectric effect
- Compton (inelastic) effect

4.1.1 Photoelectric effect

The photoelectric effect describes the complete absorption of a photon and the subsequent ejection of bounded electrons (called: photoelectrons). Although, in case of this energy any electron may be involved, electrons located at the inner shells (K-, L-shell) of the atom are most likely to be dislodged. The ejection of photoelectrons results in a temporary ionisation of the bombarded atom (Figure 3).

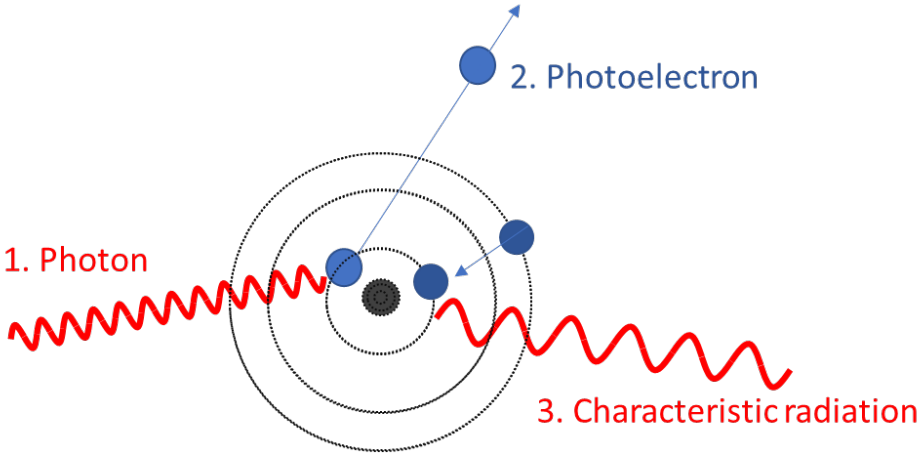

Figure 3: Schematic illustration of photoelectric effect

The photon transmits its whole energy (10^4 – $10^{5.5}$ keV) to only one electron. Depending on the energetic level of the electrons, different photon energies are required to overcome the binding energies (E_b) of the electrons to the atom. The energy surplus gets converted to kinetic energy (E_{kin}) for the dislodged electron (Equation (4)):

$$E_{kin} = E_{photon} - E_b > 0 \quad (4)$$

The removement of the photoelectron causes an electron hole resulting in an energetic unstable condition in the atomic shell. To restore stability in the atom, an outer-shell electron fills the vacancy and emits the surplus energy as characteristic radiation. Depending on its energetic quantity, the occurred photon releases another electron (Auger electron) with lower binding energy. Since, the energies of Auger electrons are considered to be low (several hundred electron volts) their range in tissue is limited. Therefore, the total absorption of the initial photon energy is completed.

The probability of occurrence for a photoelectric effect is built upon two factors:

- The initial photon energy E_{photon}
- The atomic Z number of the bombarded material

With regards to photons in the diagnostic energy range (< 150 keV) the probability of photoelectric effect τ occurring is:

$$\tau(h\nu, Z) \propto \frac{Z^n}{(h\nu)^m} \quad (5)$$

where Z is the atomic number of target atom. The exponent n is in a range between 3.6 and 5.3. The exponent m lies within 2.5 and 3.5. Both exponents (n,m) are largest for low atomic numbers. Therefore, an increasing photon energy influences the likelihood of occurrence of photoelectric effect in a negative way. On the other hand, an increasing atomic number favours emerging photoelectric effect. As a result, small deviations of the atomic number do have a substantial impact on photoelectric effect τ. Relating to radiation protection, the absorption of photon energies is of importance. Thus, materials with high atomic numbers, such as lead (Z=82) are often used for shielding materials.

Considering the low atomic number ($Z \sim 7.5$) of human tissue, only at slow photon energies ($h\nu < 30\ keV$) the photoelectric effect is dominating (equation (5)). Therefore, photoelectric effect is of great importance regarding protection from scattered radiation. Regarding the imaging point of view the photoelectric effect plays a very important role concerning the differences of contrasts being visualized on an X-ray image. These gaps of atomic numbers that are caused by the transition from soft tissue to bones but can also be achieved artificially by the application of contrast medias containing iodine or barium (Reich, 1990) (Dendy, Heaton and Cameron, 2001).

4.1.2 Compton scattering

The Compton scattering, also known as incoherent scattering, describes an inelastic interaction between photons and almost unbounded electrons of the absorber material. Compton effect confirms that electromagnetic waves also follow laws of kinematics in the same way as particles do. Due to the collision of a photon with an electron located in the outer shell of an atom, the electron is emitted (Compton electron) and a new secondary photon of lower energy gets scattered (Figure 4). Unlike to the photoelectric effect also the electron gets scattered.

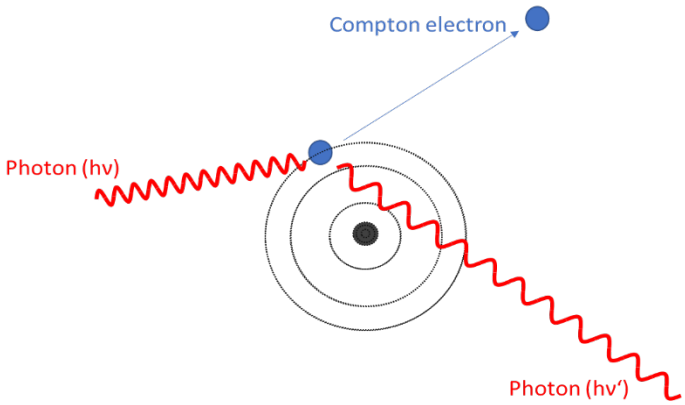

Figure 4: Schematic illustration of Compton scattering

The proportions of energy and momentum transferred to the Compton electron and the scattered photon are labeled with φ (photon) and ϕ (Compton electron).

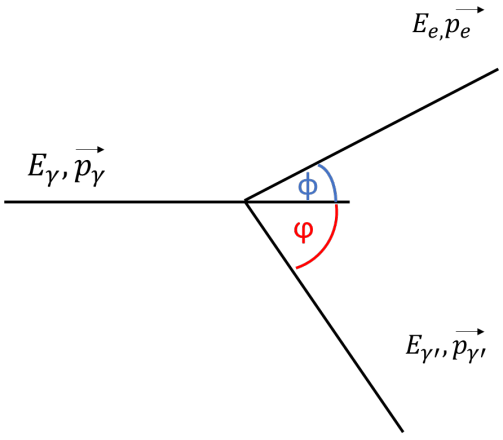

Figure 5: Schematic illustration of the distribution of energy and momentum in course of Compton scattering

Figure 5 shows the distribution of the initial photon energy and its momentum as a function of the scattering angles of the emitted electron and an arisen secondary photon.

Based on the energy conservation law, the sum energies of an inert system has to be constant. The energy of a photon is defined by its wavelength λ (Equation (1)). Therefore, a collision between a photon and an electron ends in a changed wavelength λ (and also the frequency υ) of the photon due to the loss of its energy (Equation (6)).

$$h.\upsilon = E_e + h.\upsilon' \tag{6}$$

Because of relativistic reasons, the total energy of the accelerated electron is the sum of its kinetic energy $E_e$and its mass-energy equivalence E . This mass-energy equivalence E is the product of the electrons rest energy ($E_r = m_0.c^2$) and the Lorentz factor γ ($\gamma = \frac{1}{\sqrt{1-\frac{v^2}{c^2}}}$),

$$E = \gamma.E_r \tag{7}$$

describing the change of mass as a function of velocity v. This results in a definition of the kinetic energy E_e:

$$E_e = E - m_0.c^2 = \gamma.(m_0.c^2) - m_0.c^2 = m_0.c^2.(\gamma - 1) \tag{8}$$

By substituting equation (6) the energy distribution regarding the Compton effect is defined:

$$h.\upsilon = h.\upsilon' + m_0.c^2.(\gamma - 1) \tag{9}$$

$$\frac{h}{\lambda} = \frac{h}{\lambda'} + m_0.c^2.(\gamma - 1) \quad (10)$$

Comparable to the law of conservation of energy also the conservation of momentum has to be valid. In consideration of the relativistic of mass the momentum of electrons described:

$$|p| = \gamma.m_0.v \quad (11)$$

The distribution of momenta from the initial photons to electrons and scattered photons are allocated in the X and Y-axis:

$$X - Axis: \ \frac{h}{\lambda} = \frac{h}{\lambda'}\cos\varphi + \gamma.m_0.v\ cos\phi \quad (12)$$

$$Y - Axis: \ 0 = \frac{h}{\lambda'}\sin\varphi + \gamma.m_0.v\ sin\phi \quad (13)$$

Finally, the energy of the secondary photon as a function of its scattering angle and the initial photon energy is:

$$E_{\gamma'} = hv' = \frac{E_\gamma}{1 + \frac{E_\gamma}{m_0c^2}.(1 - cos\varphi)} \quad (14)$$

Equation (15) shows influencing factors regarding the Compton photon. The ratio of the initial photon energy E_γ to the rest energy of the electron (= 511keV) has a dominant impact on the final energy of the scattered photon. The smaller E_γ, the smaller the denominator and the lower the energetic difference between E_γ and $E_{\gamma'}$ (Table 1).

Table 1: Loss of energy by scattered photons in case of a scattering angle of 45°

Eγ (keV)	Eγ' (keV)	ΔE (%)
20	19.25	3.77
60	53.70	10.51
100	83.63	16.37
200	143.74	28.13
500	252.72	49.46
1000	338.19	66.18

It follows that in the area of small photon energies, the scattering angle $cos\varphi$ has no great effect on the energy transfer. This process represents the interaction of one X-ray photon with one Compton electron. The energy loss shown by Table 1 does not represent conditions of the environment next to the intervention table in the Cath lab. The obtained secondary photon interacts with another electron. This process results in a cascade of interactions depending on the energy of the scattered photon. Finally, the photon energies determined in the scatter cloud next to the scattering body differ significantly to the initial photon energies of the primary X-ray beam. Mean scatter energies of about 35 keV and 45 keV are corresponding to tube voltages of 60 to 70 kV(Munjal *et al.*, 2006). Despite from the scattering body, also the quality of X-ray beams, shaped by additional filtering of copper or aluminium do have an impact on the final energies of scattered photons. Therefore, it is of great importance in the matter of radiation protection that shielding devices such as aprons or glasses are dimensioned adequately regarding the energy spectrum of Compton photons. Due to the collision between a photon and the Compton electron, energy gets transferred from the primary photon to the target electron. Therefore, the secondary photon shows less energy. Since, the energy of a photon is defined by its wavelength λ or frequency ν a wavelength shift has to take place:

$$\lambda' = \lambda + \frac{h}{m_0 c}(1 - cos\varphi) \tag{15}$$

where λ is the wavelength of the primary photon, $\lambda'$is the wavelength of the secondary photon and $cos\varphi$ describes the scattering angle of the Compton photon. Equation (15) shows that the wavelength shift is independent of the initial photon energy.

The law of conservation of energy and also the conservation of momentum describes the deviation of photon energies as well as their scattering angles. These laws do not describe the probability of these processes. The likelihood of an interaction between a photon and an electron in form of Compton scattering is defined by its cross section. The “Klein-Nishina” equation allows to display the differential cross section for Compton scattering of a photon on an almost unbound electron.

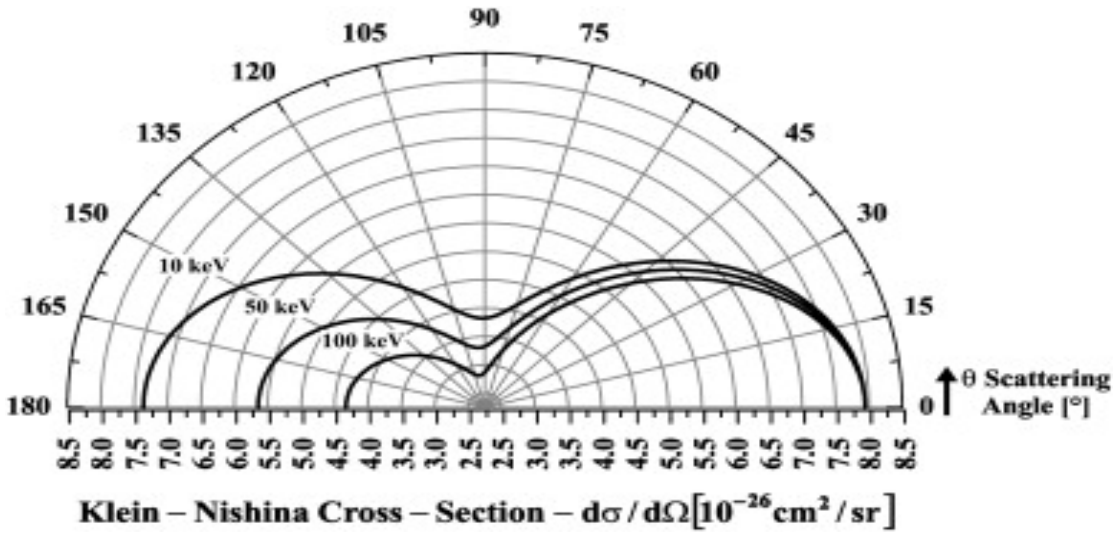

Figure 6: Polar representation of the cross section for Compton scattering based on the "Klein-Nishina" equation (Scannavino and Cruvinel, 2012)

Figure 6 depicts the variation of scattering angle as a function of the incident photon energies. This figure underlines, that the amount of the initial photon energy is linked directly. Low photon energies lead to a higher probability of scattering angles greater than 90°. With increasing photon energies, the tendency of backscattered Compton photons decreases. With regards to radiation exposure this issue is of high importance.

The probability of Compton scattering is defined by the Compton attenuation coefficient.

$$Compton\ attenuation\ coefficient = \frac{density}{energy} \tag{16}$$

The tendency of Compton scattering increases with the level of mass and electrons of the bombarded material. A decrease of the initial photon energy has a restrictive impact on process of Compton scattering. Besides of further influencing factors, the Compton effect dominates in a range of photon energies between 25 keV and 25 MeV. In contrast to photoelectric effect the atomic number has no effect on the Compton attenuation coefficient.(Krieger, 2010)(Reich, 1990) (Scannavino and Cruvinel, 2012)(Pavlovic, 2012)

4.2 Types of Dosimeters

In course of following experimental setups various dosimetric issues were treated. Therefore, different types of dosimeters were in use:

- Ionisation chamber
- Thermoluminescent dosimeter
- Semiconductor dosimeter

4.2.1 Ionisation chamber

The principle of ionisation chambers is the detection of generated electrons and positive charged ions resulting from interactions between charged particles and the filling gas of the ionisation chamber (Figure 7). These dosimetry devices are able to detect and measure different types of ionizing radiation such as X-rays, gamma rays and beta particles.
The basic construction of an ionisation chamber is similar to a plate capacitor. Two contrary charged electrodes (anode, cathode) are creating a defined electric field in the gas-filled chamber. In general, the cathode is represented by the wall of the ionisation chamber. The anode is a wire placed in the centre of the chamber. Electron-ion pairs, created in cause of ionisation processes are forced towards the electrodes of opposite polarity by the electric field. Therefore, large gas ions do migrate towards the wall of the detector and the electrons, are collected by the anode. The separation of charges and the motion of ions create an electric current. All gathered charges due to the interaction of radiation, initiate this ionization current getting measured by an electrometer.

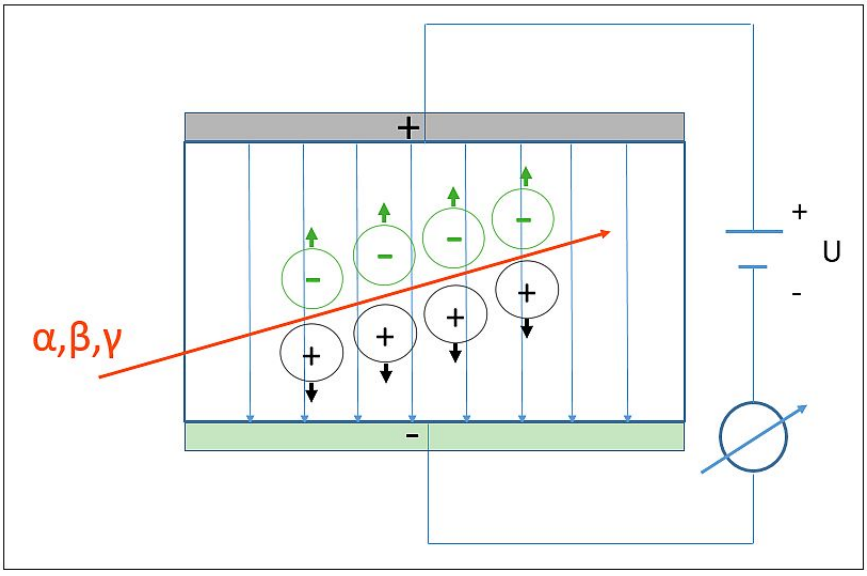

Figure 7: Schematic structure of an ionisation chamber

By altering individual attributes of the ionisation chamber its spectrum of application can be extended. Following characteristics of an ionisation chamber are variable:

- Volume and shape
- Type of filling-gas
- Gas pressure in the chamber
- Electrode voltage

A result of this variability of various parameters, ionisation chambers are suitable for a large spectrum regarding dosimetric issues. Ionisation chambers are used for low-dose detection such as environmental monitoring (dose rate: 0,1 µSv/h) but also are find application in the field of soft beam therapy (dose rate: 10 Gy/min).

Since the electric field stops the recombination of ion pairs in the ionisation chamber, the electric potential between the electrodes has a significant impact on the level of its efficiency. As the voltage between the anode and cathode is not high enough, the rate of recombination of generated ions is too high. The detected signal does not cope with the number of generated ion pairs. Consequently, an increase of voltage inhibits the recombination and an adequate ionisation current gets measured. From this point on the rate of recombination is neglectable. In this area a linearity between the electric potential of the field and the current detected by generated ions is observed. This saturation voltage depends on the one hand on the dose rate of ions and on the other on the distance between the electrodes. Therefore, the number of

generated ion-pairs, the characteristic of the fill gas and also gas pressure in the detector do affect the required electric potential. Smaller dose rates need lower saturation voltage than dose rates of higher extend.
A further increase of the electric potential of the electric field results in an additional kinetic energy of the generated electrons. This causes the creation of another electron-ion pairs via secondary ionisation. This cascade can result in an electron avalanche. Consequently, the ionisation current increases even though the intensity of radiation is constant. Finally, a much higher dose rate is indicated. This phenomenon is called gas amplification. (Krieger, 2013), (Reich, 1990)

4.2.2 Solid state detectors

Similar to gaseous matter, solid states also create charge charrier pairs by interacting with ionizing radiation. To quantify the number of generated electrons and ions an external electric field has to act on this detector. Comparable to ionisation chambers, solid state detectors are paired with a voltage source and an electronic evaluation.
Metallic conductive matters are not suitable for dosimetrically application since it is hard to detect besides permanent existing current flow the additional generated ions. Therefore, electronic isolators with certain electric characteristics are required.

4.2.2.1 Semiconductor detectors

In general, semiconducting materials are electric isolators because of their neglectable electrical conductivity. Under certain external influences, such as ionizing radiation, semiconductors change to electrical conductors.
The key factor behind the conductivity of a matter is the material specific energy-bands structure, resulting in an individual extent of electric conductivity.
The lower band (valence band) is representing electrons implemented crystalline structure of the detector. In contrast to this, the upper band (conduction band) represents the area of free electrons effecting an increasing electric conductivity. In crystal structures, these two levels of connectivity are kept apart by the bandgap. This gap represents a required quantity of energy to shift electrons from the valence band to the conduction band. The amount of required energy to convert a rigid valence electron in a loose conduction electron is

quantifying the electrical conductional properties of a material. Therefore, the extent of bandgap is responsible whether a material is an isolator, and a semiconductor or a conductor. In case of conductors, these two bands are overlapping causing free moving electrons in between the atoms.
In case of an adequate energetic stimulation, the electrons leap from the lower band to the upper band by leaving behind electron holes in the in the valence band. Therefore, the charge carriers are not electron or ions as in the case of ionisation chambers but electrons and holes. These electrons and holes are swept away under the influence of an external electric field. Finally, electronic converts detected charges in a pulse.

Semiconductors are divided in intrinsic and extrinsic semiconductors.
Intrinsic semiconductors represent the pure form of semiconductors such as Silicon (Si) or Germanium (Ge). Both atoms are quadrivalent and create four covalent bonds with their neighbouring atoms. These bonds are at low temperatures stable so that electrons fail to break the valence bond. With an increase of the impact energy, electrons break the bond and are able to carry the current. The left places in the valence bond ("holes") can considered to be positive charged. These processes take place in the entire crystalline structure. By applying an electric potential, electrons are attracted by the positive poles whereas the holes in the valence bond migrate towards the negative pole. The material becomes an electrical conductor. In case of intrinsic semiconductors, the number of free electrons in the conduction band and the number of holes in the valence band are almost in balance. Therefore, hole current and electron current arise to comparable extent. Hence, pure silicon crystals are not used in technologies because of their insufficient conductivity.
For getting an influence on the conductivity and proportions of types of current, intrinsic semiconductors are getting doped. To obtain a doped (extrinsic) semiconductor, impurities are added to the silicon crystal. With respect to technology of doping two types of extrinsic semiconductors are known: N-type semiconductor, P-type semiconductor.

For N-type semiconductors a pentavalent atom like phosphorus, arsenic or antimony are added to the crystal structure of silicon. Due to the 5 valence electrons of the impurities the overhang of one electron results in an almost extra flowing electron in the conduction band. Consequently impurities, used for N-Type semiconductors are electron donors. To achieve an electric conductivity, no further hole in the valence bond is required. Therefore N-type semiconductors are characterized by a dominant electron current.
On the other side, P-type semiconductors are dealing with the third group of the periodic

table like boron, aluminium or gallium. These atoms are trivalent. In contrast to silicon, these impurities do have one valence electron less than silicon. Trivalent atoms accept electrons from silicon atoms. Thus, they are called acceptor impurities. The implementation of these atoms causes a lack of electrons required for covalent bonds to other silicon atoms. The larger number of holes enhances the electron movement to create covalent bonds. As a result, the percentage of free electrons is shrinking since they are used for filling up the holes in the valence bond. By applying an electric field, the holes migrate towards the negative pole to a larger extend than electrons to the positive pole. Therefore, regarding P-type semiconductors the hole current is dominant.

P-type and N-type semiconductors are electrically neutral since there is no initial imbalance between positive and negative carries. By joining these two semiconductors
(p-n junction), an electrostatic gradient arises due to unequal distribution of negative electrons and positive charged hole at interface between P-type and N-type semiconductor. This electrostatic force at their common interface causes movement of electrons from the N-side and holes from the P-side ending up in recombination until a state of equilibrium has been reached. After holes are filled with electrons the electrical neutrality of the semiconductors is gone at. Negative ions at the P-side are opposed to positives ions from the N-side. In this region the positive and negative cancel each other. Consequently, no free charges are available in this depletion area. This area creates an energy barrier between the remaining holes and the free electrons. Any further movement across the junction gets prevented. The diode acts as an isolator. By applying a certain electrical potential with a positive pole at the P-side and a negative pole at the N-side the repelling barriers can get broken down and the diode is conducting.
Comparing a p-n junction with an ionisation chamber, P-side and N-side are representing the electrodes. In the depletion area ionizing radiation creates electron-ion pairs resulting in decreased barrier and an increased movement of electrons and holes. These generated current signals are measured. By altering the extent of the depletion area, the required electrical potential gets changed. The type of N-type and P-type conductor and also the extension of the isolating zone define the application area of a semiconducting detector. (Rizzi, D'Aloia and Castagnolo, 2010), (Krieger, 2013)

Thermoluminescence Detectors (TLD)

Thermoluminescence detectors are generally crystalline structure substances such as ion crystals like lithium fluoride or calcium fluoride. Additionally, these crystals are doped with impurity atoms (titanium, manganese or magnesium) acting as an activator. In case of an interaction with ionizing radiation, the absorbed energy gets stored over prolonged duration due to metastable levels of energy in the crystal. Similar to semiconductors, these processes take place in the area between the conduction and the valence band. A TLD exposed to ionizing radiation creates pairs of electrons and holes. Released electrons migrate from the valence band towards the conduction band. By passing the bandgap, electrons get captured by traps on certain energy levels between the two bands. These electrons are fixed in a metastable state and can return by the implementation of energy such as heat. This energetic impact allows captured electrons getting back to the valence band. In case of recombination, the energy gradient between the trap level and the valence band gets emitted via photon energy. This light can be measured and used to determine the amount of radiation the detector was exposed to. This gets realized by summing up the area under the glow curve. Thus, TLDs are integrating detectors. Depending on the combination of TL-substances the range of detectable energy dose extends from $10^{-7}$to 10^{4} Gy.

In daily clinical practice TLDs are used for in-vivo dosimetry. Furthermore, TLDs are applied for personal dose monitoring because of its capability of long-term memory. (Reich, 1990), (Krieger, 2013)

4.3 Dose quantities

The definitions of dose quantities and their application in the matter of radiation protection were set by the International Commission on Radiological Protection (ICRP) and the International Commission on Radiation Units and Measurements (ICRU). In 2007 the ICRP Publication 103 "Recommendations of the International Commission on Radiological Protection" was published. This publication contains the latest findings regarding biology and physics of radiation exposure.

Dose quantities are necessary to describe radiation fields and their impact on human tissue from a scientific point of view. Depending on the question or issue, dose quantities are classified in three groups:

- Physical quantities
- Protection quantities
- Operational quantities

4.3.1 Physical quantities:

The physical quantities are the fundament of dose quantities. They are defined by the ICRU (Report 60) and deal with the quantitative description of radiation fields of mono-energetic radiations including the particle fluence Φ, the kerma K and the absorbed dose D.

Particle fluence Φ

The particle fluence Φ of a radiation field at a certain point P can be calculated by the quotient of the differential of the expected number of particles dN and a cross-sectional area da, surrounding point P:

$$particle\ fluence\ \Phi = \frac{dN}{da} \tag{17}$$

The unit of the particle fluence Φ is m^{-2} and the cross-sectional area da is thought to be perpendicular to the beam of particles. Therefore, the angle of incidence can be neglected.

Kerma K:

The term Kerma stands for "**K**inetic **e**nergy **r**eleased per unit **ma**ss". Kerma represents the sum of kinetic energies dE_{tr} being transferred by charged particles to the surrounding tissue dm getting initially released by an uncharged ionizing particle such as photons. This implements all processes such as primary and secondary ionisation.

$$Kerma\ K = \frac{dE_{tr}}{dm} \tag{18}$$

The unit of Kerma K is Joule per kilogram ($J.kg^{-1}$). The name for the unit Kerma is Gray (Gy).
Air is of particular importance regarding Kerma, since it is the medium of choice for calibrating monitoring instruments in radiations fields of photons. Therefore, the quality air kerma Ka was established.

Absorbed dose D

The absorbed dose D is defined as the amount of any ionizing energies acting on a subject in a specified point. Not all forms of energy that are leaving the defined volume are considered:

$$Absorbed\ dose\ D = \frac{d\bar{\varepsilon}}{dm} \tag{19}$$

where $d\bar{\varepsilon}$ is the mean energy being absorbed by a subject dm. The unit also Joule per kilogram ($J.kg^{-1}$) and is also labeled with Gray (Gy).

(Horton *et al.*, 2012)(Icrp, 2012)(Wyckoff, 2013)

4.3.2 Protection quantities:

Protection quantities are discussed in the Publication 103 released by the International Commission on Radiological Protection (ICRP). Their focus are the definition of dose limits and reference levels and to optimize radiation protection. These quantities are considering the individual dose radio sensitivity by implementing tissue weighting factors w_T and also a different biological effectiveness for all kinds of radiations represented by the radiation weighting factor w_R. These quantities are risk related and therefore not measurable. These body-related protection quantities are applied to quantify the extent of radiation exposure. Therefore, these quantities are required for radiological protection issues.

Two protection quantities are listed by the ICRP:

- Equivalent dose H_T
- Effective dose E

Equivalent dose H_T :

The equivalent dose H_T stands for the product mean absorbed dose $D_{T,R}$ in Grays in tissue T by radiation type R and the aliquot radiation weighting factor w_R:

$$\text{Equivalent dose } H_T = \sum_R w_R . D_{T,R} \quad (20)$$

Radiation weighting factor w_R is a tool to determine the relative effectiveness of different radiation types for stochastic issues.
The equivalent dose H_T absorbed by tissue T has the unit Joule per kilogram ($J.kg^{-1}$) named Sievert (Sv). The equivalent dose is calculated for individual organs. The task of equivalent dose is to distinguish different types of radiation from their various relative biological effects. Therefore, radiation weighting factors deliver information regarding potential stochastic radiation effects.
In 2007 the ICRP published revised radiation weighting factors w_R (Table 2):

Table 2: Radiation weighting factors according to ICRP Publication 103

Radiation type	Radiation weighting factor w_R
Photon (all energies)	1
Electron, muons (all energies)	1
Proton, charged pions	2
Alpha particles, fisson fragments, heavy ions	20
Neutrons	Continous function of neutron energies

Effective dose E:

In addition to the equivalent dose H_T the effective dose E also includes the individual radio-sensitivity of different tissues. The effective dose is calculated for the whole body. Thus, it is the sum of all equivalent doses to all organs in consideration of their individual radio-sensitivity.

$$\text{Effective dose E} = \sum_T w_T . H_T \quad (21)$$

where H_T is the equivalent dose in the tissue T and w_T is the tissue weighting factor. The ICRP Publication 103 also lists the latest recommended tissue weighting factors w_T (Table 3):

Table 3: Tissue weighting factors according to ICRP Publication 103

Tissue	Tissue weighting factorw_T	Σ w_T
Bone marrow, Colon, Lung, Stomach, Breast, Remainder tissues*	0.12	0.72
Gonads	0.08	0.08
Bladder, Oesophagus, Liver, Thyroid	0.04	0.16
Bone surface, Brain, Salivary glands, Skin	0.01	0.04
	Total	1.00
Remainder tissues*: Adrenals, extraaortic region, Gall bladder, Heart, Kidneys, Lymphatic nodes,		
Muscle, Oral mucosa, Pancreas, Prostate, Small instine, Spleen, Thymus, Uterus/cervix;		

The unit of the effective dose E is Joule per kilogram ($J.kg^{-1}$), and is named Sievert (Sv). (Stadtmann, 2001),(Agency, 2015)

4.3.3 Operational quantities

In case of external exposure of radiation, operational quantities are established. These operational quantities are needed to assess physical quantities. In contrast to protection quantities, operational quantities are measurable. These quantities were defined in the ICRU Reports 39, 51 and 66. They are used to calibrate dosimetry devices for questions regarding area and individual monitoring. In terms of requirements, area monitoring or personal monitoring, different operational quantities are defined:

- Ambient dose equivalent H*(d)
- Directional dose equivalent H'(d, Ω)
- Personal dose equivalent $H_p(d)$

All these operational quantities are based on the common dose quantity, the dose equivalent H:

$$\text{Equivalent dose H} = Q.D \tag{22}$$

where D is the absorbed dose and Q represents a quality factor at a certain point P in the tissue of concern. This quality factor Q refers to the linear energy transfer (LET) that describes the amount of energy departed by ionizing particles per distance. Thus, also secondary ionisation processes within the body are considered.

Regarding area monitoring the ambient dose equivalent H*(d) and the directional dose equivalent H'(d, Ω) are applied to control work places and other areas containing radiation fields. The main task is, to simulate the effect of radiation field in free area in human bodies at a certain depth d. Therefore, the ICRU sphere, a phantom simulating soft tissue with a diameter of 30 cm is in use. The personal dose equivalent $H_p(d)$ is concerned with another dosimetric issue. In contrast to area monitoring quantities the individual monitoring also

includes the backscatter and absorption of radiation in the body. The reference point P is behind the personal dosimeter in the depth of (d).

Table 4: Scope of operational quantities assessing exposure of radiation

Task	Operational Quantities for	
	Area monitoring	Individual monitoring
Controll of effective dose	ambient dose equivalent $H^*(10)$	personal dose equivalent $H_P(10)$
Controll of skin dose	directional dose equivalent $H'(0.07, \Omega)$	personal dose equivalent $H_P(0.07)$

Regarding area monitoring a distinction is made based on the penetration depth of the radiation field. In case of area monitoring, radiation acting superficially (ß-particles < 2 MeV, photons < 12 keV) the directional dose equivalent H'(0.07, Ω) is valid. As a result of the small penetration depth, the additional specification of the beam impact direction (Ω) is necessary. The ambient dose equivalent H*(10) refers to strongly penetrating radiation (photon >12 keV, neutrons). The same applies to personal dose equivalent $H_p(d)$. $H_p(0.07)$ is intended to be utilized for monitoring the dose exposure to extremities.
The determination of dose to the lens of eye assumes a special role. Regarding this organ the directional equivalent dose H'(3, Ω) and the personal equivalent dose $H_p(3)$ are defined (Agency, 2015)(Dietze *et al.*, 2005).

5 Materials and Methods

Since there were no test subjects (human beings, laboratory animals, tissue samples) involved in any experimental setups, informed consent was waived. To prevent any dose exposure of the present personnel, DSA-series were started outside the Cath lab.

5.1 Dosimetry systems

Depending on the measuring points and respective scientific question, different dosimetry devices were used.

5.1.1 Real-time occupational dose monitoring system (RaySafe i3)

The real-time dosimetry system RaySafe i3 (Unfors RaySafe AB, Uggledalsvägen 29 S-427 40 Billdal, Sweden) was an electronic dosimeter system that was especially developed for the detection and visualisation of occurring scattered radiation in the angiography suite. At the time of measurements this system was not available on the market and was provided for research purposes only.

The RaySafe i3-set consisted of four real-time dosimeter, labeled by different colours (here: blue, red, grey and purple), a real-time screen displaying the accumulated dose and the current dose rate detected by each PDM. The present system contained only three functioning dosimeters (red, blue and grey) (Figure 8).

Figure 8: RaySafe i3 dosimetry system

Since three dosimeters were sufficient for following measurements the use of a fourth dosimeter was dispensed with. The PDMs were semiconductor dosimeters, using four silicon diode sensors per device, with different amounts of filtration to enable beam quality calculation. The four sensor elements were placed at the bottom edge of the PDM. Detected signals were send to a signal processing chip. The on-board software calculated the dose values that were displayed on a real-time-screen. The dosimeters were calibrated for a Personal Dose Equivalent Hp(10). Technical relevant key features are listed (Table 5).

Table 5: Main Technical Parameters of RaySafe i3

Key Technical Parameters RaySafe i3	
Operational Quantity	Hp(10)
Energy Dependence	< 25 % (N-series, 40 – 150 kV)
Detection Limit	< 30 µSv/h
Dose Rate Uncertainty	10 % or 10 µSv (40 µSv/h – 150 mSv/h)
	20% (150 mSv/h – 300 mSv/h)
	40% (300mSv/h – 500 mSv/h)

5.1.2 DIADOS PTW Diagnostic Dosimeter T11003, DIADOS Diagnostic Detector T60004

The DIADOS PTW Diagnostic Dosimeter T11003 and the DIADOS Diagnostic Detector T60004 (PTW Freiburg – Physikalisch-Technische Werkstätten Dr. Pychlau GmbH, 79115 Freiburg, Germany) were labelled with CE-0124 in accordance with the Council Directive 93/42/EEC about Medical Devices and fulfilled the essential requirements of Annex I of this directive. Furthermore, these devices fulfilled following standards: IEC 61674, DIN 6809. In course of tube voltages of 40-150 kV, T11003 Dosimeter was designed for measuring X-ray dose, dose rate during fluoroscopy. And also dose per pulse, irradiation time and the total amount of pulses can be monitored.

The DIADOS Diagnostic Detector T60004 was a semiconductor detector. It was designed for measurements in conventional X-ray diagnostics in the range from 40 to 150 kV. The

detector was intended for dosimetry in the X-ray machine's central ray with or without additional absorber. The outer dimensions of the detector were 40 mm x 30 mm x 12 mm. The measuring quantity was air kerma (µGy).

5.1.3 Ionization chamber Capintec PM-500

The ionization chamber PM-500 (Capintec,Inc, Florham Park, NJ,USA) was designed for precision measurement in matters of radiation protection, especially for pulsed radiation. The scope of detectable photon energy ranged from 10 keV to 700 keV. The nominal response was defined with 16 nC/mSv. The nominal sensitive volume was 530 cm^3. The dose values were acquired as photon dose equivalent (Hx).

Figure 9: Ionization chamber Capintec PM-500

The measuring range of dose rate extends from $0.1*10^{-3}$ mSv/min to 200 mSv/min.

5.1.4 PTW Ionization chamber Type 32002

The PTW ionization chamber Type 32002 (PTW Freiburg – Physikalisch-Technische Werkstätten Dr. Pychlau GmbH, 79115 Freiburg, Germany) was spherical shaped and designed for low level measurement of ionizing radiation in radiation protection. The useful region of radiation quality extended from 25 keV to 50 MeV. The nominal sensitive volume amounted 1 litre and offered an outer diameter of 14 cm. The nominal response lay in the area of 40 µC/Gy.(Del Sol Fernández *et al.*, 2016). The chamber voltage ranged from nominal 400 V to a maximum of 500 V. The obtained measuring quality was photon equivalent dose.

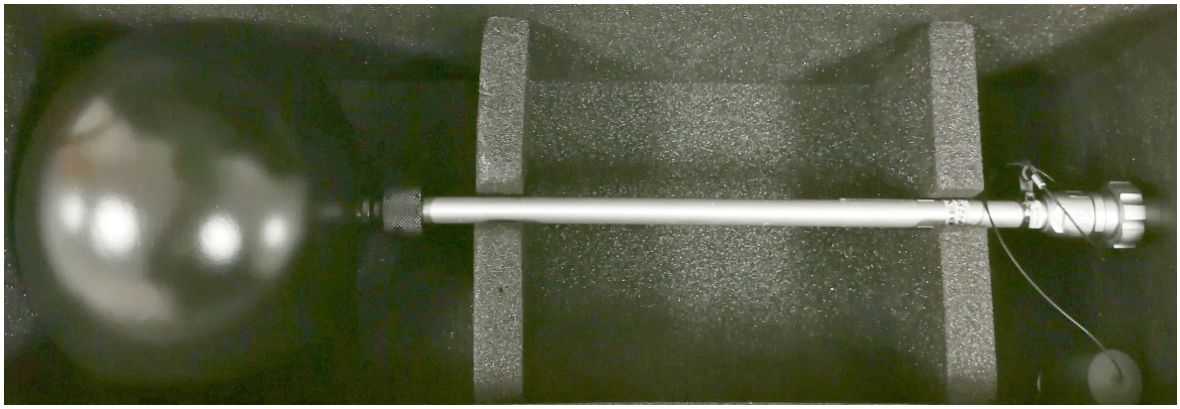

Figure 10: PTW Ionization chamber Type 32002

5.1.5 TLD 100-H (LiF: Mg, Cu, P)

TLD 100-H were thermoluminescent dosimeter based on lithium fluoride. Additionally, these TLDs were doped with magnesium, copper, and phosphorus. These dosimeters were characterized by a proximate tissue equivalence, high sensitivity and excellent dosimetric characteristics such as a good detection threshold. Thus, TLD 100-H were useful for monitoring occupational doses in the angiography suite. (Del Sol Fernández *et al.*, 2016) Because of their small dimensions (3.2 x 3.2 x 0.89 mm) these TLDs were able to be placed very individually. To allow single calibration of all TLDs, they had to be stored in a special acrylic holder that was divided in ten rows labeled with “A, B, C, D, E, F, G, H, J, K, L, M” and ten columns numbered from “1” to “10” (Figure 11). In case of calibration, the whole

setup was irradiated with a predefined dose. Since each TLD chips had its own “address” the determination of correction factors of all TLD chips could be calculated individually.

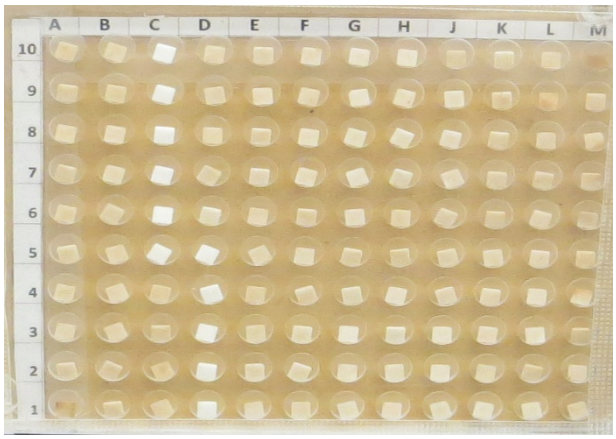

Figure 11: Setup of TLD 100-H chips

5.2 Angiography unit

All experiments were performed on a Siemens Artis zee angiography system (Siemens Healthcare, Erlangen, Germany) (Figure 12) at the Department of Radiology, Division of Vascular and Interventional Radiology at the University Hospital Graz. The angiography

Figure 12: Angiography system Siemens Arits zee

system was floor-mounted and equipped with a rectangular (30cm x 40 cm) amorphous silicon flat panel detector. The detector was provided with a high resolution 2k* matrix (2480 x 1920) with a pixel size of 154 µm and 16-bit digitization depth. The system operates with a high-performance angiography X-ray tube MEGALIX Cat Plus.

Organ specific digital-subtraction angiography (DSA) programs were used to simulate pelvic vascular interventions. An intelligent dose optimisation and beam filtering (Copper filter from 0.0 to 0.3 mm) were applied automatically. Depending on different scattering bodies and the chosen field of view (FOV) the tube voltage was in a range from 58 to 83 kilovolts (kV). The Artis zee system provides an integrated ionization chamber delivering the kerma-area product (KAP) in the unit µGym².

5.3 Scattering bodies

To simulate X-ray absorption and scattering processes during interventional procedures scattering bodies were used (Figure 13):

- Rando Alderson Phantom (Alderson Research Laboratories, Stanford, USA)
- water phantom (according to ÖNORM S5214-1)

Figure 13: Water Phantom (left), Rando Alderson Phantom (right)

The Rando Alderson Phantom was an anthropomorphic soft tissue phantom torso built up on soft tissue-, bone- and lungs equivalent tissue following ICRU-44 standards.
The water phantom was a cuboid (25x25x12.5 cm) made of Plexiglas with 1 cm wall thickness filled with water.

5.4 X-Ray Radiation Protection Lead Glasses

To quantify the extent of protection of X-ray protection glasses during fluoroscopy guided interventions two different models were in use (Figure 14).

Figure 14: MAVIG X-ray Protective Glasses (Type BR 115 left, Type BR 126 right)

The distinction between these two glasses (MAVIG GmbH, 81829 Munich, Germany) were based on different lead equivalents of their glasses (Table 6) but also on a various design regarding the size of the front glasses but also different solutions concerning the lateral X-ray protection.

Table 6: X-ray protection glasses and their specific attributes

X-Ray protection glasses		
	Lead equivalent (frontal, lateral)	**Weight**
MAVIG BR115	Pb 0.75 mm	approximately 110 g
MAVIG BR126	Pb 0.50 mm	approximately 70 g

Based on different designs on various glasses model BR115 and BR126 were different in mass.

5.5 Test setups

5.5.1 Quantification of dose values by using RaySafe i3 under varied conditions

The aim was to compare detected dose values of all PDMs (red, blue, grey) to each other and also to check the RaySafe i3 system against well-known dosimetry systems (PTW ionization chamber Type 32002, ionization chamber Capintec PM-500).
Measurements were performed at different conditions:

Altering dose quantities (Q1, Q2, Q3) were combined with varying distances (A1, A2, A3) between the scattering body (water phantom according to ÖNORM S5214-1) and dosimetry systems.
The three dose quantities were generated by adding extra layers of Plexiglas, 1 cm thickness each. Plexiglas layers were placed close to the flat panel detector.

Table 7: Experimental setup Q1, Q2, Q3

Dose Quantity	Scattering bodies	X-ray exposure data
Q1	water phantom, no additional layers	65.4 kV, 355.8 mA, 0.2 mm Cu-filtering 129 mGy, 1.032 Gy/min, 30.9 ms/F
Q2	water phantom, 3 cm Plexiglas	67.4 kV, 342.4 mA, 0.1 mm Cu-filtering 468 mGy, 3.744 Gy/min, 34.1 ms/F
Q3	water phantom, 6 cm Plexiglas	73.1 kV, 313.9 mA, no filtering 1197 mGy, 9.576 Gy/min, 36.7 ms/F

Three distances A1 (30cm), A2 (60 cm) and A3 (120 cm) were defined between the water phantom and all dosimetry systems. Both, the water phantom and all dosimeters were placed at an altitude of 110 cm. The centre of the water phantom was matched with the central beam of the angiography system.

In all trails the same organ specific (pelvic) angiography program was started. The duration of each DSA-run was 10 seconds and the frame rate was fixed with 7.5 f/s. With respect to changing number of Plexiglas layers the puls length per frame varied (Table 7). Listed air kerma values (Table 7) refer to calculated doses at the interventional reference point (IRP), located on the central axis of the X-ray beam, 15 cm back from the isocentre toward the X-ray tube. Each measurement was performed three times. As a result of increasing air-kerma values (mGy) paired with growing pulse time per frame (ms/F) dose rate values per frame rose with increasing number of Plexiglas layers (Q1: 3.34 Gy/min, Q2: 10.98 Gy/min, Q3: 26.1 Gy/min).

To generate back scattering, resulting in a more realistic initial situation, an additional water phantom was placed behind the PDMs.

Simultaneously with altering PDMs, two ionizing chambers (PTW ionization chamber Type 32002, ionization chamber Capintec PM-500) monitored dose values on the opposite side of the water phantom with a distance of 110 cm (Figure 15).

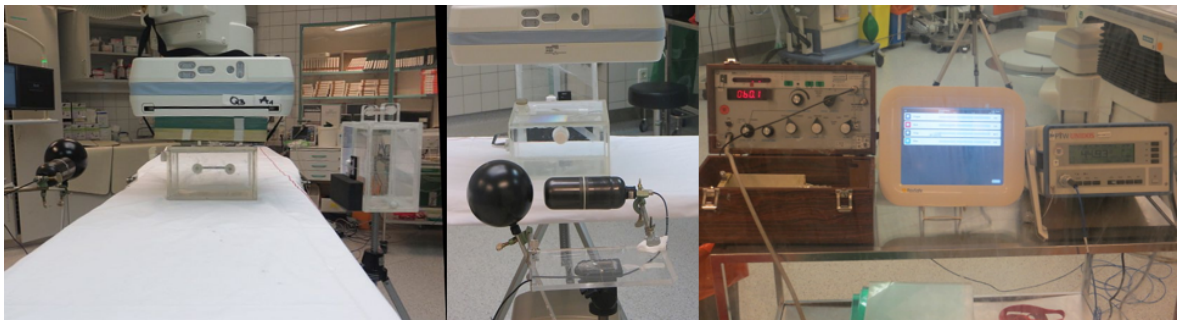

Figure 15: Experimental Setup – Assessment of RaySafe i3

5.5.2 Angle-dependent measuring in horizontal and vertical plane

The deviation of detected dose values with respect to the angle of incidence was tested.

PDMs were tilted in vertical and also in horizontal plane to determine potential dependency between detected scattering dose and the alignment of the PDMs.

A scattering body (water phantom according to ÖNORM S5214-1) was placed on the examination table of angiography system. The centre of the water phantom and the central beam were corresponding. The water phantom and all PDMs were positioned at a height of

109 cm. The distance between the water phantom and the dosimeters was 60 cm (Figure 16).

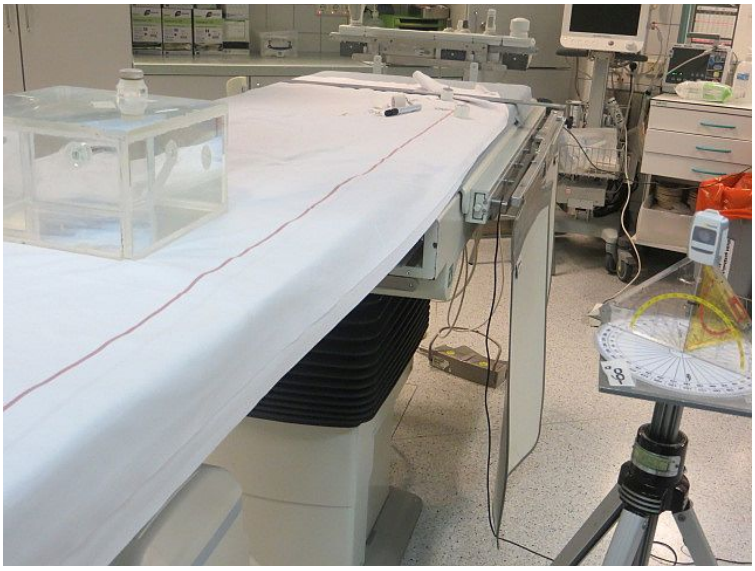

Figure 16: Experimental Setup - Angular response of PDMs in horizontal plane

PDMs were fixed on a mount and positioned on a 360-degree full circle protractor. PDMs were aligned in steps of 15 degrees (-90°, -75°, -60°, -45°, -30°, -15°, 0°, 15°, 30°, 45°, 60°, 75°, 90°) with respect to the water phantom (Figure 17).

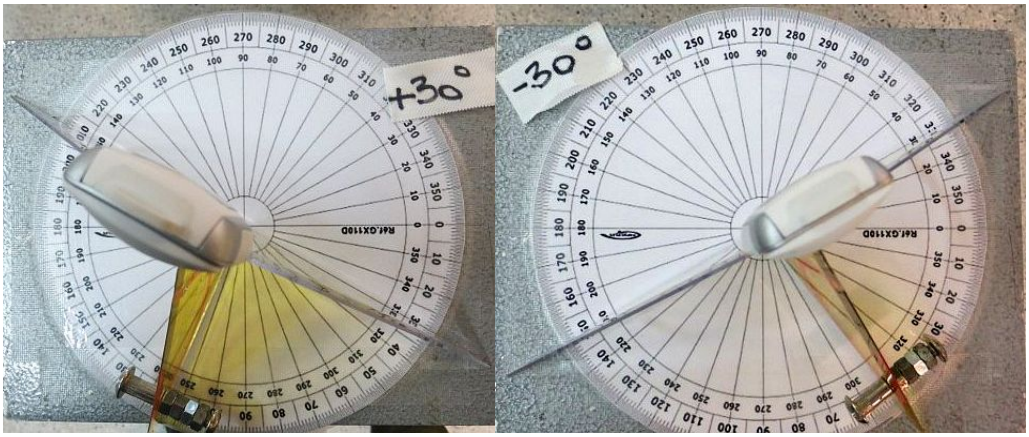

Figure 17: PDM-alignment in horizontal plane

Alignments with negative sign were designated as left orientated position, positive figures represented right orientated PDMs.

The water phantom was irradiated by starting pelvic DSA-programs (63.8 kV, 394.1 mA, 0.3 mm cooper filter) with a frame rate of six frames per seconds for a period of four seconds.

Regarding the vertical adjustment of PDMs, the 360-degree full circle protractor was attached on a stand placed with a distance of 60 cm to the water phantom. Comparable to the preceded experimental setup, all PDMs were tilted vertically in steps of 15 degrees. Positive signed figures represented PDMs clockwise angulations, counter clockwise positioning was associated with negative signed degrees (Figure 18)

Figure 18: PDM-Alignment in vertical plane

X-ray parameters (63.8 kV, 394.1 mA, 0.3 mm cooper filter) were taken over from the prior setup.

5.5.3 Calibration of TLD 100-H chips

To obtain exploitable dose values, TLD 100-H chips were calibrated individually. The main task of the setup was to create an environment that was almost identic to the following test constructions. Scattering bodies and the geometric setup, such as the distances to the dummy were simulated as similar as possible.

To get individual correcting factors for all TLD 100-H chips, an acrylic storage with a loading capacity of 120 TLD chips (Figure 11) was positioned at a predefined height at the front of the dummy. Organ specific pelvic DSA-runs started with a high frame rate to achieve dose values that considerably differed from the background noise. To detect dose values, a Diados Diagnostic Detector T60004 was placed via a special cradle at the same position as the arrangement of TLD chips before (Figure 19).

Figure 19: Experimental setup for calibration of TLD 100-H chips

The detected scattering dose values were displayed by the DIADOS PTW Diagnostic Dosimeter T11003.

5.5.4 Detection of dose values at different measuring points

The aim of this setup was the creation of ratios of the eye lens dose to other measuring points (outer corner of the eye, nasal root, thyroid and sternum) based on measuring data received from different dosimetry systems (TLD 100-H and RaySafe i3). The second task was to

determine comparability regarding scattering dose values between RaySafe i3 and TLD 100-H chips.

Rando Alderson Phantom (Alderson Research Laboratories, Stanford, USA) was the utilized scattering body placed on the examination table of the angiography system. The central beam was focused on the pelvic centre of the phantom. A dummy, consisting of a lead apron and the head-equivalent of the Rando Alderson Phantom was replacing the interventionist. The dummy was positioned in a realistic distance (75 cm) to the centre of irradiation (Figure 20).

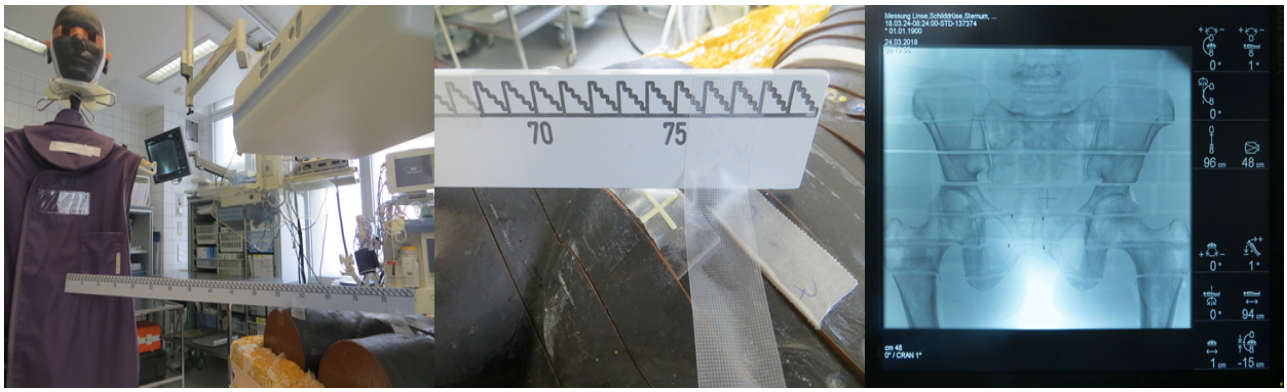

Figure 20: Alignment of dummy and Alderson phantom

TLD 100-H chips were placed pairwise at both lateral corners of eyes, at the nasal root (at a height of 173 cm) and the predefined positions of the thyroid (height: 152 cm) and the sternum (height: 136 cm) (Figure 21).

Figure 21: Placement of TLD 100-H chips at reference points

Three PDMs (grey, blue and red) were placed at the same reference points of the dummy (nasal root, thyroid and sternum) to achieve maximum conformity between both setups (Figure 22).

Figure 22: Comparing reference points - TLD 100-H and RaySafe i3

5.5.5 Determination of dose values at different reference points for three positions in the Cath lab

To evaluate individual dose exposures to working places of different representing professional groups, the dummy was placed typically to the positions of an interventionist, and assisting staff. PDMs were placed at three reference points (nasal root, thyroid and sternum).

Table 8: Experimental Setup - radiation exposure to different working groups

Experimental Setup – Dose Exposure to different working groups				
	HEIGHT			**DISTANCE**
	Nasal root	**Thyroid**	**Sternum**	**Dummy – Scattering body**
Interventionist	173 cm	152 cm	136 cm	75 cm
Assisting staff	173 cm	152 cm	136 cm	115 cm

A Rando Alderson Phantom was used to generate scattering radiation in a realistic manner at a height of 110 cm on the intervention table. To simulate pelvic interventions, the entry point of the central X-ray beam was matched with the pelvic centre of the phantom. In accordance to different working groups, the dummy was positioned in different distances to the scattering body (Table 8). The pelvic DSA-program was started for 7.5 frames per second over 40 seconds.

To determine the impact of electronic magnification on the dose exposure, each experimental setup was carried out using three different magnification factors that were represented by three different sizes of the field of view (FOV).

The standard FOV was defined by a diagonal alignment of 48 cm. Following two FOVs did have a diagonal length of 32 cm and 11 cm respectively (Figure 23).

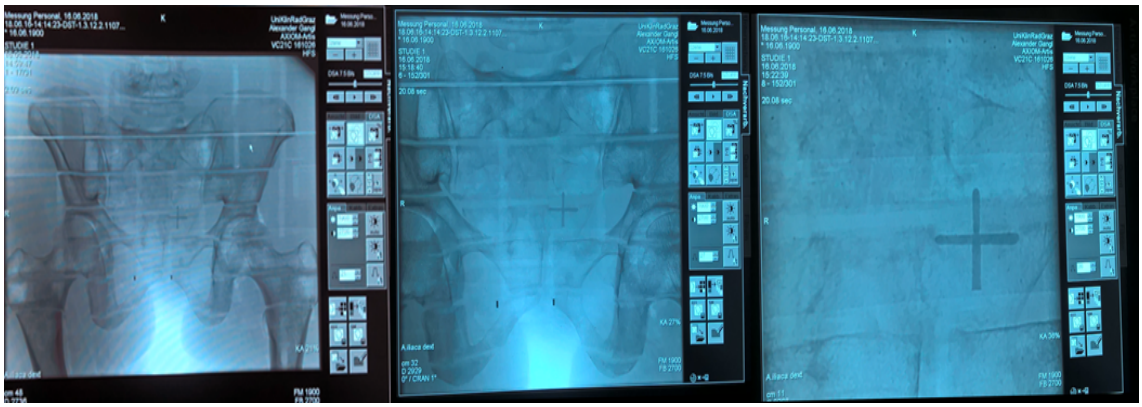

Figure 23: Fluoroscopy images: FOV 48 cm, 32 cm, 11 cm

With respect to the different FOV-sizes, the X-ray parameters were changed by the intelligent dose optimisation of the angiography system (Table 9). All dose rate values listed in Table 9 refer to calculated air-kerma at the interventional reference point.

Table 9: X-ray parameters with respect to altering FOV-sizes

X- Ray parameters depending on magnification level	
FOV-11cm	83 kV, 478.3 mA, 36.8 ms/F, 1130 mGy, 6.1 Gy/min
FOV-32 cm	76 kV, 259.4 mA, 36.8 ms/F, 434.5 mGy, 2.4 Gy/min
FOV-48 cm	70 kV, 288 mA, 34.3 ms/F, 360 mGy, 2.1 Gy/min

5.5.6 Determination of dose reduction factors of protection glasses (water phantom)

The water phantom was placed on the examination table and centred on the irradiation field. The dummy was positioned at a distance of 70 cm from the water phantom's centre.
Initially the head phantom was aligned towards the scattering body. To generate scattering radiation dose an organ-specific pelvic DSA-program was started (63 kV, 352 mA, 0.3 mm cooper filter) with a frame rate of 6 frames per second over 20 seconds. To obtain realistic conditions the head position was turned in steps of 20 degrees (0°, 20°, 40°, 60°) in the right (towards the fluoroscopy screen) (Figure 24). This setup was repeated twice by adding two different designed lead glasses (5.4).

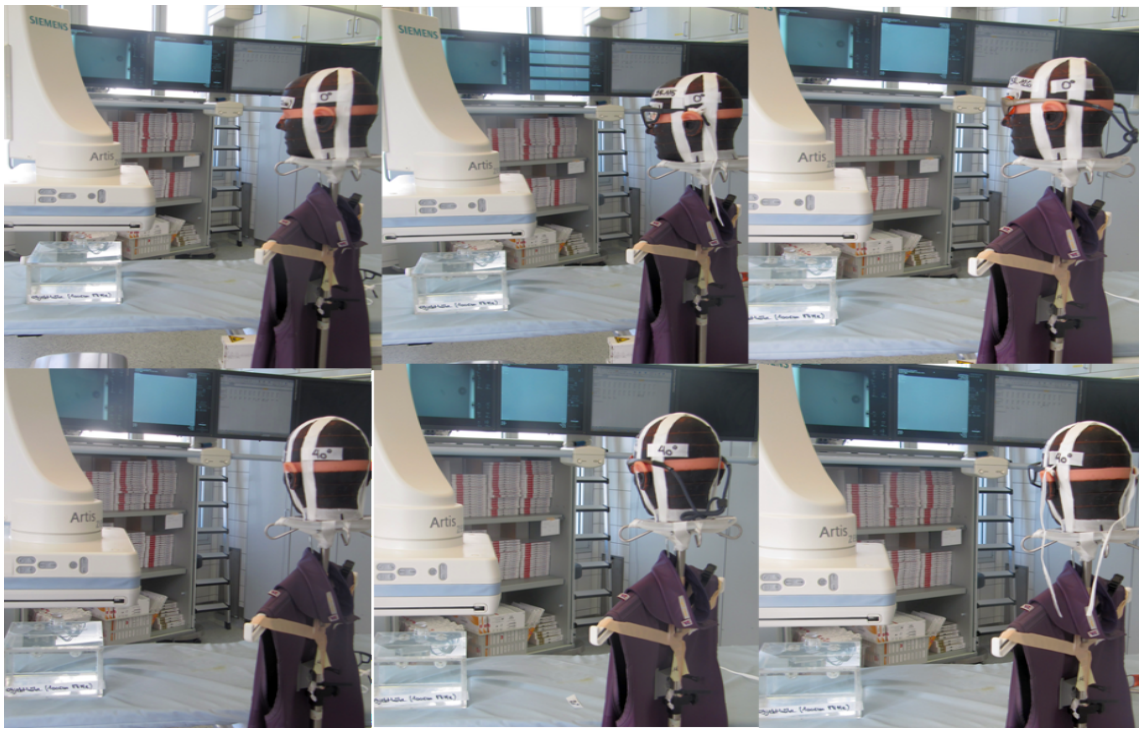

Figure 24: Quantifying the degree of safety of protective eye glasses

To evaluate the effect of various body sizes on the eye lens dose, the eye level of the dummy was reduced from 176 cm to 157 cm. At both eye levels the same test procedures were performed.

To eliminate the dependency of eye level, in another experimental setup the head phantom's orbits were placed at the same level as the centre of water phantom (107 cm). The distance between the head phantom and the scattering body was about 70 cm.

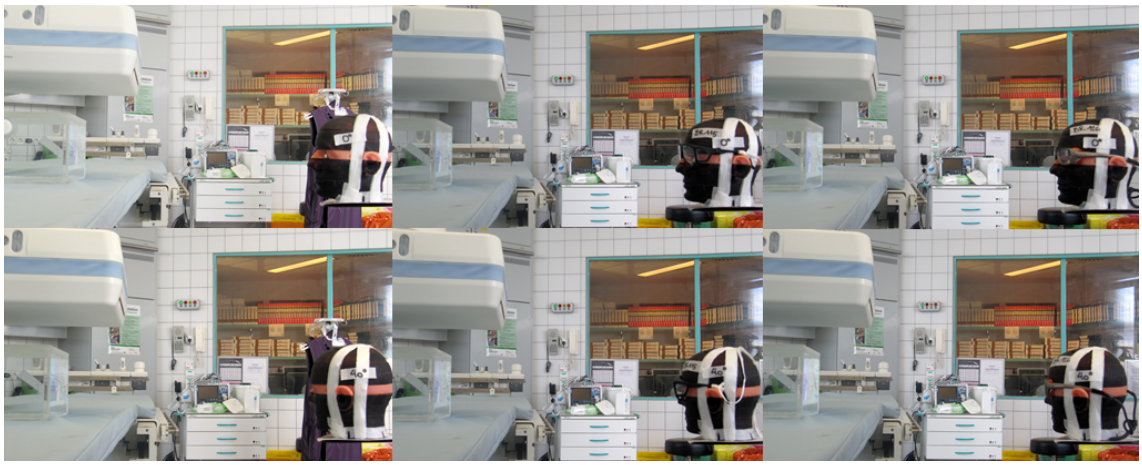

Figure 25: Quantification of the eye lens dose at the same height as the water phantom

Similar to the previous setups the doses to the lens of eye were measured in various positions (0°, 20°, 40°, 60°) (Figure 25).

Because of the right sided orientation of the head phantom, a higher dose exposure to the left orbit especially from lateral was expected. Since there was a limited amount of TLD 100-H chips, the measurement focused only on the left orbit of the head phantom. In each test, procedure the acrylic bracket was filled with three TLD 100-H chips (Figure 26).

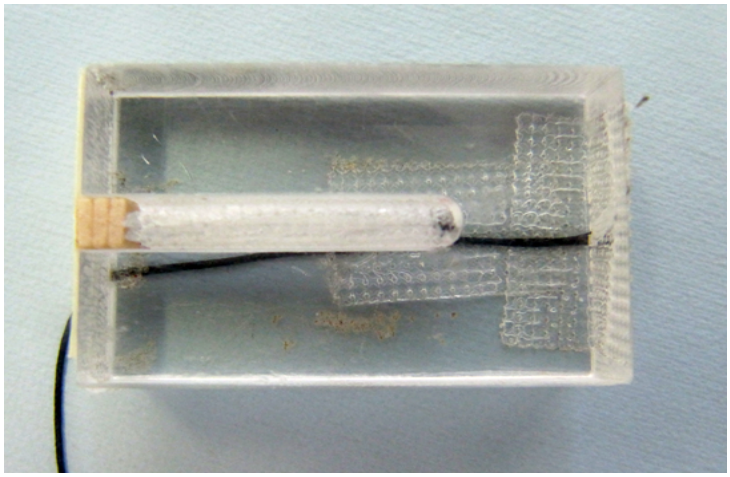

Figure 26: Acrylic bracket filled with TLD 100-H chips

5.5.7 Quantification of the protective function radiation protection glasses (Alderson Phantom)

To approach realistic test conditions for the eye protection devices, a Rando Alderson Phantom was utilized as scatter body. Additionally, a table mounted lower body X-ray shielding (312/DS-039/1, Kenex Limited, CM19 5QB, Essex, England) equipped with a 0.5 mm lead equivalent layer was attached. In accordance with the prior experimental setup (5.5.6), a dummy was placed in 70 cm distance to the pelvic middle of the Alderson phantom (Figure 27). Furthermore, the head phantom was aligned in steps of 20 degrees like before. Measurements were performed at an eye level of 176 cm. Simultaneous to the dosimetry to the lens of eye, PDMs and a DIADOS Diagnostic Detector T60004 was placed at the level of sternum (height = 136 cm) to evaluate the comparability of absolute dosimetry of these two dosimetry devices.

Figure 27: Quantifying eye dose values and comparing dosimetry systems

6 Results

6.1 Unfors RaySafe i3 in comparison with ionisation chambers

The dosimetry data obtained via the experimental setup as explained in 5.5.1, are stated Appendix A.

In all following experimental setups only one PDM-device was in use. Therefore, the comparability of determined dose data of PDM_GREY, PDM_BLUE and PDM_RED has to be verified. Bland-Altmann plots showed that apart from few outliers the differences between all PDMs were found within the limits of agreement (bias ± 1.96*SD) (**Fehler! Verweisquelle konnte nicht gefunden werden.**).

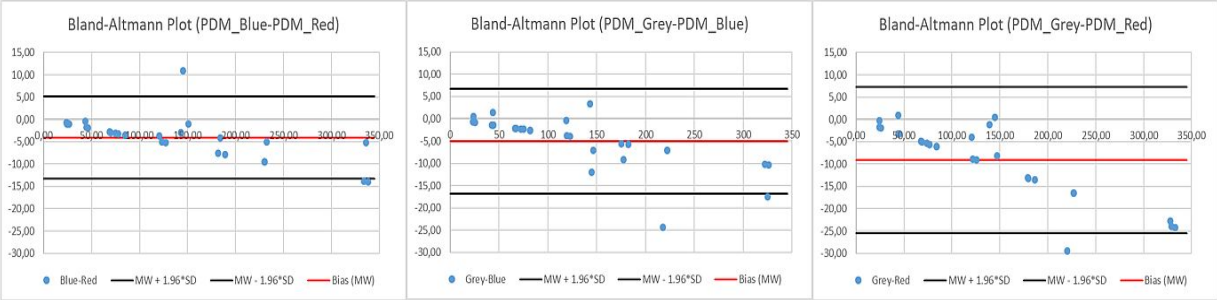

Figure 28: Bland-Altmann Plots describing the agreement of PDMs (Grey, Red, Blue)

Therefore, the dosimeters can be considered to be comparable over all setups (QxAx).
Furthermore, the relative deviations of dose values for all RaySafe i3- detectors standardised to their common mean values did not exceed 10% over the entire bandwidth of measurements and setups (Figure 29). Based on the results shown above, the dosimetric output of all PDMs can considered being almost uniform.

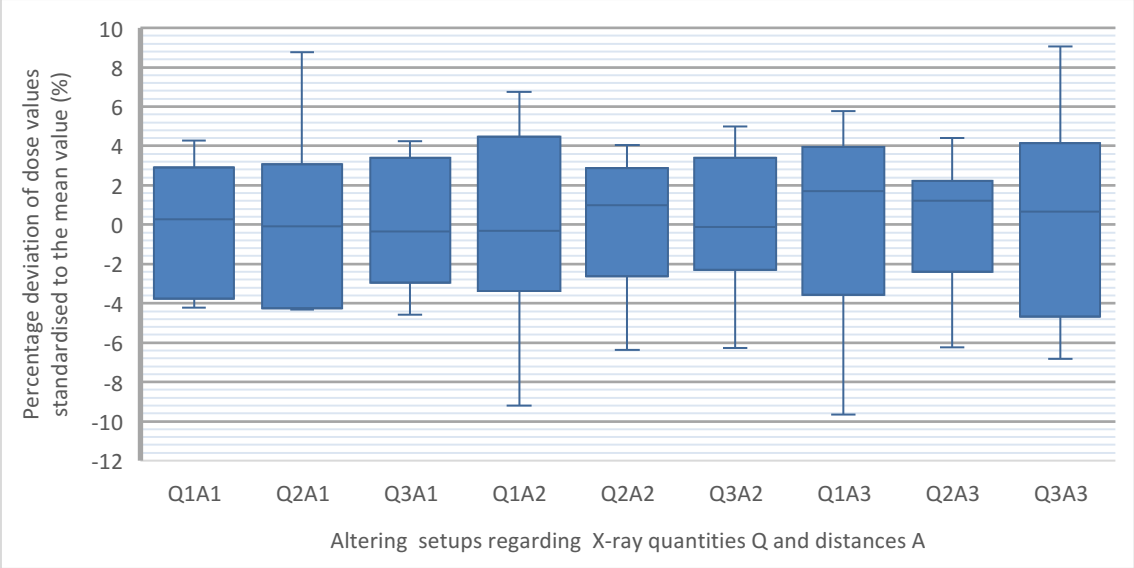

Figure 29: Percentage deviation of accumulated dose values taking into account all PDMs standardised to their mean value considering all setups

For further comparison to other dosimetry systems the averaged dose values (PDM_MEAN) were representing PDM_GREY, PDM_BLUE and PDM_RED.

To compare the dosimetric output of all dosimeters, the ratio of measuring results regarding all dosimeters (PM_500, PDM and IC 32002) including all combinations of distances and X-ray quantities are determined (Figure 30).

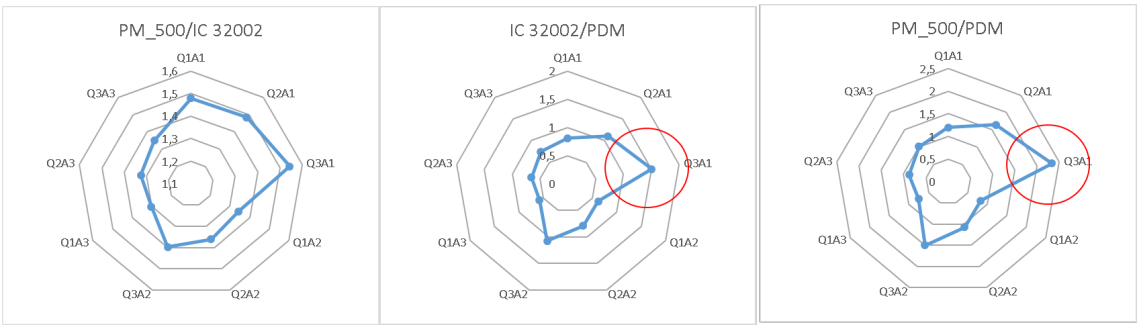

Figure 30: Comparison of dosimetry system by determining the ratio of dose values

A similar performance of all dosimeters would end in a homogeneous ratio of detected value overall test runs. About RaySafe i3 (PDM), Figure 30 shows some irregularities, especially concerning the test setup Q3A1. Comparing ionisation chambers with RaySafei3, at both ratios PM_500/PDM and IC 32002/PDM, a peak is present at the point Q3A1. These peaks result in an increased quotient obtained from dose data measured at the setup Q3A1. Since

the denominators are always represented by the PDM-values, it can be concluded that too small PDM-values referring to test setup Q3A1 were detected.

To verify the validity of measuring values at pre-set distances (A1, A2, A3), the expected dose reduction with increasing distance to the scattering body was to be checked. Scattering doses detected at distance A1 were the initial values of this trail.

Figure 31 displays the individual decrease of detected dose values with respect to altering distances (A1, A2, A3) considering dose energies (Q1, Q2, Q3) for each dosimetry device (PM 500, IC 32002 and RaySafe i3).

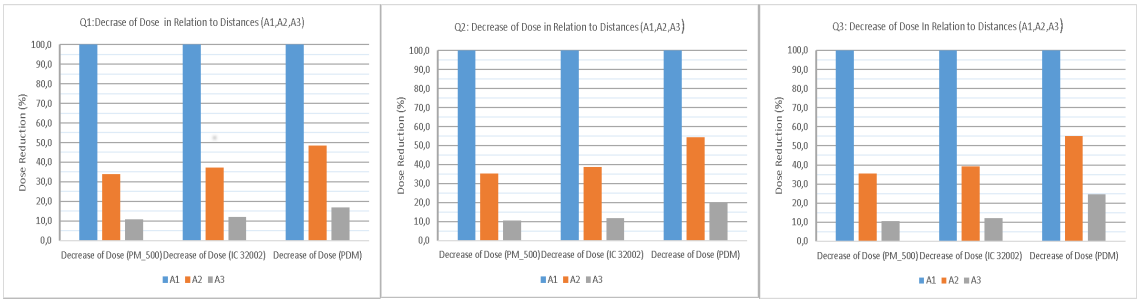

Figure 31: Percentage change of dose as a function of altering distances (A1, A2, A3)

The doses drop from distance A1 (30 cm) to A2 (60 cm) points out a difference between the ionisation chambers (PM 500, IC 32002) and the semiconductor dosimeter (PDM) (Table 10).

Table 10: Dose ratios referring to distances A2 and A1 for all quantities (Q1, Q2, Q3)

	PM_500	IC 32002	PDM
Q1A2/Q1A	0.34	0.37	0.48
Q2A2/Q2A1	0.35	0.39	0.54
Q3A2/Q3A1	0.35	0.39	0.55
Mean	0.35	0.38	0.53

Both ionisation chambers showed similar scattering dose drop-offs as a function of distance A overall dose energies Q. In contrast, PDM obtained in all test runs a larger A2/A1-ratio. This result can be explained by too small measuring results at short distances (A1) with regard to following measuring point at distance A2. This finding is in line with the prior

assumption, that RaySafei3-system may issue inaccurate dose values at small distances coupled with high dose energies.

Figure 32 displays the course of determined dose rates with respect to individual experimental setups. Dose values, gained from ionization chamber PM-500 are the origin for the calculation of dose rates. For calculating the effective radiation time per acquisition run, dose-specific radiation times per frame (ms/F) are used (Table 7). Especially, in consideration to the dose rate uncertainty referring to RaySafe i3 (listed in Table 5) some deviations of dose values have to be expected.

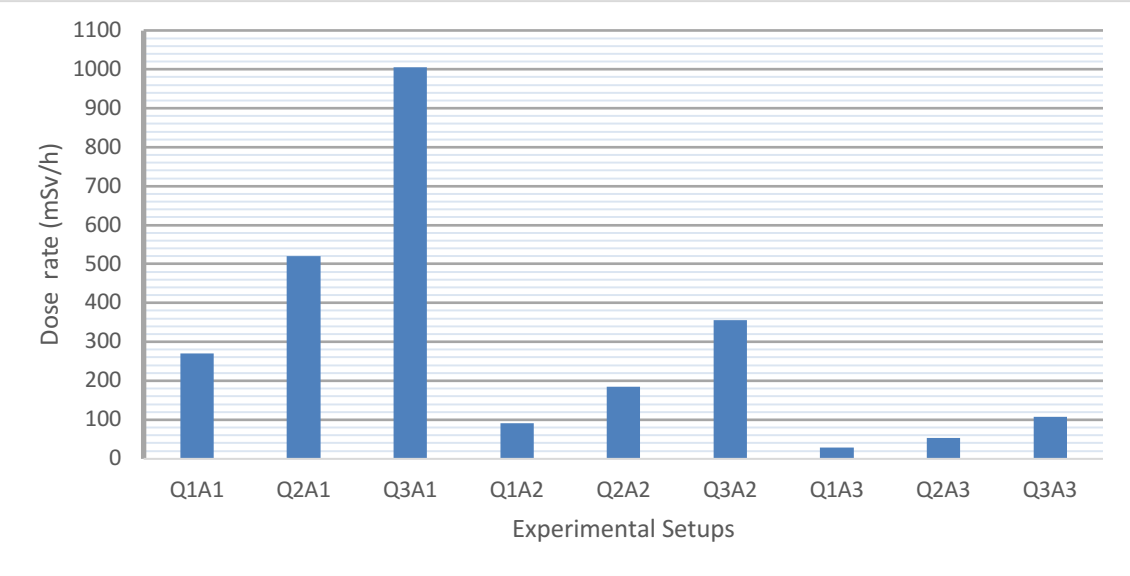

Figure 32: Determined dose rates with respect to altering experimental setups

Table 11 shows the range of dose rates determined within experimental trials. Therefore, a maximum dose rate of 1009.5 mSv/h may explain these too small measuring values regarding the position Q3A1 detected by RaySafe i3 detector as described above.

Table 11: Range of dose rates determined over all setups

Dose rates (mSv/h)		
Mean	**Maximum**	**Minimum**
278.1	1009.5	24.1

To describe the agreement of two quantitative measurements of the same variables the Bland-Altman plot is the method of choice (Figure 33):

Both Bland-Altman plots depict a general comparability between the semiconductor dosimeter (PDM) and ionization chambers (PM_500, IC32002). In almost all experimental setups an accordance between ionisation chambers and the RaySafe i3 system could be determined. The only exception was observed with the experimental setup Q3A1. As depicted in Figure 33, both ionisation chambers are not in line with the personal dosimeter. The combination of the highest dose quantity and the smallest distance to the scattering body (Q3A1) ends up in a substantial gap of detected dose values of ionisation chambers and PDM.

Figure 33: Bland-Altman plot comparing RaySafe i3 with ionisation chambers

To compare dosimetry systems, conversion factors from one dose quantity to the other have to be calculated. First, all dose values considering changing dose qualities Q und distances A (Appendix B) detected by ionisation chambers (PTW ionization chamber Type 32002; Capintec PM-500) are aligned by calculating their quotients and determining their average conversion factor $0.717\frac{\mu Gy}{\mu Sv}$. This factor allows converting dose values measured by ionisation chamber PM 500 from photon dose equivalent Hx (µSv) to air kerma Ka (µGy).

The total mean value of air kerma (Ka) over all dose qualities (Q1, Q2, Q3) and distances (A1, A2, A3) for both ionisation chambers (PM 500, IC 32002) is 148.74 µGy. The mean ratio between Ka-PM 500 and Ka-IC 32002 is 1.003. The determined mean value of PDM_MEAN is 136.10 µSv (Appendix B).
For calculating the conversion factor from the physical quantity air kerma (Ka) to the operational quantity to personal dose equivalent Hp(10) the quotient of these two quantities has to be calculated:

$$\frac{Hp(10)}{Ka} = \frac{136{,}10\ \mu Sv}{148{,}74\ \mu Gy} = 0.915\ \frac{\mu Sv}{\mu Gy} \qquad (23)$$

6.2 Deviation of dose values in dependency of the angle of incidence

An important quality criterion for dosimeters is an accurate detected of radiation dose regardless of the incident angle of the impacting radiation. Subject of this chapter is the horizontal and vertical angular response of the dosimetry-system RaySafei3.

6.2.1 Measurements considering angular modification in horizontal plane

For quantitative and qualitative analysis of all personnel dosimeters, some descriptive statistical key values for all angles of incidence are issued (Appendix C).

When comparing all three PDMs, two research questions need to be tackled. On the one hand uniform dose values for all devices should be determined. Due to the change of the

angle of incidence not only the initial dose value (at 0°), but also the entire range of deviations considering the angle of incidence have to be focused. Each RaySafe i3-detector was irradiated 5 times for each angulation. Figure 34 shows a box-plot diagram considering all obtained measurements for by PDM_BLUE, PDM_GREY and PDM_RED over all angular alignments.

Figure 34: Change of detected dose values as a function of incident angle considering all PDMs (horizontal plane)

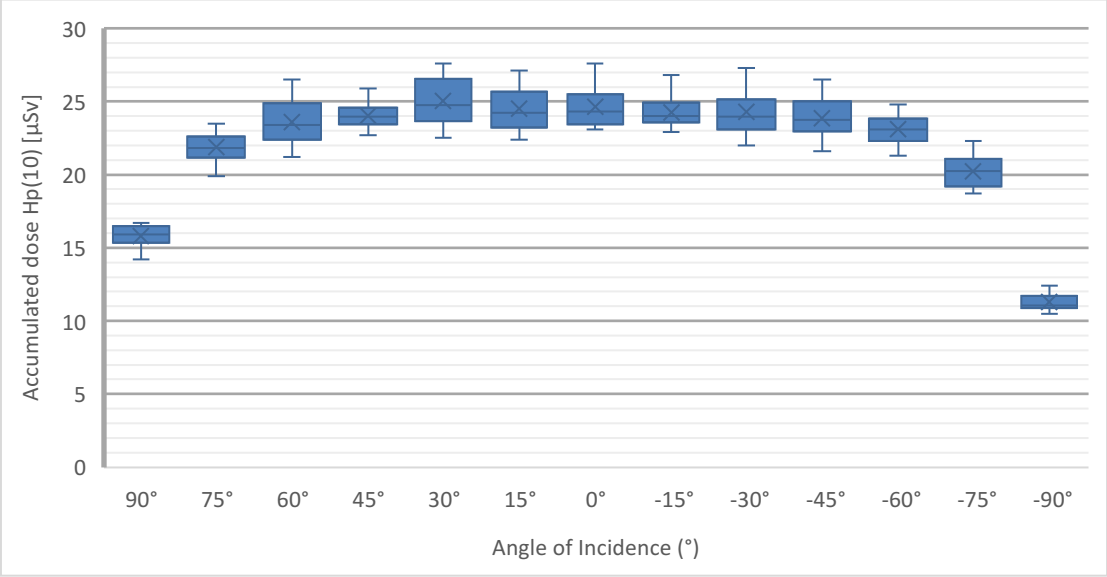

Dose values detected in the area from – 60° to 60° creating an almost common plateau. Within this range, clear deviations from the initial value (0°) are not apparent. Angles of incidence ± 75° and greater cause a decrease of measured values. Incident angles of ± 90 ° resulted in a significant drop off for both sides of orientation (left, right).

A right sided orientation (positive sign) of the dosimeters stands for a higher irradiation of the devices' left side and vice versa. Comparing total sums of dose values (280µSv, 289 µSv and 292 µSv) detected by PDM_BLUE, PDM_GREY and PDM_RED the equivalence of all three devices can be assumed. The maximum value was measured at 0° (27.6 µSv) and the minimum at 90° (10.5 µSv).

Regarding the percentage change of dose values as a function of altering incidence angles, up to ± 75° all dosimeters achieved a deviation smaller than 20% of the initial dose value at 0°. Finally, an alteration of 90° results in measured values of 46% (-90°) and 64% (90°) of the initial dose values (Figure 35).

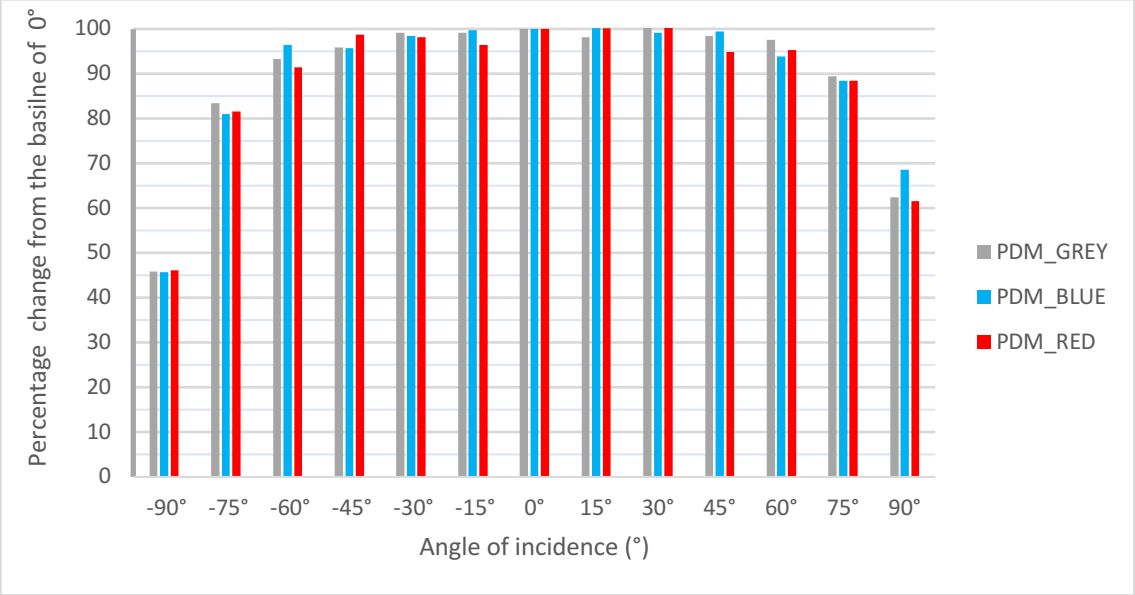

Figure 35: Percentage change of dose values considering the angle of incidence (horizontal plane)

6.2.2 Measurements considering angular modification in vertical plane

Analog to 6.2.1 the deviation of detected dose values considering the vertical angle of incidence were to determined. Detected measurement values including descriptive statistics in accordance with their angulation are listed (Appendix D).

The change of the vertical alignment of PDMs considering the angle of incidence, the dosimetric output needs to be quantified. Again, the change of detected measuring values under changing alignments of the dosimeters have to be considered to verify the dosimetric

uniformity the RaySafei3-system. Positive angle degrees were standing for tilting the dosimeters top towards scattering body. Negative angle degrees mean an orientation of the devices' bottom in the direction of the water phantom. Similar to the previous setting, same organ-specific (pelvic) DSA-acquisition mode was executed over four seconds with a frame rate of 7.5 f/s.

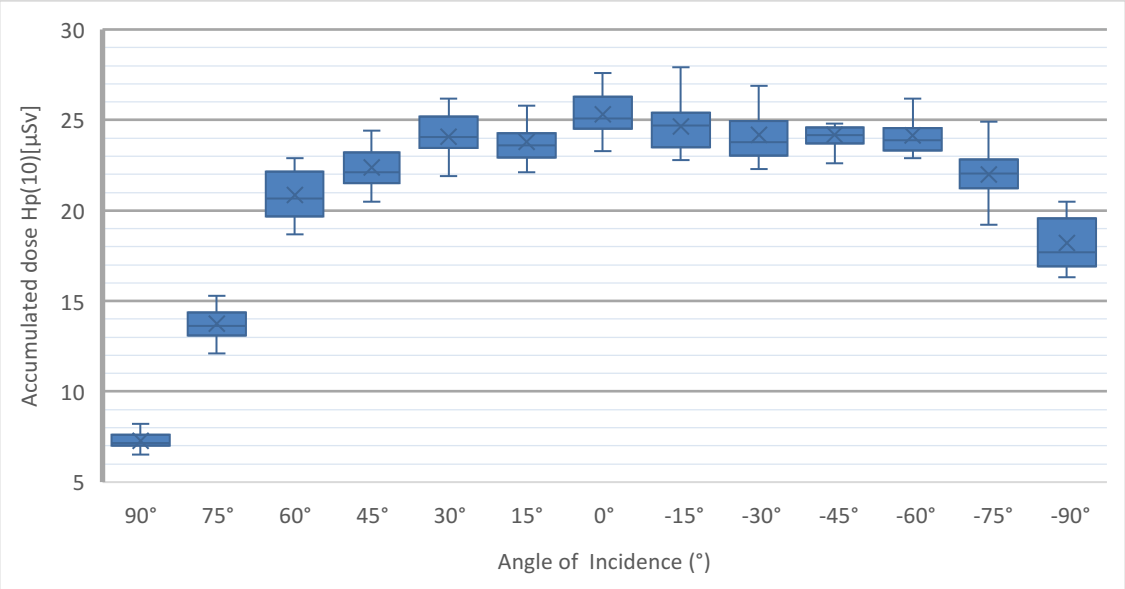

Figure 36: Change of detected dose values as a function of incident angle considering all PDMs (vertical plane)

Figure 36 displays the individual response characteristics of dosimeters considering the vertical angle of incidence. Analogous to Figure 34 shown box-plots graphs include measurements of all RaySafe i3 detectors. An increased angulation, both in positive and negative direction, results in lower measurement values. This fact applies to all tested PDMs. The measurement values ranged from 27.9 µSv to 6.5 µSv. The maximum was detected at an angulation of -15° the minimum at 90°.

Regarding the uniformity of absolute values, PDMs are differing in some angulations to a higher extent. Comparing all tested PDMs by means of the sum of dose values almost comparable results referring to PDM_GREY (280 µSv), PDM_RED (279 µSv) and PDM_BLUE (266 µSv) were obtained. The percentage change of dose values in consideration of altering alignments of the detectors is under influence of the angle of incidence. A higher percentage of detected scattered photons could be assigned to the bottom of the dosimeter.

In contrast to the horizontal plane the percentage change does not behave symmetric to both sides (Figure 37). Angles of incidence with a negative sign showed a higher percentage than their positive counterpart. In case of -90° still about 70% (68.9 – 75.2%) of the initial dose is detected by the dosimeters. The situation was different with 90°, since the mean dosimetric output fell below 30% (26.9 – 30.8%) of the initial dose value. This finding may be explained by the constructive design of RaySafei3-dosimeters, since all sensor elements are placed at the bottom of the device.

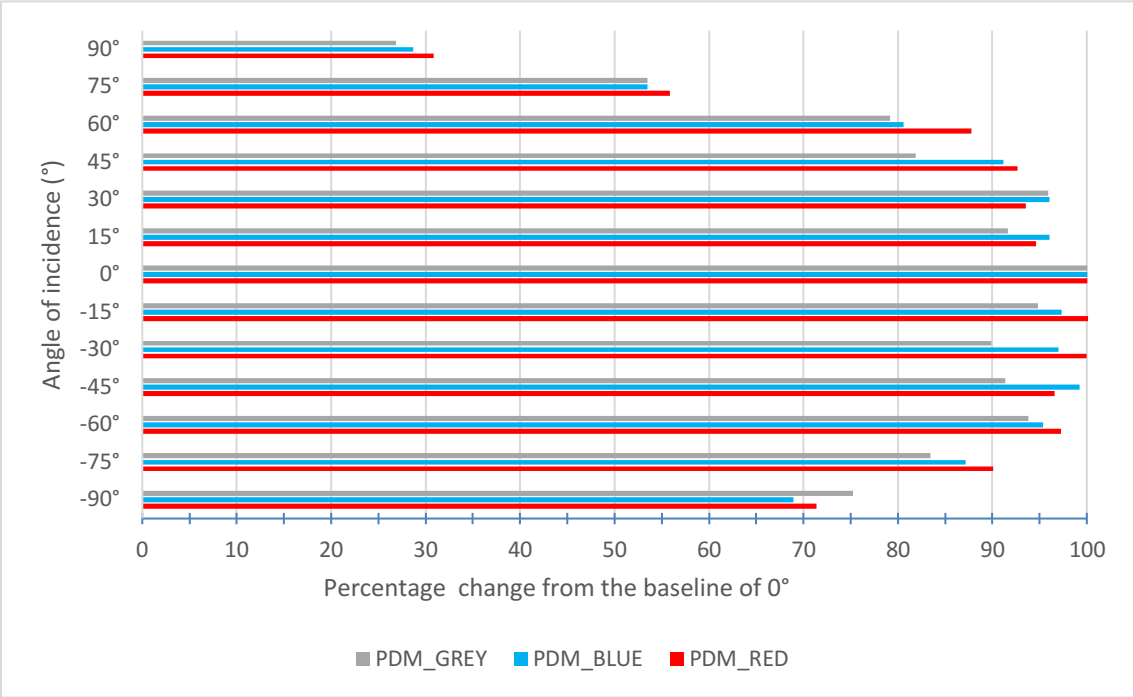

Figure 37: Percentage change of dose values considering the angle of incidence (vertical plane)

6.3 Calibration of TLD 100- H chips

Since TLD dosimeters do not provide absolute dose values, they are relative-dosimeters. Therefore, TLDs have to be calibrated against absolute dosimetry systems. To gain individual correction factors for each TLD-chip, a grid filled with TLD 100-H chip was positioned in a reference radiation field obtaining individual dose responses stated in nano-coulomb (nC). Next another dosimeter (DIADOS Diagnostic Detector T60004) providing absolute dose values given in micro-gray (µGy) was undergoing the same radiation at the same position. Therefore, four DSA-runs with a frame rate of 7.5 F/s over 20 seconds where

started. The total dose response over all four acquisitions was 824.1 µGy. Based on this accumulated dose value individual correction factors µGy /nC for each TLD 100-H chip were calculated (Appendix E).
Since DIADOS Diagnostic Detector T60004 was calibrated to air-kerma (µGy), also dosimetric output received by TLDs were given in the same unit (µGy).

In consideration of the wide spread of initial values (nC) gained from evaluated data, the implementation of a mean correction factor would cause strong undesired effects on the final measurement results (Table 12).

Table 12: Statistics of the distribution of calibrated calibrating factors

	nC	µGy/nC
Mean	33.7	26.7
SD	9.1	9.3
Minimum	11.4	14.1
Maximum	58.4	72.6

Therefore, the generation of individual correction factors (µGy/nC) for each TLD chip is an absolute precondition to assure reliable dosimetry with TLDs.

For confirmation of stable conditions of the X-ray unit, statistical issues of the technical X-ray tube output parameters (X-ray tube potential (kV), anode current (mA), radiation time per frame (ms), dose area product (µGym²) and the detected dose values (µGy) are compiled. All parameters were part of the technical protocol the angiography-system released.

Table 13: Descriptive statistics regarding technical outputs of the X-ray unit and dosimetry system

	Siemens Artis zee				DIADOS
	Tube voltage (kV)	Tube current (mA)	Radiation time per frame (ms)	Dose area product (µGym²)	Air kerma (µGy)
Mean	65.0	347.9	27.9	1752.2	206.0
Minimum	65.0	347.0	27.7	1741.2	204.6
Maximum	65.0	348.0	28.4	1781.5	208.8

All parameters listed in Table 13 show low considerable deviations over all acquisition runs. These stable conditions are essential to guarantee reliable calibrations of TLDs.

The obtained TLD response was stated as nanocoulomb (nC). By creating the quotients of total dose response (824 µGy) obtained from the DIADOS Diagnostic Detector T60004 and the detected values (nC) of TLDs, individual correction factors are gained (Appendix E).

6.4 Comparing dose exposure regarding selected measurement points

Since an immediate dosimetry of occupational lens dose is not feasible, an indirect determination of the radiation dose exposure is required. By creating correction factors from selected measuring points to the eyes, a good approximation regarding the eye lens dose can be achieved. The comparability of TLD-dosimetry with personnel semiconductor dosimeters (PDMs) was studied. PDMs and TLDs are placed at selected positions (nasal root, thyroid and sternum) of the dummy, representing an interventionist.
To ensure sufficiently high dose values the accumulated dose values of three DSA-runs (frame rate: 7.5 f/s over 120 seconds) summed up. Listed data refer to single DSA-runs (Table 14).

Table 14: Descriptive statistics of dose values regarding selected points measured by PDMs (Hp(10))

	Nasal root (µSv)	Thyroid (µSv)	Sternum (µSv)
Mean	519.7	866.9	1006.6
SD	2.7	5.9	4.2
Minimum	517.5	861.8	1010.6
Maximum	522.7	873.4	3019.8

In the next step, TLD-chips were placed in pairs at the outer corners of the eyes and at the nasal root of the dummy's head. Similarly, to PDMs, pairwise TLDs are placed to the left and to the right of the thyroid and sternum and were irradiated under the same conditions.

Table 15 shows that the nasal root is an acceptable measuring point to reflect the mean superficial dose exposures to both eyes ending up in a dose difference of about 18 %. Therefore, this reference point (nasal root – TLD) will be used for further preparations of comparisons between TLDs and PDMs.

Table 15: Descriptive statistics of dose regarding selected points measured by TLDs (Ka)

Region	Mean (µSv)	SD (µSv)	Minimum (µSv)	Maximum (µSv)
Eye corner left	2143.8	121.2	2052.3	2314.1
Eye corner right	1520.4	415.3	1117.7	1960.7
Eye corners mean	1832.1	166.4	1632.2	2006.5
Nasal root	2173.9	240.8	1977.0	2525.1
Thyroid left	3451.1	168.3	3260.0	3667.4
Thyroid right	3485.4	159.9	3360.6	3704.6
Sternum left	4181.1	504.0	3538.9	4594.4
Sternum left	4286.1	287.2	4080.0	4691.0

Since there is a significant dose difference between the left and the right eye corner, the mean values do not allow any conclusions regarding the site-specific dose exposure. Considering Table 15 it can be presumed, that the side facing the scattering body (here: left side) ends up in a higher dose exposure than the averted side (here: right side). This conclusion comes into effect for all reference points being measured bilateral.

To compare dose values received from PDMs and TLDs, radiation quantities have to be unified. Therefore, dose values obtained from TLDs were converted from µGy to µSv by applying the determined correction factor from the physical quantity air kerma (Ka) to the operational quantity to personal dose equivalent Hp(10) (Table 16).

Table 16: Air kerma converted into Hp(10) by using the correction factor 0,915

Region	Ka (µGy)	Hp(10) (µSv)
Eye corner left	2143.8	1961.6
Eye corner right	1520.4	1391.1
Nasal root	2173.9	1989.1
Thyroid left	3451.1	3157.8
Thyroid right	3485.4	3189.1
Sternum left	4181.1	3825.7
Sternum right	4286.1	3921.8

To establish the comparability of these two dosimetry devices the absolute dose values detected at different reference points have to be checked against. Figure 38 illustrates all measuring points representing various dose exposures detected by TLDs and PDMs. Noticeable differences between these two dosimetric devices can be noted

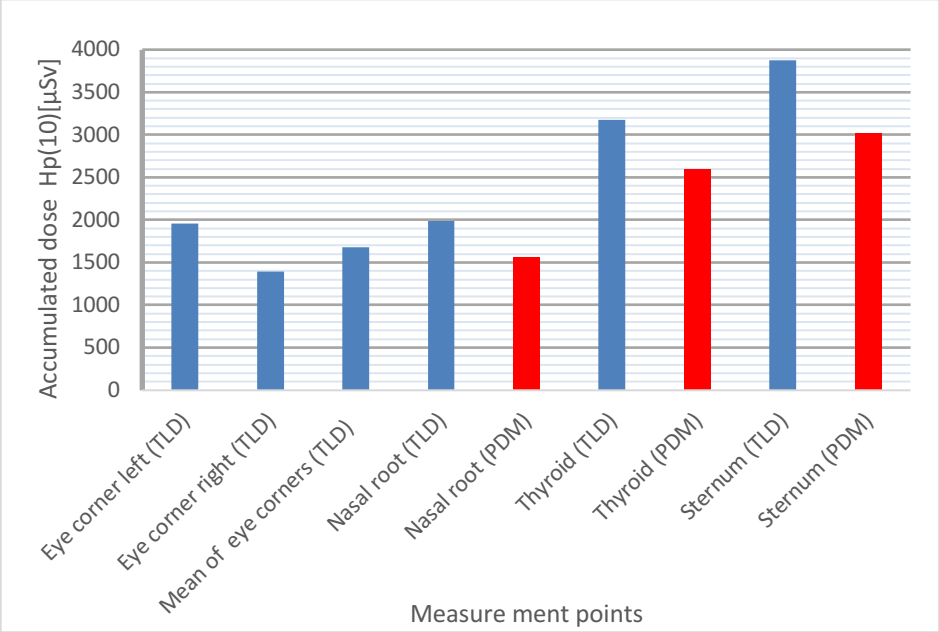

Figure 38: Overview of measurement points detected by PDMs (red) and TLDs (blue)

Table 17 depicts an almost consistent ratio between values gained by TLDs and PDMs in a range from 1.2 to 1.3. Although radiation quantities were unified, detected dose values at all reference points differed at the same rate. This fact may be caused by the conversion factor $0.915\ \frac{\mu Sv}{\mu Gy}$. Its value was detected under deviating conditions.

Table 17: Opposing TLDS with PDMs by comparing absolute dose values generated at three reference points

Ratio TLD-PDM		
Nasal root	**Thyroid**	**Sternum**
1.3	1.2	1.3

With respect to Figure 6, the distribution of dose quantities such as the energetic spectrum, changes with altering measuring points. Since there are differences of absolute dose values

between PDMs and TLDs the ratio of selected reference points has to be created and opposed (Table 18).

Table 18: Comparing dose ratios of reference points gained by TLDs and PDMs

Ratio PDM	
Nasal root/Thyroid	**Nasal root /Sternum**
0.60	0.52
Ratio TLD	
Nasal root/Thyroid	**Nasal root /Sternum**
0.63	0.51

Regarding the dose ratio of referring to reference points, PDMs and TLDs deliver comparable results.

6.5 The impact of magnification mode on the lens dose exposure to the medical staff in the Cath-lab

The application of magnification mode decreases the input field size and therefore the field diagonal shrinks with each additional magnification level. According to increasing magnification levels predefined diagonal lengths were stated (Siemens Artis zee angiography system: 48cm, 42 cm, 32 cm, 16 cm, 11 cm). The impact of increasing magnification levels on occupational lens doses was to investigate. The nasal root was set as a reference measuring point representing both eye in one point (Table 16). Figure 39 shows dose exposure at the nasal root of dummies representing professional groups (interventionist, assistant) placed at typical positions next to the operating table. Dose data were obtained from RaySafe i3 detectors. Three FOV sizes (48 cm, 32 cm, 11cm) are representing three different magnification modes, where 48 cm stands for the initial and 11 cm for maximum magnification.

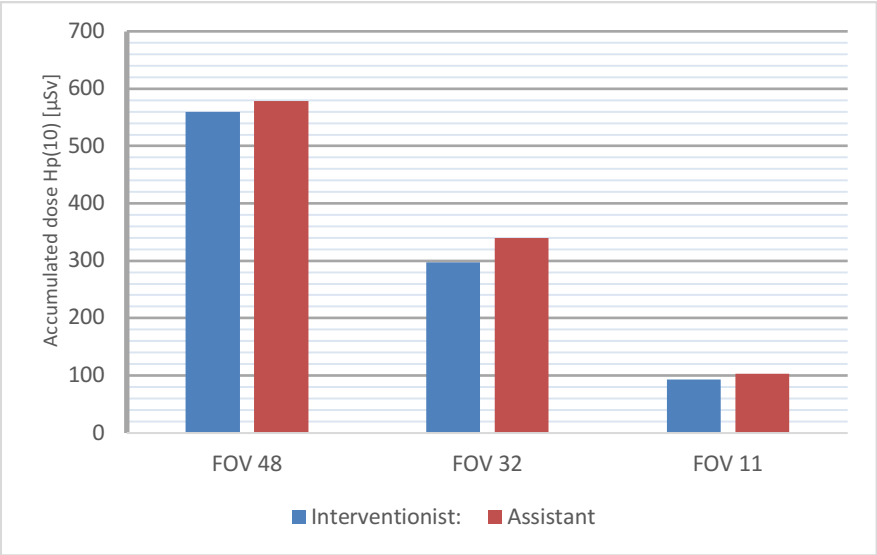

Figure 39: Lens dose values as a function of FOV-sizes referring to different professions.

On the basis of generated data, the impact of magnification levels on the occupational dose exposure can be determined. By setting FOV 48 as the baseline for further calculations, the dose saving extents by using increasing zoom-levels are shown in Figure 40. Referring to both professional groups, "Interventionist" and "Assistant", an increasing magnification level resulted in significant dose drop. The range of decreased dose exposures varied at FOV 32 between 47% (interventionist) and 41% (assistant) and at FOV 11 from 83% to 81%.

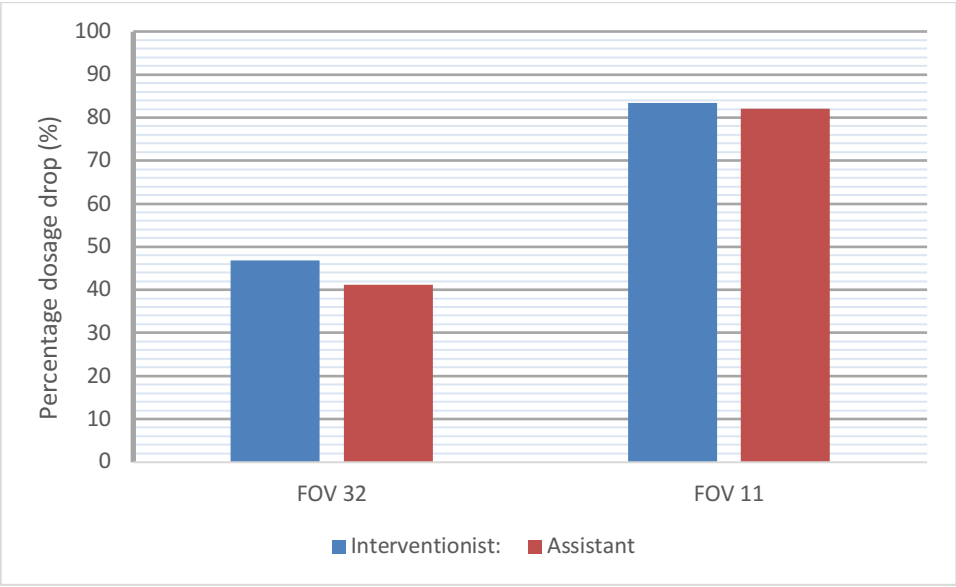

Figure 40: Percentage decrease of eye lens exposure caused by increasing magnification levels

6.6 *Protective effects of radiation protection glasses*

To determine the effect of scattering bodies to the lens of eyes, two similar setups were installed using two different scattering bodies (water phantom, Alderson phantom). To minimize the impact of anatomic structures on the one side and to point out the sole dose reducing extent of protection glasses on the other side, dose measurements were performed on the left eye.

6.6.1 Eye lens dose using a water phantom

To minimize the influence of designs of the protection glasses, the first experimental setup was performed positioning scattering body (water phantom) and the phantom head at the same horizontal level with a distance in-between of 70 cm.

Figure 41 shows dose values measured under varying application of protection devices:

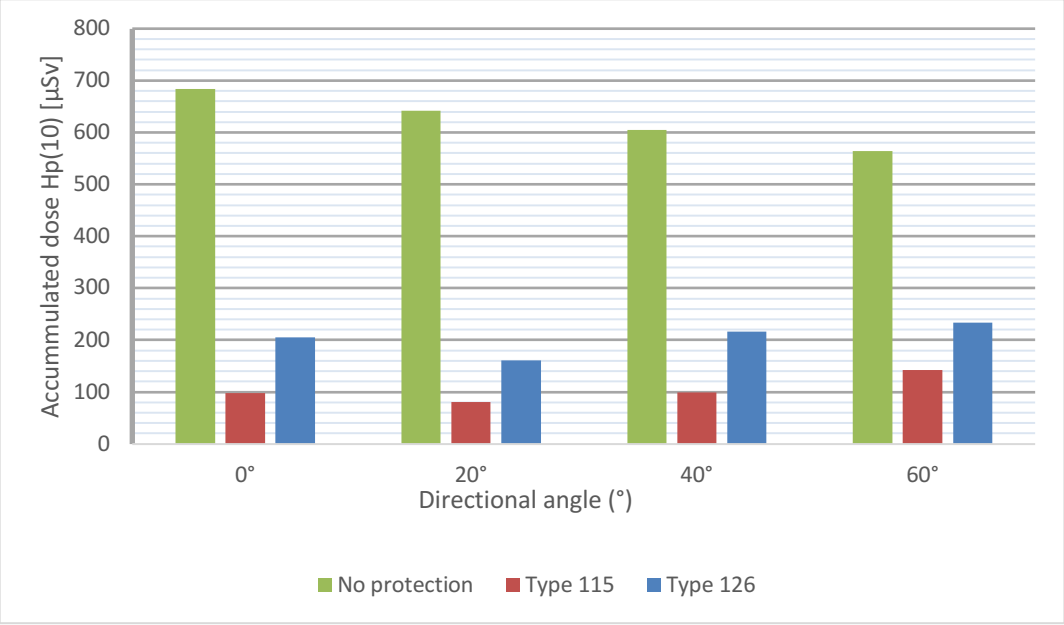

Figure 41: Eye lens dose at the same height (100 cm) as the water phantom

The first trial showed that both protection glasses (Type 115, Type 126) ensure a high protective effect for all alignments of the phantom head with respect to the scattering body.

A comparison between Type 115 and Type 126 showed that there was a significant ($p < 0.02$) difference concerning the protection scattering radiation (Figure 42).

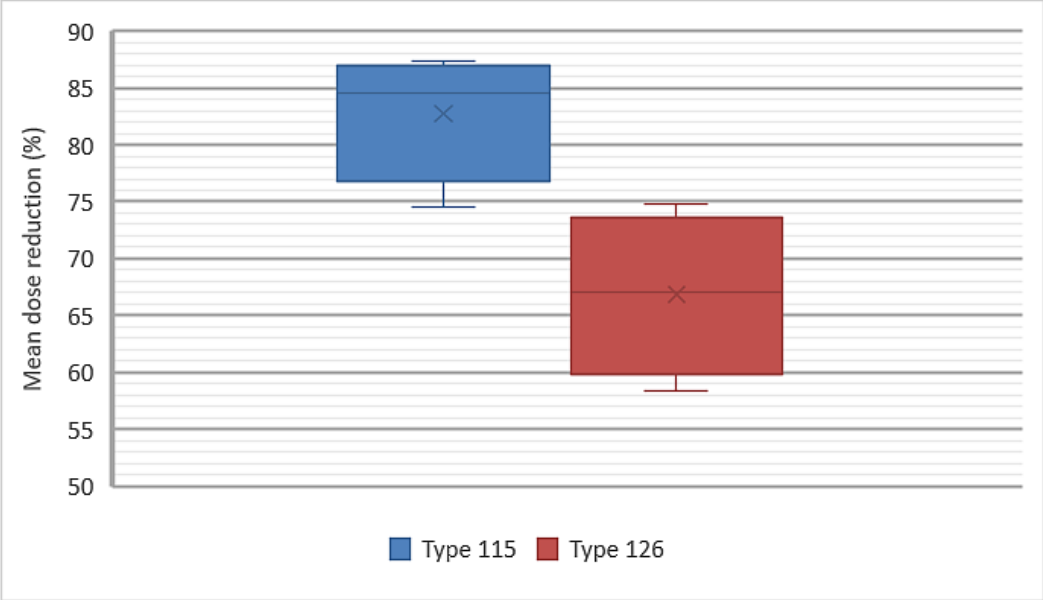

Figure 42: Percentage dose reduction of lens dose at the same height of the scattering body (water phantom)

Considering the mean protective outcome, a notable difference between both glasses could be noticed. Type 115 showed an averaged dose reduction of 82.8%. On the other side, Type 126 reduced the dose by 66.8%.

To quantify the impact of the design of glasses on the dose exposure the lens of eye, two further measurements showing different vertical gaps between eye lens and scattering body are necessary. These setups were implying the protection against scattering radiation affecting from below.

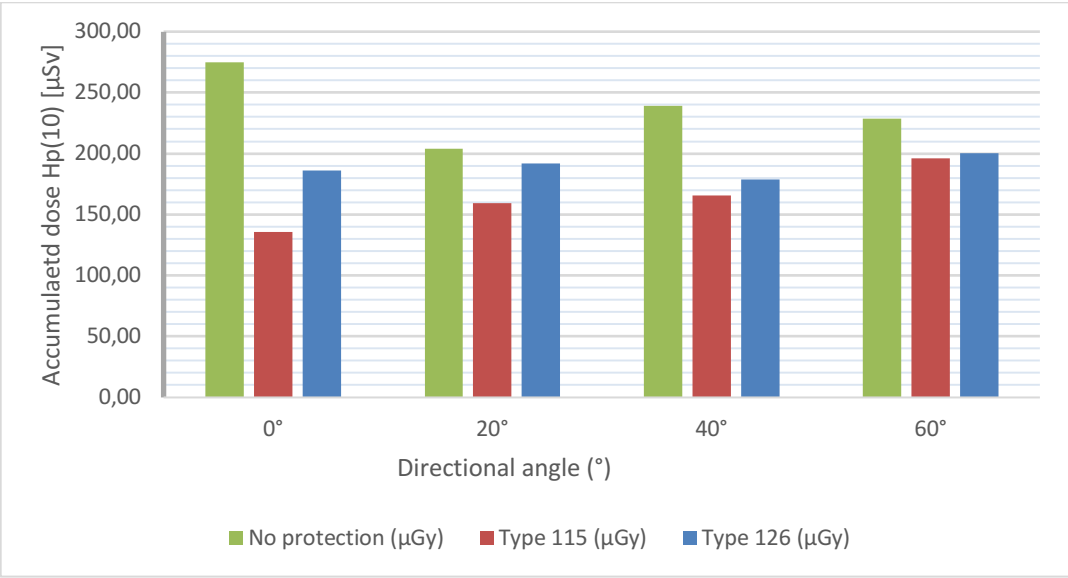

Figure 43: Eye lens dose 176 cm height using a water phantom

In contrast to the preceding experiment the efficiencies of both glasses declined (Figure 43). Also, the directional angles of the phantom head had an additional influence on the detected dose values.

Next test series proceeded the issue determining the impact of the body height on the dose exposure to the lens of eye. Therefore, the setup maintained excluding the eye level. The height was lowered from 176 cm to 157 cm. With respect to the previous setup, Figure 44 displays a major change concerning protective efficiency against scatter radiation. First issues that struck, was the different extent of absolute dose values with respect to changing heights. Over the full range of measuring runs, protected lens of eye received higher dose at a height of 157 cm than at height 176 cm. Of further importance is the big gap between Type 115 and Type 126. Over the entire bandwidth from 0° up to 60°, Type 115 was far superior to Type 126.

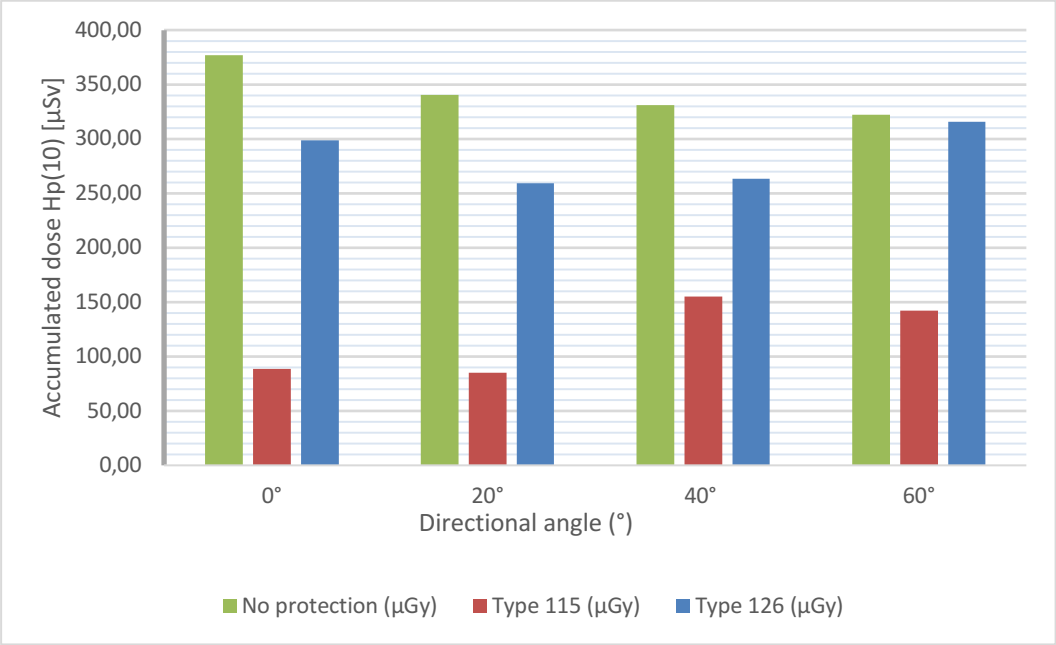

Figure 44: Eye lens dose at 157 cm height using a water phantom

Figure 45 confirms the impaired outcome of both glasses. The mean dose reduction for Type 115 was 27.8 % and for Type 126 was 17.9%. Referring to both glasses, the relatively large range of dose values underlines the strong impact of the viewing directions. Especially, considering the directional angle of 60°, the mean dose reduction for Type 115 is 22 % and for Type 126 the protective outcome does not reach 7%.

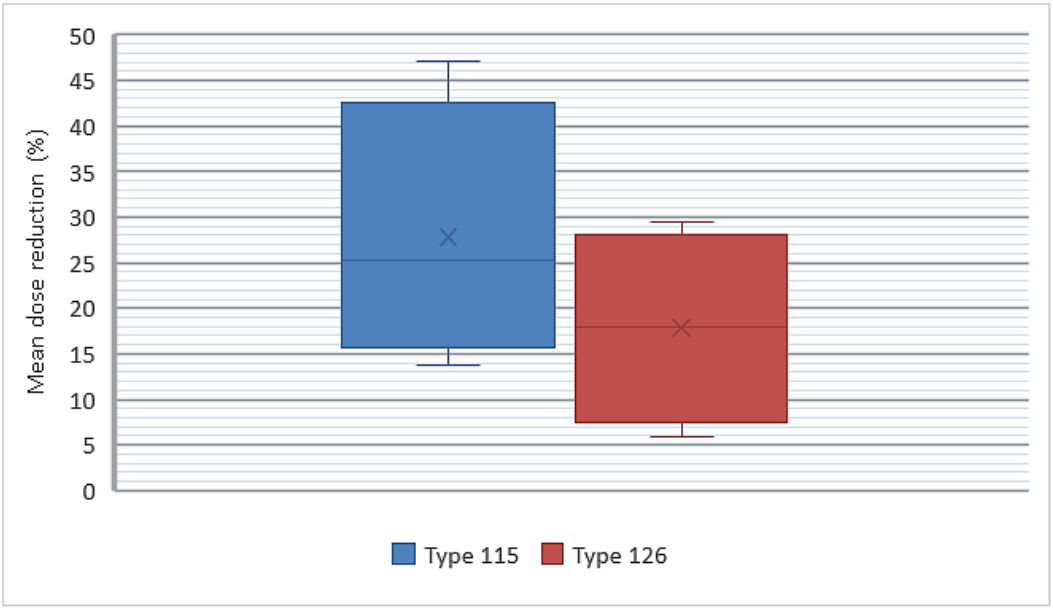

Figure 45: Mean dose reduction of the eye lens dose at 176cm height using a water phantom

Figure 46 depicts a heterogeneous outcome of the mean dose reductions referring on different designs of protection glasses. The mean dose reduction over the entire range of directional angles concerning Type 115 was 65.1 %. On the other hand, the mean protective outcome of Type 126 is 16.8 %.

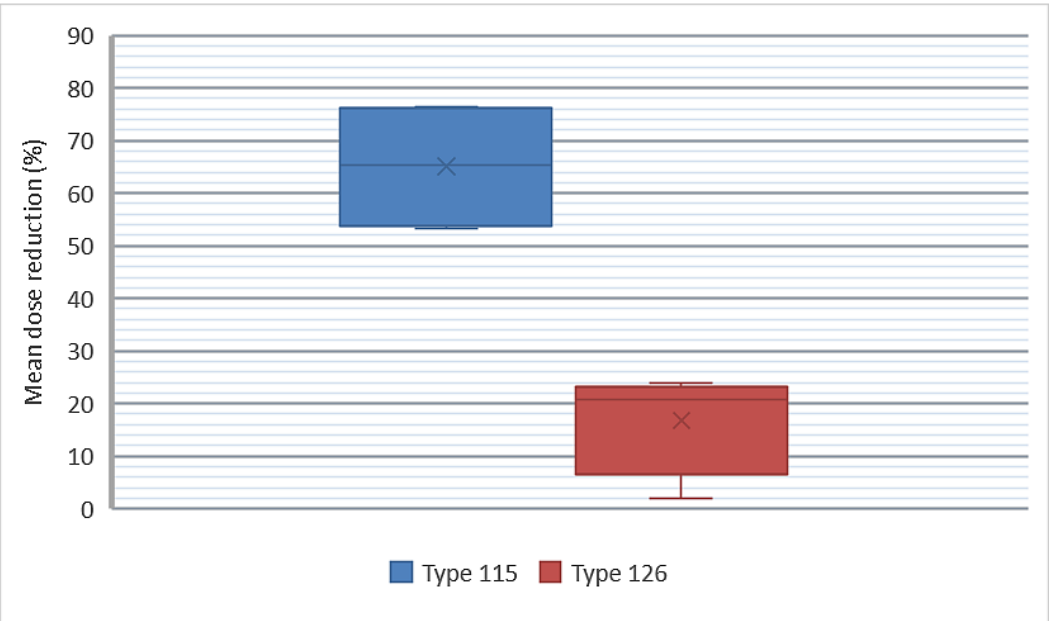

Figure 46: Mean dose reduction of the eye lens dose at 157 cm height using a water phantom

6.6.2 Eye lens dose using an Alderson phantom

For determining the impact of the scattering body on the eye lens dose, the water phantom was replaced by an Alderson phantom. Apart from the scattering bodies the experimental setup remained unchanged. As a result, the initial X-ray parameters of the angiography system (tube voltage, tube current and radiation time per frame) changed (Table 19):

Table 19: X-ray parameters under by changing scattering bodies

Scattering body	X-ray parameters
Water phantom	63 kV, 352 mA, 41.6 ms/frame
Alderson phantom	70 kV, 291 mA, 30.1 ms /frame

Figure 47 shows accumulated lens dose values detected at an eye level of 176 cm. Comparing both types of protection glasses, Type 115 showed over all test runs a better protective performance.

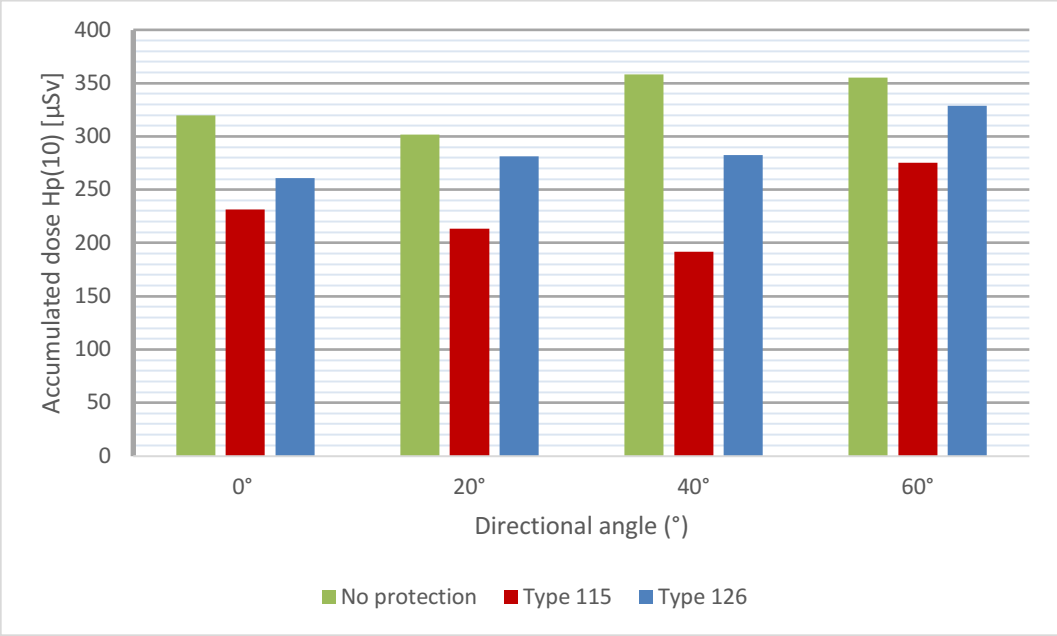

Figure 47: Eye lens dose at 176 cm height using an Alderson phantom

Nevertheless, the protective performance was of low extent for both types protection of glasses. Regarding Type 115 the mean dose reduction was 30.8% and even worse, the protective outcome of Type 126 is determined by a mean dose reduction of 13.1% (Figure 48).

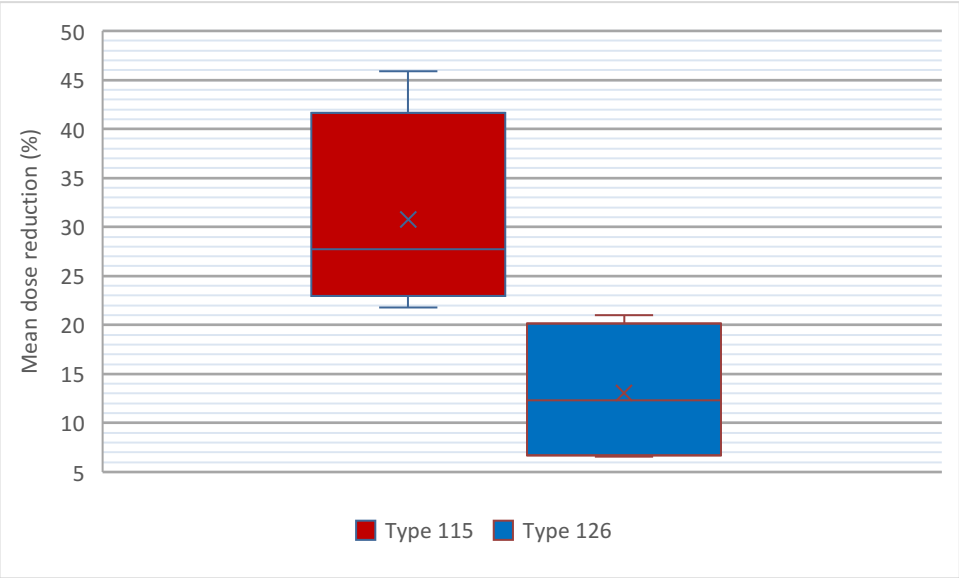

Figure 48: Mean dose reduction of the lens of eye at 176 cm height using an Alderson phantom

To assess the influence of scattering bodies on the dose to the lens of eyes direct comparisons are necessary.

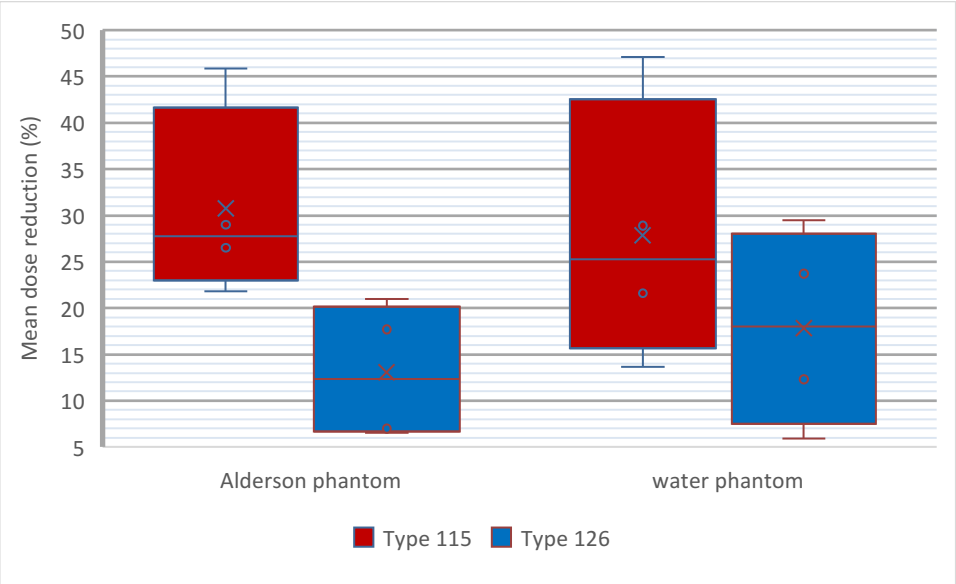

Figure 49: Comparing performance of protection glasses with respect to altering scattering bodies

Figure 49 depicts the superiority of Type 115 over all alignments of the phantom head for both scattering bodies. Nevertheless, depending on the orientation of the phantom head, potential low protective effects for both eyewear models are possible.

Another issue was the impact of scattering bodies on the absolute dose values detected in the orbital region.

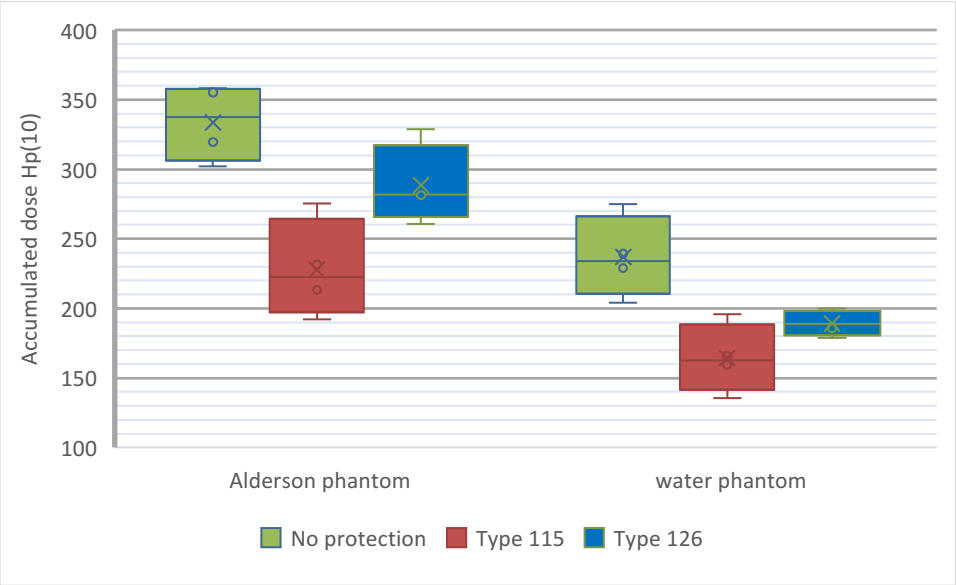

Figure 50: Comparing eye dose values by changing scattering bodies

By comparing test results, based on altering scattering bodies (Figure 50), the influence of scattering bodies on the lens of eye becomes apparent. Considering all test setups, using the Alderson phantom as a scattering medium ended in a significantly higher eye lens dose. The mean ratios of detected dose regarding Alderson phantom and water phantom were for all protection sceneries (No protection, Type 115 and Type 126) almost homogenous and lay between 1.2 and 1.7.

6.6.3 Kerma-area product (KAP) and kerma (Ka) as a function of FOV

Each acquisition run gets achieved in an examination protocol by Siemens Artis Zee system.

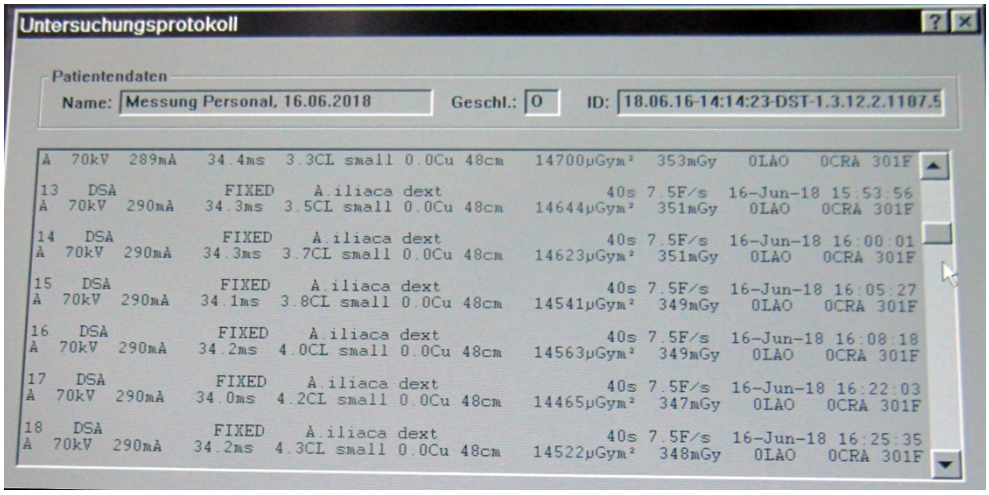

Figure 51: Examination protocol Siemens Artis Zee

Following dose relevant parameters are stored of each acquisition run:

- Tube voltage (kV)
- Tube current (mA)
- Radiation time (ms)
- Filtering (mm Cu)
- FOV-Size (cm)
- Kerma-area product (KAP) (µGym²)
- Frame rate (F/s)
- Cumulative air kerma (CAK) at the interventional reference point (mGy)

This examination protocol allows analysing the interaction of KAPs and FOV-sizes. Figure 52 shows a correlation between FOV-sizes on the quantity of KAP. KAP and FOV-size behave inversely proportional ending reduction of KAP of 45.4% by reducing FOV- size from 48 cm to 32 cm diagonal length. By reducing the FOV from 48 cm to 11 cm, the KAP lessens by 81.6%.

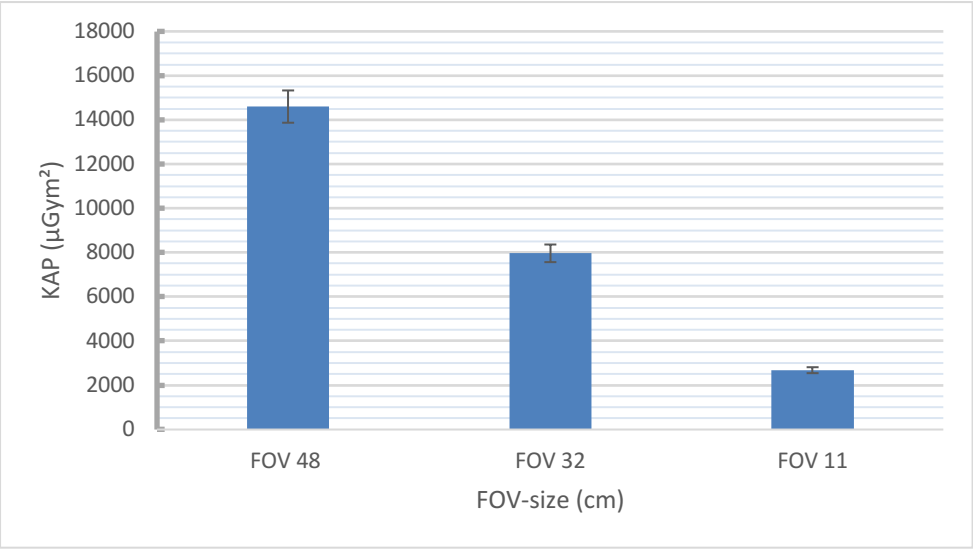

Figure 52: Kerma-area product as a function of altering FOV-sizes

Similar to KAP also the detected air kerma values are affected by the FOV-size.

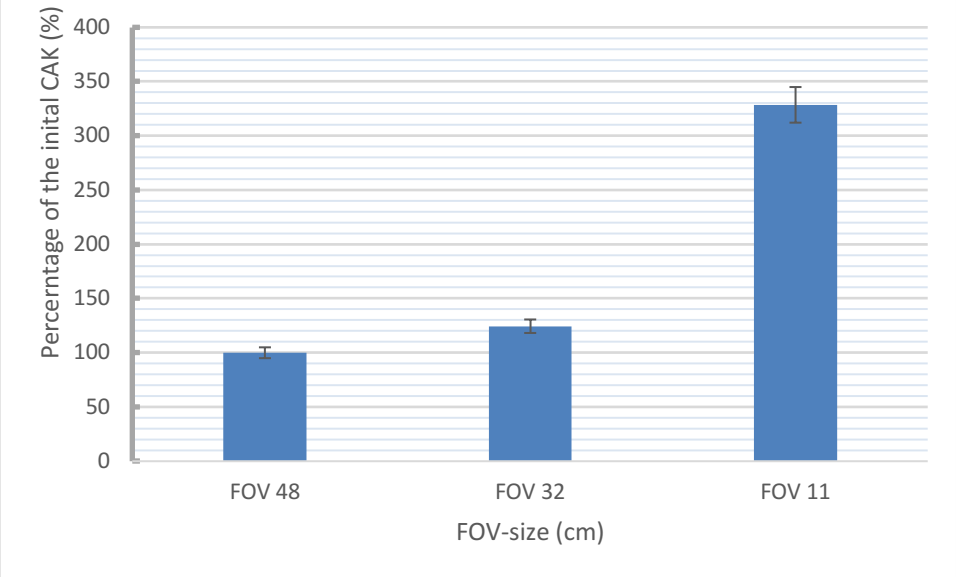

Figure 53: Percentage change of CAK as a function of FOV-size

In contrast to the KAP, air-kerma values (CAK) are increasing in combination with decreasing FOV-sizes. On the one hand, the reduction from FOV 48 to FOV 32 ends in a percentage of growth of 23.8%. On the other hand, changing the FOV from 48 cm to 11 cm diagonal length, the detected air-kerma values raise by 225.3% (Figure 53).

7 Discussion

The main aims of this thesis are to assess the reliability of the real-time personal radiation dosimetry system RaySafe i3, to determine controllable correction factors for eye lens dose measurements obtained from predefined reference points (thyroid, sternum) and to quantify the protective efficiency of leaded radiation protection glasses. Another issue is to quantify the impact of magnification mode on the dose exposure to the medical staff in terms of pelvic endovascular interventions.

7.1 RaySafe i3 system

In the light of discussions concerning dose monitoring of occupational exposure, the International Commission on Radiation Protection (ICRP) and the National Council on Radiation Protection (NCRP) have recommended the utilization of two dosimeters (Icrp, 2012). Usually, personnel dosimeters are worn beneath lead aprons. This method has the effect, that detected dose values may result in an underestimated occupational exposure medical staff receives. The idea of double-dosimetry may result in a more realistic estimation of radiation exposure to staff working in the range of radiation. Furthermore, dosimeters that allow an immediate response, are able to affect the behaviour of medical workers in a positive way (Miller *et al.*, 2010).

The RaySafe i3 system represents the latest generation of real-time personnel dosimetry devices.
During fluoroscopic guided interventions, medical staff from various specialities fulfil a range of tasks at different places in the intervention room. That is why personnel dosimeters have to work reliable, regardless the position of measurement. Consequently, to guarantee a valid detection of dose exposure to the medical staff in the Cath lab, dosimetry devices have to provide low angular dependency.
Caused by the wide range of individual patient sizes, varying X-ray quantities occur. To ensure a reliable detection of scattering dose, the energy response of dosimeters has to be adjusted to photon energies in diagnostic range and below. Finally, the dose rate uncertainty of the dosimeters has to be adapted to the needs in the Cath lab.

Concerning the angular response of RaySafe i3 detectors, measurement results showed an almost symmetrical distribution (Figure 34) with regard to the horizontal plane for all PDMs being tested (Appendix C). Up to an angle of incidence of ± 75°, detected dose values were in range of 80% of the baseline measured at 0°. Beyond 75°, dose values dropped off, so that at -90° and at 90° the RaySafe i3 detected values 54% and 36% lower than at 0° (Figure 35).
Similar to the horizontal plane, measurements concerning the vertical plane also showed nearly identical dose values for all three detectors (Appendix D). Regarding the change of dose values as a function of the angle of incidence, considerable differences were established. Radiation detected from above resulted in higher deviations and uncertainties than measurements focusing on radiation from below. An angle of incidence of -90° (measured downwards) ended in a percentage decrease of about 30 % (25 – 31%). Angles between -75° and 0° stood for a high dosimetric efficiency, same or greater than 83%. Something quite different, however, is the dosimetric output regarding angles of incidence of +75° and more. An angle of 75% resulted in a drop of dose values of 54 % (53.5 – 55.8%) with regard to the initial dose values of 0°. Finally, a percentage decrease of 71% (69.2 – 73.2%) was determined in the case of an angulation of 90°.

Based on these results, RaySafe i3 detectors show smaller deviations of dose values from below than from above. The reason may be found in the constructive design of the detection device. Since all four detectors are placed at the bottom of the RaySafe i3, the dosimetric sensitivity may be biased to detect radiation from top down.
Despite the fact of minor dosimetric sensitivity regarding radiation irradiating from above, it is important to highlight the fact, that RaySafe i3 detectors are able to provide reliable dosimetric values. That applies to almost any positions in the area of radiation fields. Therefore, concerning monitoring issues, wearing RaySafe i3 detectors can be useful to all professional groups working in the Cath lab. Consequently, implementation of real-time dosimetry systems in Cath labs can provide accurate information regarding absorbed occupational doses.

For getting an insight, regarding the comparability between RaySafe i3 system and ionisation chambers (Capintec PM-500, PTW ionization chamber Type 32002), the output quantities of the ionisation chambers were unified to the physical quantity air kerma (Ka). The mean value (PDM_MEAN) of all RaySafe i3 dosimeters was used to calculate a conversion factor from air kerma to Hp(10). The obtained factor of $0.915\ \frac{\mu Sv}{\mu Gy}$ was exemplary for a conversion

coefficient in between the narrow (N) X-ray spectra 30 kV (N-30) and 40 kV (N-40) (Table 20).

The conversion coefficients from air kerma to the ICRU operational quantity Hp(10) with respect to radiation qualities N-15 to N-60 of the ISO narrow spectrum series are defined as follows (Hakanen *et al.*, 2007):

Table 20 : Conversion Coefficients from Ka to Hp(10) concerning Radiation Quantities N-15 to N-60

Radiation Quantities	**X-ray tube voltage** (kV)	**Mean Photon Energy** (keV)	**Conversion Coefficient from Ka to Hp(10)** ($Sv*Gy^{-1}$)
N-15	14.2	11.4	0.064
N-20	19.1	15.4	0.28
N-25	25.0	20.0	0.56
N-30	29.5	24.1	0.79
N-40	39.9	33.1	1.19
N-60	60.7	48.0	1.66

The initial X-ray tube voltages of the experimental setup ranged from 65.4 kV to 73.1 kV. Even if the radiation spectrum of scattering radiation is not comparable to narrow (N) spectrum series listed in Table 20, an approximation of the mean energy of scattered photons was calculated. According to the International Organisation for Standardization ISO 4037-1 (1996) standard [3] and another publication (Hakanen *et al.*, 2007) a conversion factor of 0.915 $\mu Sv*\mu Gy^{-1}$ was in line with radiation quantities between N-30 and N-40. This ended up in an estimated mean energy range of scattered photons between 24.1 keV and 33.1 keV. This estimation is in line with scientific evidence (Munjal *et al.*, 2006), stating mean scatter energies of about 40 keV referring to an initial X-ray tube peak voltage of 70 kV. This means that the mean energy of scattered photons of about 28 keV paired with the initial X-ray tube voltages in an area of 68 kV is plausible.
Consequently, the dosimetric output of RaySafe i3 was in line with theoretically expectable energy spectrum of scattered photons.

Figure 30 displays the ratio of RaySafe i3 and ionisation chambers (Capintec PM-500, PTW ionization chamber Type 32002) taking into account various combinations of dose quantities

(Q1, Q2, Q3) and distances (A1, A2, A3). Regarding the setup configuration, Q3A1 was accompanied with irregularities regarding the determined dose ratio ending up in a peak caused by increased quotient. A higher quotient can be caused be a decreased denominator (here: PDM – RaySafe i3). In consideration of determined dose rates
(Figure 32), the experimental setup Q3A1 caused dose rates maxima more than 1000 mSv/h. In view of dose rate uncertainties listed in Table 5, a deviation of dose values can be a consequence of too high dose rates. It can thus be concluded, that dose values detected by RaySafe i3 system tend to be under dimensioned in situations with high dose quantities paired with a short distance to the scattering body.

Focusing on the decrease of dose exposure as a function of distance, Figure 31 points out another important issue. According to the inverse square law, physical quantities decrease inversely with the square of distance from the initial source. Therefore, to double the distance should result in a reduction to one quarter of the initial dose value. All measurements performed with ionisation chambers resulted in a dose reduction to one third and less. Figure 54 depicts this difference between theory and practice.

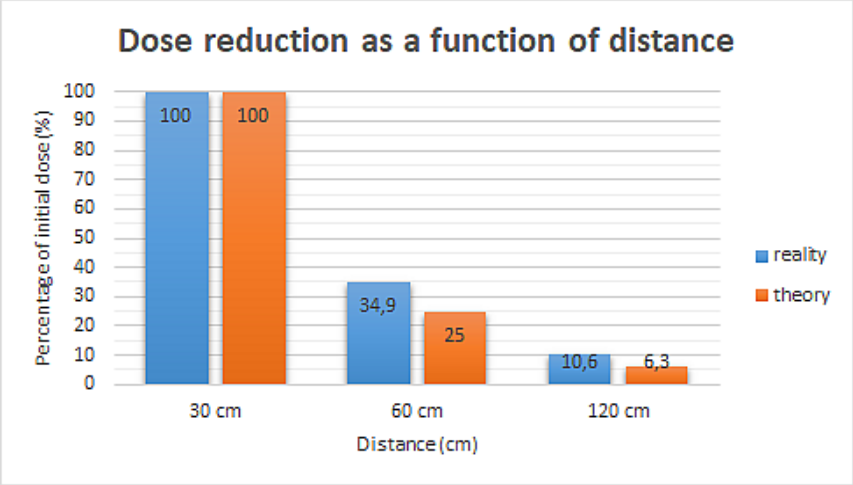

Figure 54: Dose reduction as a function of distance in theory and real life

This experience is consistent with (Haqqani *et al.*, 2013) stressing the fact that one further step away from the scattering body may not reduce the risk of radiation exposure as expected. The inverse-square law is based on an isotropic point source emitting mono- energetic photons in empty space. Of course, these conditions cannot be transferred to the environment of a Cath lab. Many employees working in radiation fields, rely on the protective extent of the inverse square law. Even if a larger distance to a radiating source results in a smaller

radiation exposure, educational contents regarding radiation protection courses need to be rethought. According to this educational issue concerning radiation protection, the project "EuroSafe-imaging", supported by 22 European countries, does have the mission to support and strengthen medial radiation protection and stresses the importance to distribute comprehensive knowledge over all involved professions (Imaging *et al.*, 2018). Exemplifying anaesthetic teams staying in varying distances to the patients, the application of additional protection devices like mobile radiation shield walls or additional under table shields may be recommended.

7.2 Determination of eye lens dose using correction factors

The idea of double dosimetry, implies the receipt of confident dose values resulting in a realistic estimation of the dose to the lens of eye. The fact, that in course of fluoroscopic guided interventions the latest annual dose limit of 20 mSv can be exceeded (Jacob *et al.*, 2013) an increased demand for the dosimetric determination of the lens exposure has occurred. Since direct eye dosimetry is not practicable in practice, dose ratios from the lens of eye to pre-defined reference points (thyroid, sternum) are to be established. To perform precise dosimetry on the spot, the usage of ionisation chambers is not suitable. Due to their favourable size, TLD chips are preferred for selective dosimetry. Under consideration of correction factors, real-time dosimetry devices placed beyond the lead apron (thyroid, chest) are thought to provide a prompt estimation for the eye lens dose. Therefore, correction factors determined by TLDs and RaySafe i3 are to be compared.

Regardless of the measuring points, Table 18 shows almost uniform dose ratio for both dosimetry devices. The ratio of 0.6 for eye lens/thyroid and 0.51 for eye lens/sternum corresponds to findings of previous publications. Carinou *et al.*, 2015 denotes a range of correction factors from 0.44 to 1.86, however, ratios of one and more can be explained by angiography systems with overcouch tubes. Martin and Magee, 2013, published in a review of studies of interventional procedures of different types, a median dose ratio of 0.6. And also, the dose ratio eye lens/chest of 0.51 is in line with the published range between 0.5 and 0.75. It can therefore be concluded, that dose ratios obtained by TLDs and RaySafe i3 system are consistent with existing scientific evidence. Based on the conditions of the experimental setup, the application of personal real-time dosimetry devices, such as RaySafe i3, can be

useable tools to estimate the dose exposure to the lens of eye. Consequently, RaySafe i3 fulfils the request of ICRP, Society of Interventional Radiology (SIR) and Cardiovascular and Interventional Society of Europe (CIRSE) for the application of second dosimeters worn above the lead apron.

With regards to a consistently occurring ratio of absolute dose values between TLDs and PDMs (Table 17) of about 1.3, these effects are in line with publications ((Boziari *et al.*, 2011), (Clairand *et al.*, 2009)) reporting about discrepancies of dosimetric performance between this two systems caused by under responding PDM-systems.

Another strategy to create reliable correction factors is based on a correlation between KAP and dose values considering radiation exposure to the lens of eye.

Figure 55 shows a regression analysis considering measurements obtained from RaySafe i3 detectors positioned at the nasal root of the dummy (Interventionist, Assistant) and KAP values read out from technical protocol of the angiography system. The coefficient of determination R^2=0.9926 confirms the linear regression.

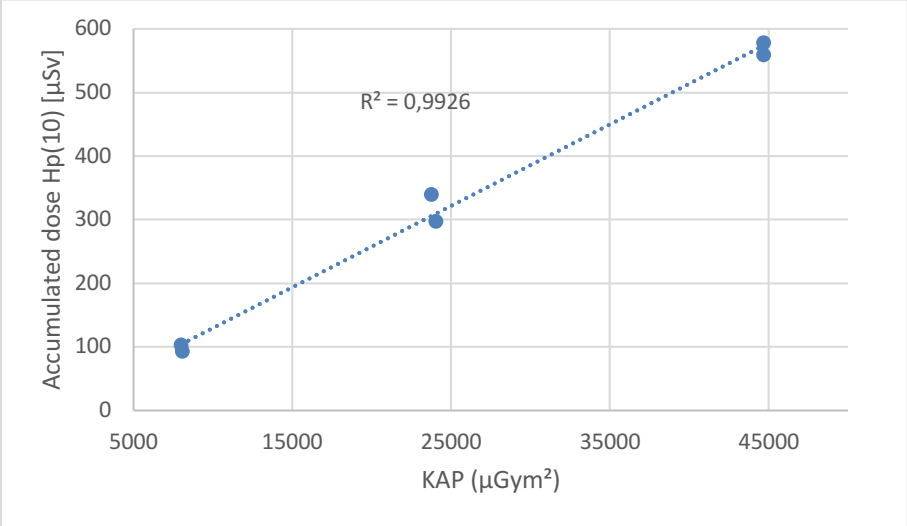

Figure 55: Regression analysis - Eye lens exposure and KAP

Next step was to determine conversion factors from KAP to the effective dose Hp(10) in consideration of altering setups (changing FOVs). Depending on changing test procedures obtained conversion factors were within 0.0114 and 0.0144 µSv/Gym² (Figure 56).

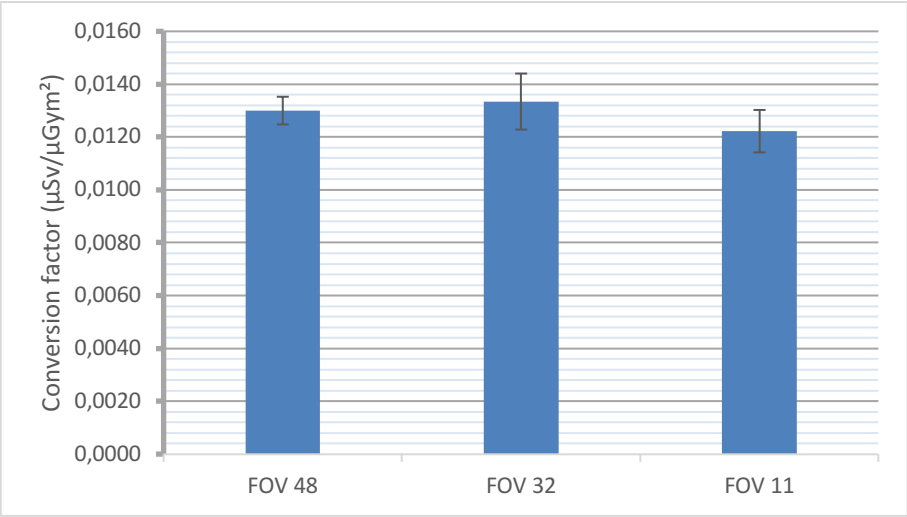

Figure 56: Correction factors KAPs-Hp(10) considering changing test procedures

To compare these conversion factors with evidence-based figures, the unit µSv/Gym² has to be converted into more common mSv/Gycm² by using the factor 10^{-1}. Finally, a mean generated conversion factor of 0.129 mSv/Gycm² was in line with published data (Irie, 2004) listing a mean conversion factors between dose-area product (DAP) und effective dose (E) for abdominal PTAs (percutaneous transluminal angioplasty) of 0.12 (0.10-0.15) mSv/Gycm² and regarding abdominal embolization a correction factor of 0.14 (0.11-0.16) mSv/Gycm².

7.3 Change of personnel dose exposure with respect to altering magnifications

The general principle of electronic magnification is the reduction of the X-ray field and display it over the full viewing area of the examination monitor. Consequently, the irradiated volume of the patient decreases with rising magnification level. In contrast to magnification, a collimated irradiated area results in a smaller X-ray field but no further advantages considering the visibility of small structures. To evaluate the change of dose exposure to medical staff by altering the level of magnification was the aim of chapter 6.5. The reduction of dose exposure for all working areas referring to each measuring point (nasal root, thyroid, sternum) was confirmed by RaySafe i3 detectors. Figure 39 displays a uniform significant ($p < 0.02$) dose reduction to all measuring points at all monitored places in the intervention

room in conjunction to applied magnification. Depending on the level of magnification, dose reductions up to 80% can be achieved (Figure 40). These results point to the likelihood, that the application of electronic magnification reduces radiation exposure at any places in the Cath lab and therefore results in a lower eye lens dose to the medical staff. In general, it can be noted, that magnification level (FOV-size) and occupational radiation exposure (detected by RaySafe i3 system) act indirectly proportional to each other (Figure 57).

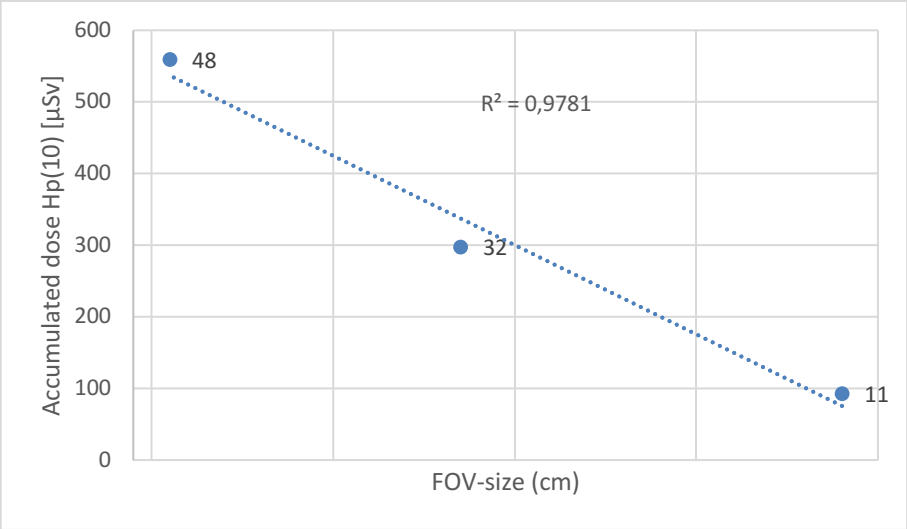

Figure 57: Correlation and regression analysis in the field of dose exposure and FOV-size

These findings are consistent with behaviour of kerma-air product (KAP) in connection with altering FOV-sizes. Referring to the direct ratio of KAP and to personnel dose exposure (Figure 55), the KAP and the occupational dose exposure decreased in a similar extend (80 %), by reducing the FOV-size from 48cm to 11 cm.

On the other hand, obtained air-kerma values increase with shrinking FOV-size (Figure 53). Depending on the magnification level, the cumulative air-kerma (CAK) raises up to 225 %. KAP is the product of the radiation dose in the centre of the X-ray beam at a certain plane and the area of this plane. Based on the inverse square law and the increase of area with the square of distance, KAP is independent from geometric alterations. To estimate risks for skin reactions KAP is an insufficient tool. On the other hand, KAP allows approximate assessments regarding stochastic effects or effective dose (Mohapatra *et al.*, 2013). Figure 52 shows, that increasing magnification causes a significant decrease of KAP. Therefore, the application of magnification during fluoroscopic guided interventions ends up in a decrease of occupational dose exposure but also reduced risks for stochastic effects to the patients. A

similar conclusion was reached by a previous study (Mohapatra *et al.*, 2013).

Nevertheless, this statement contradicts common previous recommendations regarding concepts focusing on radiation protection to the patient (Icrp, 2012). This rejective stance towards the use of magnification-mode is based on its adverse impact on the tissue reactions. An increased magnification level result in a higher CAK (Figure 53). Since direct measurements of patient doses are not performed routinely, CAK provides an indicator for the peak skin dose (PSK). PSK is a parameter for estimation of deterministic effects such as skin damages. Consequently, the aim is to lower CAK to reduce the risks of deterministic complications. Unfortunately, a larger FOV-size reduces CAK, but on the other hand increases the total amount of energy deposited in the patient (Mohapatra *et al.*, 2013). Furthermore, medical staff directly in close to the patient, receives higher scatter dose exposure. This insight is of practical value as the use of X-ray protective shields is cumbersomely. In such situations, to assure sufficient radiation protection to the staff, the enhanced application of magnification can be useful.

Apart from this, magnification mode is a helpful tool to improve the visibility of small structures such as vessels, microcatheters or microwires during complex fluoroscopic guided interventions (e.g. embolization of pelvic vessels). Not using magnification modes during fluoroscopic guided interventions may result in a potential higher number of intraprocedural complications and in a prolonged intervention and radiation time. Therefore, the use of magnification can increase patient's safety without additional risks of skin damage as long as threshold doses for deterministic effects are not exceeded (Gkanatsios *et al.*, 2001).

7.4 Performance of protective eyewear

To prevent an exceeding of the averaged equivalent dose limit to the lens of eyes of 20 mSv per year, the ICRP recommends (Icrp, 2012) the use of protective eyeglasses but also eye dose assessment. This chapter is about the determination of the dose to the lens of eye based on following parameters:

- Eye level
- Head alignment
- Scattering body
- Eyewear design

The first objective was to quantify the sole performance of protection glasses. Therefore, a setup was chosen to minimize the influence of glass sizes and individual frame designs on the dose exposure to the eye lens. Thus, the scattering body (water phantom) and phantom head, equipped with different types of protection glasses (no protection, Type 115, Type 126) were positioned at the same level of 100 cm.

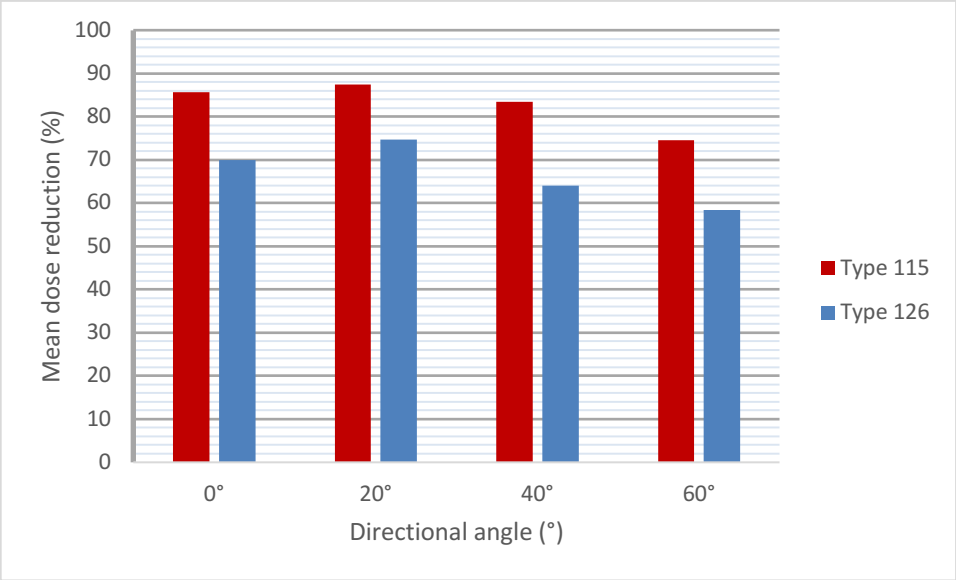

Figure 58: Comparison of percentage dose reduction at 100 cm height using a water phantom

As shown in Figure 41, both glasses, Type 115 and Type 126 performed well over the entire range of head alignments. With regard to Figure 41 and Figure 58, Type 126 exceeded Type 115 concerning all directional angles. Considering absolute dose values obtained in course of the trial, the ratios of residual eye dose values using Type 115 (mean dose reduction -83/%) and Type 126 (mean dose reduction -67%) lay in a range between 1.6 and 2.2 (Table 21).

Table 21: Accumulated lens dose values considering changing head alignments and protection devices

	Orientation of the head			
	0°	**20°**	**40°**	**60°**
No protection (µSv)	683.4	641.8	604.6	564.8
Type 115 (µSv)	98.4	80.7	100.0	143.1
Type 126 (µSv)	205.2	160.6	217.0	234.3
Type 126/ Type 115	2.1	2.0	2.2	1.6

In order to draw a comparison with evidence-based data, collected data expressed at percentages of dose reduction are converted in dose reduction factors. Dose reduction factor (DRF) is a common value describing the efficacy of protection devices being deployed in numerous publications. DRF is equal to the ratio of dose of unprotected eyes, divided by dose exposure when lead glasses are worn. Regarding the range of DRFs, Type 115 attained factors from 3.9 to 7.9 and Type 126 from 2.4 up to 4.0. To sum it up, both types of glasses confirmed high DRF values of 6.2 and 3.1 averaged over all head positions (Figure 59).

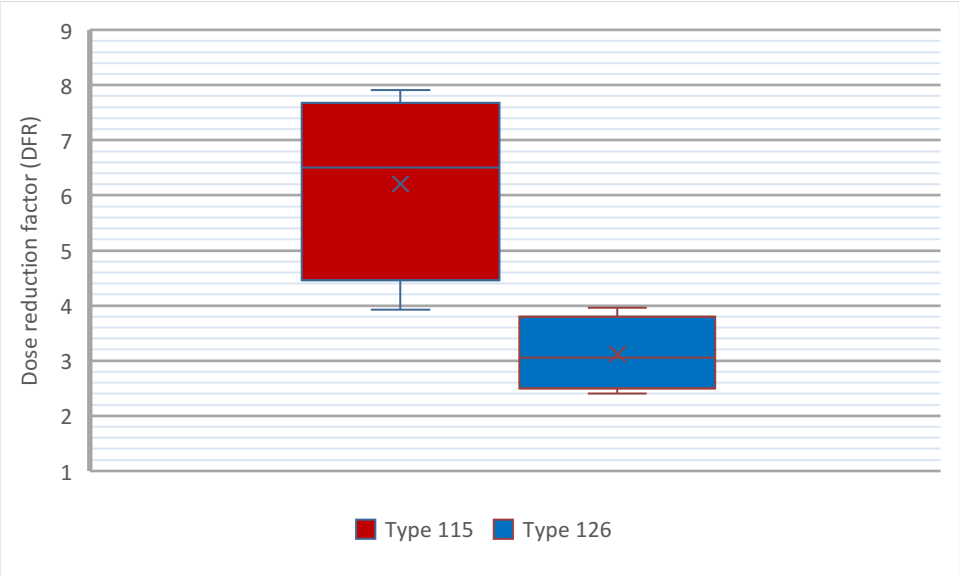

Figure 59: Comparison of dose reduction factors at 100 cm height using a water phantom

Several studies for example Magee *et al.*, 2014, confirm this range of DRFs (5.2 – 7.6) in case of frontal impacting X-rays in the same horizontal plane.

Nevertheless, varying radiation protective effects resulted in a difference of residual dose values in excess of more than 100 %. This investigation revealed a significant difference between both types of leaded eyeglasses allowing the conclusion that, a higher lead equivalent (0.5 mm PB vs 0.75 mm Pb) might be associated to a higher level of lens protection. However, glasses equipped with 0.5 mm lead equivalence lenses can attain sufficient dose reduction to the lens of eyes (Magee *et al.*, 2014). On the other hand , a linear corelation between lead equivalent and protective performance cannot generally be assumed, since previous studies showed an decreased impact of lead equivalence on the eye lens dose in course of different experimental setups (Koukorava *et al.*, 2014). Consequently, despite from lead equivalent also the frame design plays a key role in the radiation protection. Therefore, glasses equipped with 0.5 mm lead equivalence lenses can attain sufficient dose reduction to the lens of eyes (Magee *et al.*, 2014). Focusing on the experimental setup, it has

to be mentioned that the settings of this test did not reflect a realistic situation in the Cath lab. For this reason, the eye levels were shifted to a height of 176 cm and 157 cm. The position of the scattering body was maintained. Therefore, difference in heights between scattering body and the lens of eye were 76 cm and 57 cm.

In contrast to the previous setting, an eye level of 176 cm effected an altered efficiency regarding the reduction of the dose of eye. Figure 43 and Figure 49 outline data indicating a larger dependency on the directional angles on the one hand, and a smaller protection efficiency on the other hand. These more heterogeneous outcome was confirmed by a larger difference between maximum and minimum values and therefore a larger range of values (Table 22) compared to the initial experimental setup.

Table 22: Statistical comparisons between eye level 176 cm and eye level 100 cm

	Eye level 176 cm		Eye level 100 cm	
	Type 115	**Type 126**	**Type 115**	**Type 126**
Mean dose reduction (%)	27.8	17.9	82.8	66.8
Maximum (%)	66.6	43.2	88.0	79.8
Minimum (%)	3.6	0.2	71.7	55.5
Range (%)	63.0	43.0	16.3	24.3

As a result, the mean DRF decreased to 1.2 (Type 126) and 1.4 (Type 115). In addition, also the range of DRFs dropped. Type 115 reached dose reduction factors between 1.9 and 1.2, Type 126 from to 1.1 to 1.4 (Figure 60). The ratio of residual dose values referring to different types of glasses in various head positions reached from 1.0 to 1.4. Thus, the gap of protective efficiency between Type 115 to Type 126 shrinked. Even though Type 115 seemed to achieve lower eye doses, no significant advantage could be determined (Figure 60).

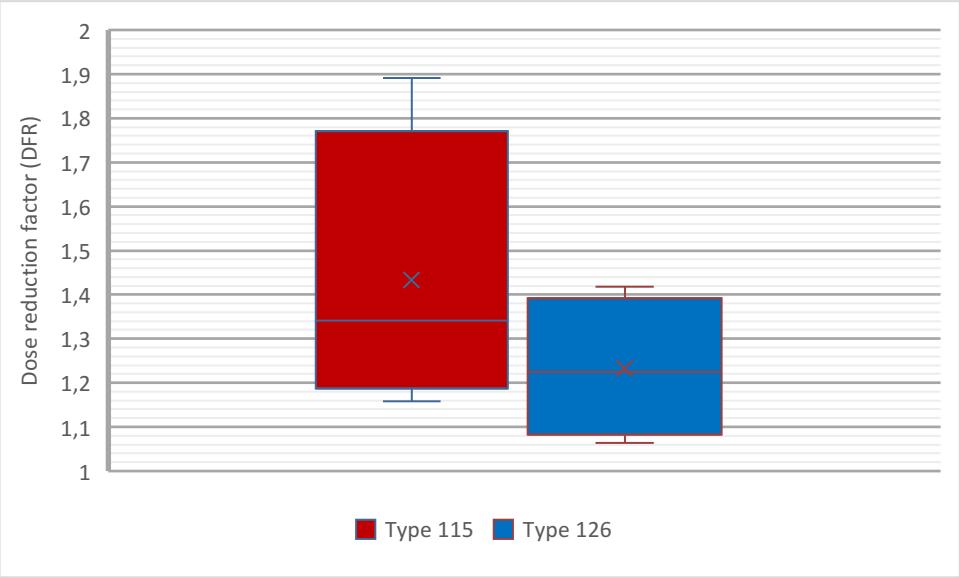

Figure 60: Comparison of dose reduction factors at 176 cm height using a water phantom

Taking into account physically smaller staff members, the level of eyes was reduced from 176 cm to 157 cm.

The reduction of about 19 cm of height ended in a rather unexpected result. In comparison with the previous experiment, the protective effects of both glasses were clearly disparate (Figure 61). In contrast to a mean dose reduction of 65.1 % achieved by Type 115, Type 126 only gained a mean percentage reduction of 16.8 %. In direct comparison between both types of protection glasses, the mean ratio of residual dose exposure to the lens of eyes was 2.6 (1.7 to 3.4).

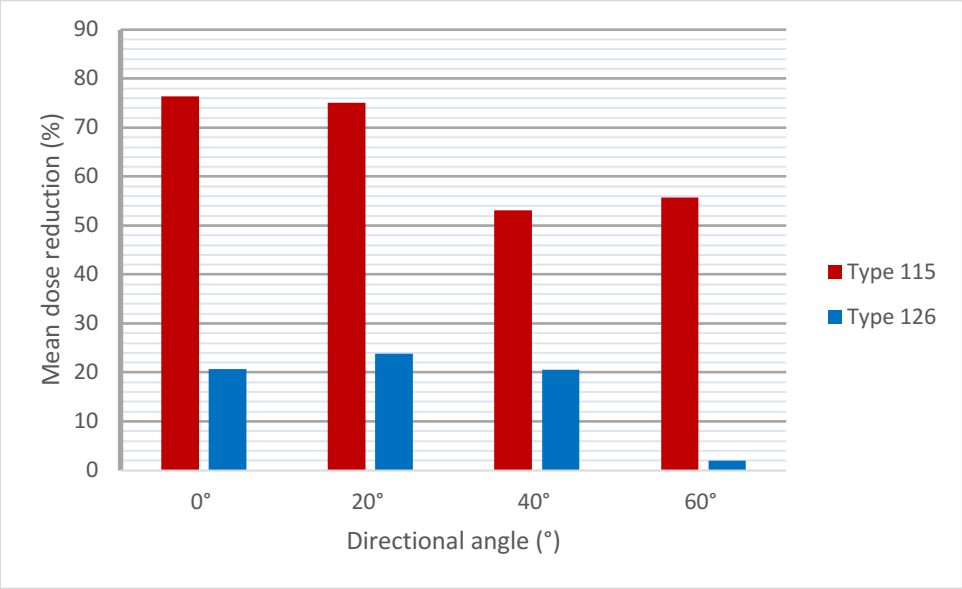

Figure 61: Comparison of percentage dose reduction at 157 cm height using a water phantom

And also, the determined DRFs of both glasses deviated significantly (Figure 62).

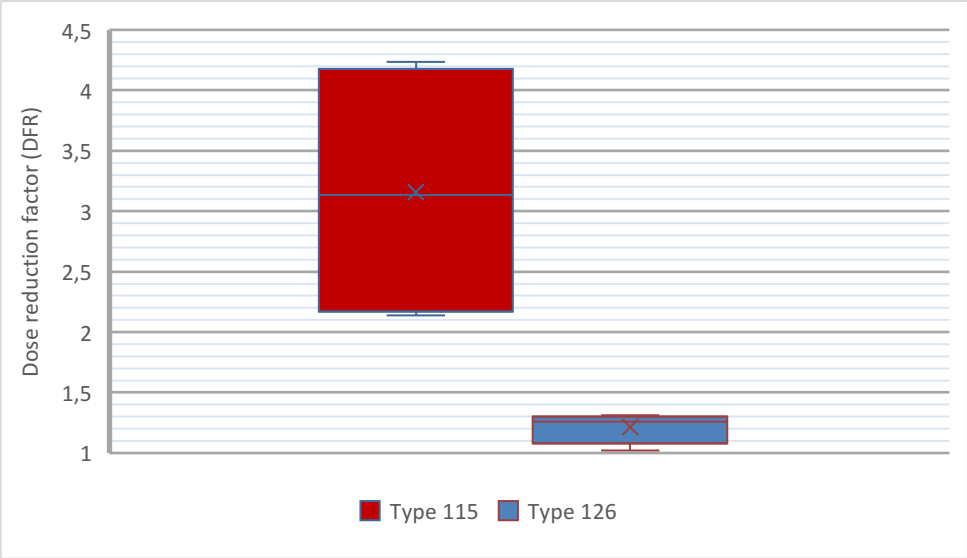

Figure 62: Comparison of dose reduction factors at 157 cm height using a water phantom

Type 115 provided a wide range of DRF values from 2.1 to 4.2. On the other side, Type 126 presented a poor DRFs between 1.0 and 1.3.

These tests reveal an almost heterogeneous efficacy regarding the protective performance for both glasses.

Generally speaking, Type 115 was superior in almost every level. However, because of the wide range of dose reduction factors, the design of these glasses did not guarantee a constant protection over all tested head positions. With respect to the eye level, clear differences in dose reduction factors were determined (Figure 63).

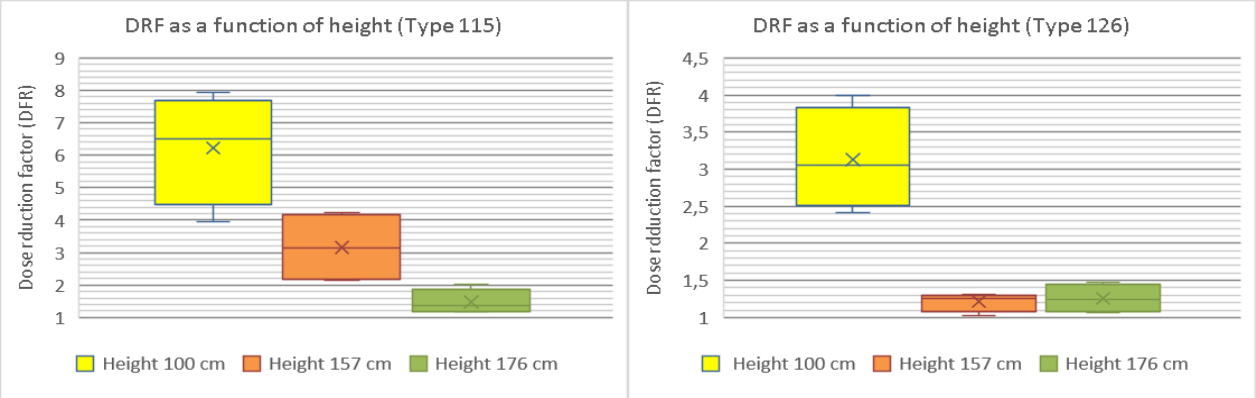

Figure 63: Dose reduction factor as a function of height referring to Type 115 and Type 126

Mean DRF of 3.2 at a height of 157 cm stood in contrast to a mean DRF of 1.4 at a height of 176 cm. Especially, a combination of a high eye level (176 cm) and head orientation turned away from the detector (60 °) resulted in its worst outcome (dose reduction factor: 1.2).

Regarding leaded eyeglasses Type 126, its top protective performance appeared in connection with the lowest eye level (100 cm) resulting in a mean dose reduction of about 67% and an averaged dose reduction factor of 3.1. With increasing eye levels (176 cm and 157 cm), the dose reduction factors dropped in a field of 1.2. in conjunction with a small deviation. It can therefore be concluded that at a specific eye level, the viewing direction did not a have great impact on the dose exposure to the lens of eye.

Despite the larger spectrum of dose reduction factors gained in these tests, the ranges and dimensions of values were in line with previous findings. A literature review focusing on parameters dealing with eye lens protection published a spectrum of dose reduction factors from 1.2 up to 10.2 determined in course of various test setups (Seals *et al.*, 2016).

In contrast to the water phantom, the irradiation of the Alderson phantom resulted in an approximately one and a half times higher dose exposure, regardless the eye level and the

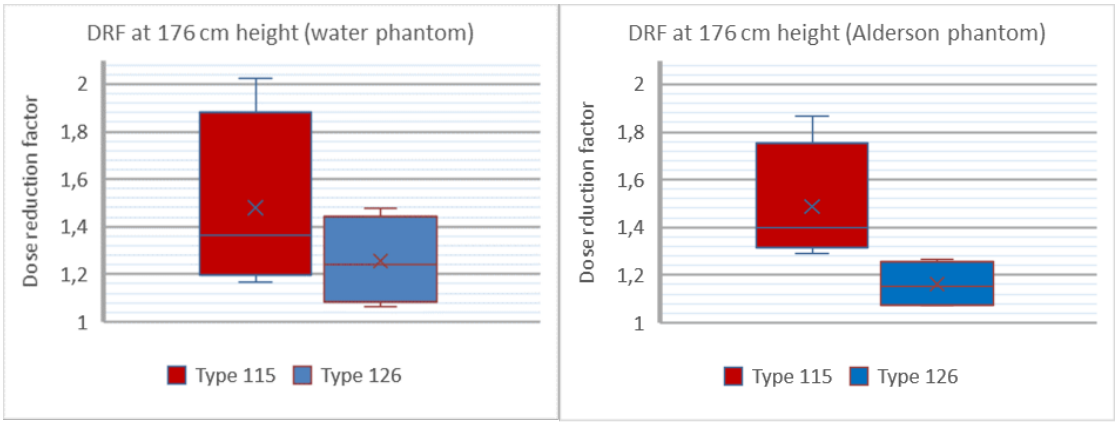

Figure 64: Comparison of dose reduction factors with regard to the scattering bodies

type of protection glasses. This confirms the impact of the patient's shape on the occupational dose exposure.

However, focusing on the DRFs, Figure 64 demonstrates an almost neglectable difference concerning an altering protective outcome by varying scattering bodies. This implies that an increase of tube voltage from 63 kV to 70 kV does not affect the dose reduction factor significantly. This effect is confirmed by previous findings in the literature. Monte Carlo simulations have shown, that altering beam qualities do not have a great impact on the

efficiency of lead glasses. Within the range from 70 kV to 100 kV, the reduction of calculated radiation exposure to the lens of eye is less than 5% (Koukorava *et al.*, 2014).

7.5 Limitations of the study

Comparing the results of the protective effect of lead glasses of this thesis to other studies, it has to be considered that this study exclusively focused on the left lens of eye. Since tests have to be repeated several times, a limited number of TLD-chips indicated to focus on the left eye explicitly. A number of studies and also this thesis have shown that in general the right eye is exposed a lower radiation dose than the left one (Koukorava *et al.*, 2014)(Vanhavere *et al.*, 2011b). Therefore, the radiation exposure to the left eye was focus of this work. This deviation to other studies may have led to different measuring results, since the protective effect of lead glasses is not averaged over both sides. This fact may end up at an advantage, since the dose to the lens of eye is more closely connected with the protective quality of the lead glasses. In contrast to the right eye, additional influencing factors like distance or anatomic structures presenting additional obstacles for scattering radiation do have a lower impact on dose exposure at the left eye by changing the alignment of the head.

Another limitation for the quantification of the protective effect of lead glasses involves the individuality of head shapes. Although the Rando Alderson Phantom is an accepted and widely used scattering body, its head only represents one certain shape of head. Factors like the air gap between glasses and eyes and the individual fit of different designed glasses do have an impact on the amount of scattering radiation reaching the eyes (Koukorava *et al.*, 2014). Therefore, this study can only reflect results based on these specific experimental setups.

Finally, in contrast to other studies, TLD chips used in this study were calibrated in the area of scattering radiation and not to a predefined X-ray beam (Magee *et al.*, 2014). Therefore, the outcome of these test series almost based on realistic conditions. On the other hand, this fact can end up in potential different results regarding quantitative and qualitative issues referring to dosimetric measurements.

8 Conclusion

The advantage of real-time occupational personnel dosimeters for assessment of radiation exposure to the lens of eye in the course of fluoroscopic guided interventions has already been studied (Omar *et al.*, 2015). With regard to the real-time dosimetry system RaySafe i3, the obtained data of this study is in line with these results with regard to the reliability in detecting occupational dose exposure. Therefore, the application of these new detectors can be a useful addition to other established devices.

We compared the RaySafe i3 system with different dosimetric devices issuing measuring values stated in the unity of µGy. The range of gained conversion factors allowing the conversion from air kerma (µGy) to the operational quantity Hp(10) varied from 0.68 to 0.92. Referring on (Hakanen *et al.*, 2007), this range of monoenergetic conversion coefficients from air kerma to the quantity Hp(10) were representing photon energies between 30 and 40 kV (Table 20). These insights may give a rough estimation of averaged photon energies arising in the area of scattered photons and the requirements for protection devices during fluoroscopic guided interventions.

In 2004, Bolognese-Milsztajn et al. tested 26 almost commercially available active dosimeters. Among relevant issues following key questions were treated:

- Are active personal dosimeters (APD) as reliable, or better than passive dosimeters?
- Are they suitable for all practices?

Regarding the energy and angular response characteristics, APDs were in most cases as good as passive dosimeters (TLD). Regarding the suitability of APDs, their general response in the range of diagnostic X-ray energies was comparable to standard passive detectors (Bolognese-Milsztajn *et al.*, 2004). This article recommends, based on the study results, the additional use of personal real-time dose monitoring systems. In the last one and a half decades real-time dosimetry devices have received consistent improvement concerning their dosimetric performance and practicability (e.g. battery life, output software). This fact is reflected in increased performance of RaySafe i3 compared to the previous model RaySafe i2. Especially, an improved angular response characteristic allows a more serious individual operational dosimetry in daily clinical practice. As a result, countries like the United Kingdom and Switzerland accept the use of active personal dosimeters, for the legal assessment of dose (Ginzburg, 2017).

For estimation of eye lens dose the application of double dosimetry has been recommended (Ciraj-Bjelac and Rehani, 2014), (Icrp, 2012). Obtained dose correction factors allow an assessment of the dose exposure to the lens of eyes without placing disruptive dosimeters in the visual view. Another approach obtaining correction factors for radiation exposure to the eye is based on the correlation of kerma-area product and the occupational exposure to the lens of eye. Under local given conditions, data, received from angiography system and RaySafe i3 detectors resulted in comparable correction factors. Although obtained results are not generally applicable, it can thus be concluded that RaySafe i3 system ensures the supply of reliable dose values provided that high dose rates in the radiation field do not cause underestimated dose values given from this system. However, these correction factors should be interpreted and applied with caution. Due to the usage of additional protective eyewear, eye lens monitoring may become more complex. This study demonstrates a considerable number of variables (eyeglass lenses, glasses frame, eye level and viewing direction) affecting the dose exposure to the lens of eye. Consequently, correction factors based on non-protected eyes become useless if protective glasses are worn. In consideration of the individual protective performance of different types of radiation eyewear, the application of general valid correction factors seems to be difficult. Alternatively, dosimeters integrated in radiation protection glasses are subject of ongoing research (Hoedlmoser *et al.*, 2019). However, the educational value for double dosimetry, especially for high-dose interventions remains evident (Racadio *et al.*, 2014)(James *et al.*, 2015).

Due to individual head shapes, protective performance of radiation protection glasses can vary. Therefore, a more flexible eyewear design would be desirable. Especially, a more customizable frame focusing on lateral protection could result in a lower dose exposure to the lens of eye.

Another aspect that is worth paying attention is the use of magnification during fluoroscopic guided interventions. Besides an improved visualisation of small details such as vessels, microcatheters or microwires, the dose exposure to the entire staff working in the Cath lab decreased significantly by a similar amount. Especially, situations impeding the usage of ceiling suspended screens, the conscious application of higher magnification levels can compensate missing protection devices in a high degree. Particularly, during pelvic vascular interventions, where the distance between the irradiated volume and the interventionist is short, a dose reduction of approximate 80 % can be achieved. This fact seems to be adoptable to all professions acting in the range of radiation in the Cath lab.

9 List of references

Agency, E. (2015) ‘Operational quantities and new approach by ICRU’, *Annals of the ICRP*, 45, pp. 178–187. doi: 10.1177/0146645315624341.

Alderson, P. *et al.* (2015) ‘Report on the Hormesis / Linear No-Threshold Petitions Subcommittee Members’, pp. 10–13.

Bahruddin, N. A. *et al.* (2016) ‘Radiation dose to physicians’ eye lens during interventional radiology’, *Journal of Physics: Conference Series*, 694(1). doi: 10.1088/1742-6596/694/1/012035.

Baxter, R. *et al.* (2008) ‘[IRPA GUIDANCE ON IMPLEMENTATION OF EYE DOSE MONITORING AND EYE PROTECTION OF WORKERS]’, *Animal Genetics*, 39(5), pp. 561–563.

Bolognese-Milsztajn, T. *et al.* (2004) ‘Active personal dosemeters for individual monitoring and other new developments’, *Radiation Protection Dosimetry*, 112(1 SPEC. ISS.), pp. 141–168. doi: 10.1093/rpd/nch286.

Boziari, A. *et al.* (2011) ‘The use of active personal dosemeters as a personal monitoring device: Comparison with TL dosimetry’, *Radiation Protection Dosimetry*, 144(1–4), pp. 173–176. doi: 10.1093/rpd/ncq545.

Brant-Zawadzki, M. *et al.* (1983) ‘Digital subtraction cerebral angiography by intraarterial injection: Comparison with conventional angiography’, *American Journal of Roentgenology*, 140(2), pp. 347–353. doi: 10.2214/ajr.140.2.347.

Brenner, D. J. (2011) ‘Icrp 2011’, *Annals of the ICRP*, 41(3–4), pp. 124–128. doi: 10.1016/j.icrp.2012.07.001.

Busch, U. (German R. M. R.-L. G. (2013) ‘The progress in Radiology in 1896’, *The Story of Radiology - Vol .2*, 2, pp. 7–23. Available at: http://www.bshr.org.uk/The_Story_of_Radiology_Vol1.pdf.

Carinou, E. *et al.* (2015) ‘Eye lens monitoring for interventional radiology personnel: Dosemeters, calibration and practical aspects of Hp(3) monitoring. A 2015 review’, *Journal of Radiological Protection*. IOP Publishing, 35(3), pp. R17–R34. doi:

10.1088/0952-4746/35/3/R17.

Chodick, G. *et al.* (2008a) 'Risk of cataract after exposure to low doses of ionizing radiation: A 20-year prospective cohort study among US radiologic technologists', *American Journal of Epidemiology*, 168(6), pp. 620–631. doi: 10.1093/aje/kwn171.

Chodick, G. *et al.* (2008b) 'Risk of cataract after exposure to low doses of ionizing radiation: A 20-year prospective cohort study among US radiologic technologists', *American Journal of Epidemiology*, 168(6), pp. 620–631. doi: 10.1093/aje/kwn171.

Ciraj-Bjelac, O. and Rehani, M. M. (2014) 'Eye dosimetry in interventional radiology and cardiology: Current challenges and practical considerations', *Radiation Protection Dosimetry*, 162(3), pp. 329–337. doi: 10.1093/rpd/nct291.

Clairand, I. *et al.* (2009) 'Use of active personal dosemeters in interventional radiology: A systematic study in laboratory conditions', *IFMBE Proceedings*, 25(3), pp. 132–135. doi: 10.1007/978-3-642-03902-7-38.

Clarke, R. H. and Valentin, J. (2009) 'The History of ICRP and the Evolution of its Policies', *Annals of the ICRP*, 39(1), pp. 75–110. doi: 10.1016/j.icrp.2009.07.009.

Commission, G., Protection, R. and Reasoning, S. (2009) 'Radiation-Induced Cataracts Recommendation by the German Commission on Radiological Protection with Scientific Reasoning'. Available at: http://www.ssk.de.

Consultants, A. B. (1989) 'Historical Development of Radiation Practices in Radiology', *RadioGraphics*, pp. 267–275. doi: 10.1148/radiographics.9.6.2685944.

Dendy, P. P., Heaton, B. and Cameron, J. (2001) *Physics for Diagnostic Radiology*. 2., *Medical Physics*. 2. New York: Taylor & Francis. doi: 10.1118/1.1350686.

Dietze, G. *et al.* (2005) 'Draft for discussion: Basis for dosimetric quantities used in radiological protection', *International commission on radiological protection committee*, (Task Group of ICRP Committee 2).

Doss, M. (2013) 'Linear no-threshold model vs. radiation hormesis', *Dose-Response*, 11(4), pp. 480–497. doi: 10.2203/dose-response.13-005.Doss.

Ginzburg, D. (2017) 'Ionisation chamber for measurement of pulsed photon radiation fields', *Radiation Protection Dosimetry*, 174(3), pp. 297–301. doi: 10.1093/rpd/ncw145.

Gkanatsios, N. A. *et al.* (2001) 'How does magnification affect image quality and patient dose in digital subtraction angiography ?', *Medical Imaging 2001: Physics of Medical Imaging*, 4320, pp. 326–330. doi: 10.1117/12.430927.

Gupta, V., Rajagopala, M. and Ravishankar, B. (2014) 'Etiopathogenesis of cataract: An appraisal', *Indian Journal of Ophthalmology*, 62(2), pp. 103–110. doi: 10.4103/0301-4738.121141.

Hakanen, A. *et al.* (2007) 'Determination of conversion factors from air kerma to operational dose equivalent quantities for low-energy X-ray spectra', *Radiation Protection Dosimetry*, 125(1–4), pp. 198–204. doi: 10.1093/rpd/ncl386.

Hamada, N. and Fujimichi, Y. (2014) 'Classification of radiation effects for dose limitation purposes: History, current situation and future prospects', *Journal of Radiation Research*, 55(4), pp. 629–640. doi: 10.1093/jrr/rru019.

Haqqani, O. P. *et al.* (2013) 'De fi ning the radiation " scatter cloud " in the interventional suite', *Journal of Vascular Surgery*. Elsevier, 58(5), pp. 1339–1345. doi: 10.1016/j.jvs.2013.01.025.

Hart, D. *et al.* (2010) *HPA-CRCE-012 Frequency and collective dose for medical and dental X-ray examinations in the UK, 2008*, *Health Protection Agency HPA-CRCE-012*. Available at: http://scholar.google.com/scholar?hl=en&btnG=Search&q=intitle:Frequency+and+Collective+Dose+for+Medical+and+Dental+X-ray+Examinations+in+the+UK+,+2008#0.

Hassan, B. (2018) *Endovascular aortic aneurysm repair : Aspects of follow-up and complications*.

Hefner, A. (1995) 'Hundred Years of Radiology', *Portorož*, (January), pp. 3–7. Available at: www.iaea.org/inis/collection/NCLCollectionStore/_Public/37/004/37004295.pdf.

Hoedlmoser, H. *et al.* (2019) 'New eye lens dosemeters for integration in radiation protection glasses', *Radiation Measurements*. Elsevier Ltd, 125(May), pp. 106–115. doi: 10.1016/j.radmeas.2019.05.002.

Horton, J. L. *et al.* (2012) 'Chapter 2 : Dosimetric Principles , Quantities and Units', pp. 45–70.

IAEA (International Atomic Energy Agency) (2013) 'TECDOC No. 1731 Implications for Occupational Radiation Protection of the New Dose Limit for the Lens of the Eye', (1731), pp. 2016–2021.

Icrp (2012) 'Annals of the ICRP 60', *Compendium of Dose Coefficients based on ICRP Publication 60*, (X), p. 130. doi: 10.1016/j.icrp.2006.06.001.

Imaging, E. *et al.* (2018) 'Education and training in medical radiation protection in Côte d ' Ivoire : where are we Background / introduction', pp. 1–7.

Irie, T. (2004) 'Realtime Digital Magnification of the Fluoroscopic and Digital Subtraction Angiography Images: Randomized Prospective Study to Show Dose Reduction during Segmental Chemoembolization for Hepatocellular Carcinoma', *Journal of Vascular and Interventional Radiology*, 15(2 I), pp. 165–168. doi: 10.1097/01.RVI.0000106392.63463.97.

Jacob, S. *et al.* (2013) 'Eye lens radiation exposure to interventional cardiologists: A retrospective assessment of cumulative doses', *Radiation Protection Dosimetry*, 153(3), pp. 282–293. doi: 10.1093/rpd/ncs116.

James, R. F. *et al.* (2015) 'Analysis of occupational radiation exposure during cerebral angiography utilizing a new real time radiation dose monitoring system', *Journal of NeuroInterventional Surgery*, 7(7), pp. 503–508. doi: 10.1136/neurintsurg-2014-011215.

Kishore, L. T. and Gupta, P. C. (2013) 'Vascular imaging:Past, present & future', *Journal International Medical Sciences Academy*, 26(1), pp. 65–68.

Koukorava, C. *et al.* (2014) 'Efficiency of radiation protection equipment in interventional radiology: A systematic Monte Carlo study of eye lens and whole body doses', *Journal of Radiological Protection*, 34(3), pp. 509–528. doi: 10.1088/0952-4746/34/3/509.

Krieger, H. (2010) *Grundlagen der Strahlungsphysik und des Strahlenschutzes*. 4., *Grundlagen der Strahlungsphysik und des Strahlenschutzes*. 4. Ingolstadt: Springer Spektrum. doi: 10.1007/978-3-8348-9348-2.

Krieger, H. (2013) *Strahlungsmessung und Dosimetrie*. 2. Wiesbaden: Springer Spektrum.

Magee, J. S. *et al.* (2014) 'Derivation and application of dose reduction factors for protective eyewear worn in interventional radiology and cardiology', *Journal of*

Radiological Protection, 34(4). doi: 10.1088/0952-4746/34/4/811.

Martin, C. J. and Magee, J. S. (2013) 'Assessment of eye and body dose for interventional radiologists, cardiologists, and other interventional staff', *Journal of Radiological Protection*, 33(2), pp. 445–460. doi: 10.1088/0952-4746/33/2/445.

Miller, D. L. *et al.* (2010) 'Occupational radiation protection in interventional radiology: A joint guideline of the cardiovascular and interventional radiology society of Europe and the society of interventional radiology', *Journal of Vascular and Interventional Radiology*. Elsevier Inc., 21(5), pp. 607–615. doi: 10.1016/j.jvir.2010.01.007.

Mohapatra, A. *et al.* (2013) 'Radiation exposure to operating room personnel and patients during endovascular procedures', *Journal of Vascular Surgery*. Elsevier Inc., 58(3), pp. 702–709. doi: 10.1016/j.jvs.2013.02.032.

Munjal, R. *et al.* (2006) 'Measurement of scatter radiation spectrum from radiographic units', *Journal of Medical Physics*, 31(2), p. 67. Available at: http://www.jmp.org.in/text.asp?2006/31/2/67/26690.

Omar, A. *et al.* (2015) 'On the feasibility of utilizing active personal dosimeters worn on the chest to estimate occupational eye lens dose in x-ray angiography', *Journal of Radiological Protection*, 35(2). doi: 10.1088/0952-4746/35/2/271.

Omar, A. *et al.* (2017) 'Assessment of the occupational eye lens dose for clinical staff in interventional radiology, cardiology and neuroradiology', *Journal of Radiological Protection*, 37(1), pp. 145–159. doi: 10.1088/1361-6498/aa559c.

Pavlovic, M. (2012) *Script MedTech course: Radiation and Nuclear Physics*.

Protection, I. C. on R. (1987) *Annals of the ICRP.* Available at: http://scholar.google.com/scholar?hl=en&btnG=Search&q=intitle:Annals+of+the+ICRP#5 .

Racadio, John *et al.* (2014) 'Effect of real-time radiation dose feedback on pediatric interventional radiology staff radiation exposure', *Journal of Vascular and Interventional Radiology*. doi: 10.1016/j.jvir.2013.08.015.

Reaktorsicherheit, B. (2014) 'Bekanntmachung Bundesministerium Bekanntmachung', (September), pp. 1–13.

Reich, H. (1990) *Dosimetrie ionisierender Strahlung*. 1. Stuttgart: Teubner Verlag.

Rizzi, M., D'Aloia, M. and Castagnolo, B. (2010) 'Semiconductor Detectors and Principles of Radiation-matter Interaction', *Journal of Applied Sciences*, 10(23), pp. 3141–3155.

Sandblom, V. *et al.* (2013) 'Evaluation of the impact of a system for real-time visualisation of occupational radiation dose rate during fluoroscopically guided procedures.', *Journal of radiological protection : official journal of the Society for Radiological Protection*, 33(3), pp. 693–702. doi: 10.1088/0952-4746/33/3/693.

Scannavino, F. A. and Cruvinel, P. E. (2012) 'A graphical tool for an analytical approach of scattering photons by the Compton effect', *Nuclear Instruments and Methods in Physics Research, Section A: Accelerators, Spectrometers, Detectors and Associated Equipment*. Elsevier, 674, pp. 28–38. doi: 10.1016/j.nima.2011.12.120.

Seals, K. F. *et al.* (2016) 'Radiation-Induced Cataractogenesis: A Critical Literature Review for the Interventional Radiologist', *CardioVascular and Interventional Radiology*, 39(2), pp. 151–160. doi: 10.1007/s00270-015-1207-z.

Del Sol Fernández, S. *et al.* (2016) 'Thermoluminescent characteristics of LiF: MG, Cu, P and CaSO4: Dy for low dose measurement', *Applied Radiation and Isotopes*, 111, pp. 50–55. doi: 10.1016/j.apradiso.2016.02.011.

Stadtmann, H. (2001) 'Dosemeter Calibration', *Radiation Protection Dosimetry*, 96, pp. 21–26.

Stecker, M. S. *et al.* (2009) 'Guidelines for Patient Radiation Dose Management', *Journal of Vascular and Interventional Radiology*. Elsevier Inc., 20(7 SUPPL.), pp. S263–S273. doi: 10.1016/j.jvir.2009.04.037.

Strzelczyk, J. (1998) *RADIOGENIC HEALTH EFFECTS: COMMUNICATING RISKS TO THE GENERAL PUBLIC Jadwiga (Jodi) Strzelczyk Radiological Sciences Division, Department of Radiology, School of Medicine University of Colorado HSC, Denver, CO. 80262 U.S.A.* Available at: https://www.google.com/url?sa=t&rct=j&q=&esrc=s&source=web&cd=1&ved=2ahUKEwi748v03MzeAhVECuwKHe13AjMQFjAAegQICBAC&url=https%3A%2F%2Fwww.ipen.br%2Fbiblioteca%2Fcd%2Finac%2F1999%2FPDF%2FCG09AX.PDF&usg=AOvVaw0SHTX5ym0l5isNwvUXJxko.

Vanhavere, F. *et al.* (2011a) ‘Measurements of eye lens doses in interventional radiology and cardiology: Final results of the ORAMED project’, *Radiation Measurements*. Elsevier Ltd, 46(11), pp. 1243–1247. doi: 10.1016/j.radmeas.2011.08.013.

Vanhavere, F. *et al.* (2011b) ‘Measurements of eye lens doses in interventional radiology and cardiology: Final results of the ORAMED project’, *Radiation Measurements*. Elsevier Ltd, 46(11), pp. 1243–1247. doi: 10.1016/j.radmeas.2011.08.013.

Vujošević, B. and Bokorov, B. (2010) ‘Radiotherapy: Past and present’, *Archive of Oncology*, 18(4), pp. 140–142. doi: 10.2298/AOO1004140V.

W.J. Meredith, J. B. M. (1968) *Fundamental Physics of Radilology*. 2. Bristol: John Wright & Sons Ltd.

Wyckoff, H. O. (2013) *International Commission on Radiation Units and Measurements (Icru)*, *American Journal of Roentgenology*. doi: 10.2214/ajr.120.3.708.

10 Appendix

10.1 Appendix A

Quantified dose values with respect to altering X-ray quantities and changing distances to the scattering body:

Dose Quantity -Distance	PM_500 (µSv)	IC 32002 (µGy)	PDM_GREY (µSv)	PDM_BLUE (µSv)	PDM_RED (µSv)
Q1A1	174,1	117,7	145,10	141,70	144,70
	173,3	117,4	143,10	150,20	151,20
	174,1	117,7	138,90	150,90	140,00
Q2A1	361,6	243,9	205,70	230,00	235,10
	374,2	251,8	218,70	225,72	235,23
	374,8	252,5	218,50	225,51	235,01
Q3A1	765	496,5	317,00	327,17	340,96
	770	499,2	316,20	333,70	338,90
	772	498,2	321,00	331,30	345,26
Q1A2	54,8	40,7	71,20	73,48	76,58
	61,1	45,3	65,40	67,50	70,34
	60,1	45	66,50	68,63	71,53
Q2A2	128,4	94,4	117,30	121,06	126,17
	132,4	97,3	120,90	124,78	130,04
	132,3	97,3	118,60	118,90	122,60
Q3A2	272,1	194,2	179,60	185,36	193,17
	272,9	195,4	172,70	178,24	185,75
	272,2	195,2	172,90	182,00	186,20
Q1A3	18,9	14,3	25,10	25,91	27,00
	18,4	14,2	23,20	23,94	24,95
	18,4	14,3	23,90	23,40	24,20
Q2A3	39,1	29,5	43,60	45,00	46,90
	38,4	28,8	42,20	43,55	45,39
	37,9	28,8	44,30	42,90	43,40
Q3A3	83,7	61,8	80,70	83,29	86,80
	80,8	59,9	73,90	76,27	79,49
	81,8	60,7	80,70	83,29	86,80

10.2 Appendix B

Conversion photon dose equivalent Hx (µSv) to air kerma Ka (µGy)

	PM_500 (Hx - µSv)	IC 32002 (Ka-µGy)	F_conv (Ka/Hx) (µGy/µSv)	PM_500 (Ka-µGy)	PM_500/IC 32002 (µGy/µGy)	PDM-Raysafe i3 (Hp(10) - µSv)
Q1A1	174,10	117,70	0,68	124,90	1,06	143,83
	173,30	117,40	0,68	124,33	1,06	148,17
	174,10	117,70	0,68	124,90	1,06	143,27
Q2A1	361,60	243,90	0,67	259,42	1,06	223,60
	374,20	251,80	0,67	268,46	1,07	226,55
	374,80	252,50	0,67	268,89	1,06	226,34
Q3A1	765,00	496,50	0,65	548,82	1,11	328,38
	770,00	499,20	0,65	552,41	1,11	329,60
	772,00	498,20	0,65	553,84	1,11	332,52
Q1A2	54,80	40,70	0,74	39,31	0,97	73,76
	61,10	45,30	0,74	43,83	0,97	67,75
	60,10	45,00	0,75	43,12	0,96	68,89
Q2A2	128,40	94,40	0,74	92,12	0,98	121,51
	132,40	97,30	0,73	94,99	0,98	125,24
	132,30	97,30	0,74	94,91	0,98	120,03
Q3A2	272,10	194,20	0,71	195,21	1,01	186,05
	272,90	195,40	0,72	195,78	1,00	178,90
	272,20	195,20	0,72	195,28	1,00	180,37
Q1A3	18,90	14,30	0,76	13,56	0,95	26,00
	18,40	14,20	0,77	13,20	0,93	24,03
	18,40	14,30	0,78	13,20	0,92	23,83
Q2A3	39,10	29,50	0,75	28,05	0,95	45,16
	38,40	28,80	0,75	27,55	0,96	43,71
	37,90	28,80	0,76	27,19	0,94	43,53
Q3A3	83,70	61,80	0,74	60,05	0,97	83,60
	80,80	59,90	0,74	57,97	0,97	76,55
	81,80	60,70	0,74	58,68	0,97	83,60

10.3 Appendix C

Descriptive statistics for angular response of RaySafe i3 in horizontal plane

PDM_GREY	-90°	-75°	-60°	-45°	-30°	-15°	0°	15°	30°	45°	60°	75°	90°
Mean (µSv)	11,30	20,60	23,02	23,66	24,46	24,48	24,68	24,22	25,42	24,30	24,08	22,06	15,40
SD (µSv)	0,56	1,48	1,43	1,33	2,25	1,73	1,78	1,94	2,33	1,19	2,58	1,57	0,82
Minimum (µSv)	10,90	18,90	21,30	22,00	22,00	22,90	23,10	22,40	22,50	22,70	21,20	19,90	14,20
Maximum (µSv)	12,20	22,30	24,80	25,60	27,30	26,80	27,00	27,10	27,60	25,80	26,50	23,50	16,10
Total (µSv)	56,50	103,00	115,10	118,30	122,30	122,40	123,40	121,10	127,10	121,50	120,40	110,30	77,00
Total %	46,16	84,15	94,04	96,65	99,92	100,00	100,82	98,94	103,84	99,26	98,37	90,11	62,91
PDM_BLUE	-90°	-75°	-60°	-45°	-30°	-15°	0°	15°	30°	45°	60°	75°	90°
Mean (µSv)	10,96	19,42	23,12	22,92	23,58	23,88	23,96	24,00	23,74	23,84	22,50	21,20	16,44
SD (µSv)	0,47	0,79	0,73	1,02	0,61	0,60	0,81	1,09	0,80	0,65	0,80	0,49	0,31
Minimum (µSv)	10,50	18,70	22,00	21,60	22,50	23,40	23,10	23,00	22,70	22,90	21,40	20,70	15,90
Maximum (µSv)	11,70	20,30	23,80	23,90	24,00	24,90	25,00	25,50	24,70	24,50	23,40	21,80	16,70
Total (µSv)	54,80	97,10	115,60	114,60	117,90	119,40	119,80	120,00	118,70	119,20	112,50	106,00	82,20
Total (%)	45,74	81,05	96,49	95,66	98,41	99,67	100,00	100,17	99,08	99,50	93,91	88,48	68,61
PDM_RED	-90°	-75°	-60°	-45°	-30°	-15°	0°	15°	30°	45°	60°	75°	90°
Mean (µSv)	11,68	20,66	23,14	24,98	24,86	24,40	25,32	25,34	25,92	24,00	24,14	22,38	15,58
SD (µSv)	0,71	0,93	1,19	1,27	1,89	0,80	1,81	1,49	1,24	1,33	0,81	0,63	0,90
Minimum (µSv)	10,80	19,50	21,60	23,30	23,10	23,50	23,50	23,30	24,40	22,80	23,20	21,70	14,30
Maximum (µSv)	12,40	21,90	24,50	26,50	26,90	25,40	27,60	26,50	27,20	25,90	24,90	23,10	16,50
Total (µSv)	58,40	103,30	115,70	124,90	124,30	122,00	126,60	126,70	129,60	120,00	120,70	111,90	77,90
Total %	46,13	81,60	91,39	98,66	98,18	96,37	100,00	100,08	102,37	94,79	95,34	88,39	61,53

10.4 Appendix D

Descriptive statistics for angular response of RaySafe i3 detectors in vertical plane

PDM_GREY	90°	75°	60°	45°	30°	15°	0°	-15°	-30°	-45°	-60°	-75°	-90°
Mean (µSv)	7,10	14,14	20,92	21,64	25,34	24,22	26,44	25,06	23,76	24,14	24,80	22,06	19,88
SD (µSv)	0,43	1,17	1,86	1,55	0,83	1,92	1,59	1,97	1,70	1,23	1,32	2,32	0,78
Minimum (µSv)	6,50	12,10	18,70	20,50	24,10	22,10	23,70	22,80	22,60	22,60	23,90	19,20	18,60
Maximum (µSv)	7,70	15,00	22,90	24,30	26,20	26,90	27,60	27,90	26,70	25,90	27,10	24,90	20,50
Total (µSv)	35,50	70,70	104,60	108,20	126,70	121,10	132,20	125,30	118,80	120,70	124,00	110,30	99,40
Total %	26,85	53,48	79,12	81,85	95,84	91,60	100,00	94,78	89,86	91,30	93,80	83,43	75,19
PDM_BLUE	90°	75°	60°	45°	30°	15°	0°	-15°	-30°	-45°	-60°	-75°	-90°
Mean (µSv)	7,00	13,06	19,68	22,26	23,44	23,44	24,42	23,76	23,68	24,22	23,28	21,28	16,82
SD (µSv)	0,12	0,17	0,58	0,95	0,87	0,78	0,90	0,88	1,04	0,54	0,26	0,73	0,47
Minimum (µSv)	6,90	12,80	18,90	21,00	22,40	22,60	23,30	22,90	22,30	23,60	22,90	20,30	16,30
Maximum (µSv)	7,20	13,20	20,50	23,10	24,30	24,60	25,20	24,90	24,80	24,80	23,60	22,00	17,40
Total (µSv)	35,00	65,30	98,40	111,30	117,20	117,20	122,10	118,80	118,40	121,10	116,40	106,40	84,10
Total %	28,67	53,48	80,59	91,15	95,99	95,99	100,00	97,30	96,97	99,18	95,33	87,14	68,88
PDM_RED	90°	75°	60°	45°	30°	15°	0°	-15°	-30°	-45°	-60°	-75°	-90°
Mean (µSv)	7,74	14,02	22,02	23,24	23,46	23,74	25,10	25,12	25,08	24,24	24,40	22,60	17,90
SD (µSv)	0,41	0,91	0,87	1,24	1,41	1,36	0,94	1,47	1,74	1,10	1,35	0,75	1,23
Minimum (µSv)	7,20	13,10	20,60	21,80	21,90	22,40	23,70	23,40	22,40	23,10	23,00	21,70	16,30
Maximum (µSv)	8,20	15,30	22,80	24,40	25,20	25,80	26,00	27,00	26,90	26,00	26,20	23,70	19,20
Total (µSv)	38,70	70,10	110,10	116,20	117,30	118,70	125,50	125,60	125,40	121,20	122,00	113,00	89,50
Total %	30,84	55,86	87,73	92,59	93,47	94,58	100,00	100,08	99,92	96,57	97,21	90,04	71,31

10.5 Appendix E

Determination of individual correction factors for TLD 100-H chips

TLD No.	"nC"	µGy/nC	TLD No.	"nC"	µGy/nC	TLD No.	"nC"	µGy/nC
C_H_A1	11,519	71,543	C_H_E1	38,399	21,461	C_H_J1	42,229	19,515
C_H_A2	22,669	36,354	C_H_E2	37,838	21,780	C_H_J2	42,366	19,452
C_H_A3	21,674	38,023	C_H_E3	33,52	24,585	C_H_J3	44,166	18,659
C_H_A4	25,476	32,348	C_H_E4	26,374	31,247	C_H_J4	37,612	21,911
C_H_A5	30,542	26,983	C_H_E5	33,272	24,769	C_H_J5	33,842	24,351
C_H_A6	23,985	34,359	C_H_E6	26,315	31,317	C_H_J6	35,639	23,124
C_H_A7	21,176	38,917	C_H_E7	38,811	21,234	C_H_J7	34,006	24,234
C_H_A8	26,771	30,783	C_H_E8	31,67	26,021	C_H_J8	38,283	21,527
C_H_A9	19,490	42,283	C_H_E9	35,464	23,238	C_H_J9	33,763	24,408
C_H_A10	24,771	33,269	C_H_E10	33,292	24,754	C_H_J10	27,786	29,659
C_H_B1	28,105	29,322	C_H_F1	34,899	23,614	C_H_K1	44,078	18,696
C_H_B2	26,466	31,138	C_H_F2	36,927	22,317	C_H_K2	34,431	23,935
C_H_B3	27,180	30,320	C_H_F3	40,063	20,570	C_H_K3	41,480	19,867
C_H_B4	28,401	29,017	C_H_F4	39,033	21,113	C_H_K4	38,747	21,269
C_H_B5	26,018	31,674	C_H_F5	31,076	26,519	C_H_K5	38,501	21,405
C_H_B6	28,380	29,038	C_H_F6	28,395	29,023	C_H_K6	31,711	25,988
C_H_B7	27,926	29,510	C_H_F7	36,106	22,824	C_H_K7	31,379	26,263
C_H_B8	27,835	29,607	C_H_F8	33,442	24,643	C_H_K8	31,470	26,187
C_H_B9	28,817	28,598	C_H_F9	29,842	27,615	C_H_K9	29,685	27,761
C_H_B10	26,836	30,709	C_H_F10	37,331	22,075	C_H_K10	30,778	26,776
C_H_C1	32,222	25,576	C_H_G1	43,357	19,007	C_H_L1	35,704	23,081
C_H_C2	22,432	36,738	C_H_G2	39,628	20,796	C_H_L2	24,049	34,268
C_H_C3	26,384	31,235	C_H_G3	49,302	16,715	C_H_L3	36,821	22,381
C_H_C4	28,681	28,733	C_H_G4	36,488	22,586	C_H_L4	37,142	22,188
C_H_C5	45,432	18,139	C_H_G5	36,267	22,723	C_H_L5	32,062	25,703
C_H_C6	52,186	15,792	C_H_G6	38,707	21,291	C_H_L6	25,491	32,329
C_H_C7	48,965	16,830	C_H_G7	38,787	21,247	lC_H_L7	20,681	39,848
C_H_C8	52,786	15,612	C_H_G8	37,531	21,958	C_H_L8	25,658	32,119
C_H_C9	51,785	15,914	C_H_G9	40,034	20,585	C_H_L9	13,563	60,761
C_H_C10	45,538	18,097	C_H_G10	39,287	20,976	C_H_L10	22,971	35,876
C_H_D1	58,390	14,114	C_H_H1	47,605	17,311	C_H_M1	32,876	25,067
C_H_D2	55,169	14,938	C_H_H2	40,061	20,571	C_H_M2	33,015	24,961
C_H_D3	53,289	15,465	C_H_H3	37,392	22,039	C_H_M3	24,278	33,944
C_H_D4	48,184	17,103	C_H_H4	43,567	18,916	C_H_M4	25,165	32,748
C_H_D5	51,579	15,977	C_H_H5	30,245	27,247	C_H_M6	18,546	44,435
C_H_D6	36,160	22,790	C_H_H6	36,303	22,701	C_H_M7	18,772	43,900
C_H_D7	26,924	30,608	C_H_H7	35,068	23,500	C_H_M8	27,161	30,341
C_H_D8	31,071	26,523	C_H_H8	37,392	22,039	C_H_M9	33,403	24,671
C_H_D9	23,654	34,840	C_H_H9	35,792	23,025	C_H_M10	11,354	72,582
C_H_D10	27,170	30,331	C_H_H10	38,053	21,657			